CRANFIELD UNIVERSITY

HAO LI

AEROELASTIC INVESTIGATION OF CONVENTIONAL FIXED
WINGS AND BIO-INSPIRED FLAPPING WINGS
BY ANALYSIS AND EXPERIMENT

School of Aerospace Transport and Manufacturing

PhD
Academic Year: 2015 - 2018

Supervisor: Prof. Shijun Guo
September 2018

CRANFIELD UNIVERSITY

School of Aerospace Transport and Manufacturing

PhD

Academic Year 2015 - 2018

HAO LI

Aeroelastic Investigation of Conventional Fixed Wings and Bio-inspired Flapping Wings by Analysis and Experiment

Supervisor: Prof. Shijun Guo
September 2018

ABSTRACT

In this thesis, the structure and aeroelastic design, analysis and optimization of conventional fixed wing is firstly addressed. Based on the study results of conventional fixed wing, the study then focuses on the more complicated aerodynamics and aeroelasticity of flapping wing Micro Air Vehicles (MAV).

A Finite Element (FE) model of a composite aircraft wing is firstly used as case study for the aeroelasticity of conventional fixed wing. A MATLAB-NASTRAN interfaced optimization platform is created to explore the optimal design of the wing. Optimizations using the developed platform show that 13% of weight reduction can be achieved when the optimization objective is set to minimize wing weight; and 18.5% of flutter speed increase can be achieved when aeroelastic tailoring of composite laminate layups is carried out. The study results further showed that the most sensitive part of the wing for aeroelastic tailoring is near the engine location, which contributes to the majority of flutter speed increment for optimization.

In order to facilitate the structural design of non-circular cross section fuselage of Blended-Wing-Body (BWB) aircraft, an analytical model of 2D non-circular cross section is developed, which provides efficient design and optimization of the fuselage structure without referring to FE models. A case study based on a typical BWB fuselage using the developed model shows that by optimizing the fuselage structure, significant weight saving (17%) can be achieved.

In comparison with the conventional fixed wing, insect flapping wings demonstrate more complicated aerodynamic and aeroelastic phenomena. A semi-empirical quasi-steady aerodynamic model is firstly developed to model the unsteady aerodynamic force of flapping wing. Based on this model, the aerodynamic efficiency of a Flapping Wing Rotor (FWR) MAV is investigated. The results show that the optimal wing kinematics of the FWR falls into a narrow range of design parameters governed by the dimensionless Strouhal number (St). Furthermore, the results show that the passive rotational of the

FWR converges to an equilibrium state of high aerodynamic efficiency, which is a desirable feature for MAV applications.

Next, the aerodynamic lift coefficient and efficiency of the FWR are calculated and compared with typical insect-like flapping wings and rotary wing. The results show that the aerodynamic efficiency of FWR in typical wing kinematics is higher than insect-like flapping wings, but slightly lower than the conventional rotary wing; the FWR aerodynamic lift coefficient (C_L) surpassed the other wings significantly.

Based on the numerical results, the study then continued to experimental investigations of the FWR. A prototype FWR model of weight 2.6g is mounted on a load cell to measure the instantaneous lift production. The kinematics of the wing is captured using high speed camera. Aeroelastic twist of the wing is measured using the resulting wing motion. Analyses by CFD and the quasi-steady aerodynamic model is then carried out and compared with experimental results. The study revealed that passive twist of the FWR wing due to aeroelastic effects forms desirable variations of wing Angle of Attack (AoA), which improves the aerodynamic performance of FWR.

The results of the thesis provide guidance for structural, aerodynamic and aeroelastic design, analysis and optimization of conventional fixed wing, as well as bio-inspired flapping wing MAVs.

Keywords:

Aeroelasticity; composite wing; design optimization; bio-inspired flapping wing; micro air vehicle; aerodynamic efficiency.

ACKNOWLEDGEMENTS

LIST OF PUBLICATIONS

The work of this thesis is based on the following publications:

A. Li, H., Guo, S., Zhang, Y.L., Zhou, C. and Wu, J.H. (2017) 'Unsteady aerodynamic and optimal kinematic analysis of a micro flapping wing rotor', *Aerospace Science and Technology*, 63, pp. 167–178.

B. Li, H. and Guo, S. (2018) 'Aerodynamic efficiency of a bio-inspired flapping wing rotor at low Reynolds number', *Royal Society Open Science*, 5(3) The Royal Society, p. 171307.

C. Guo, S., Li, H., Zhou, C., Zhang, Y.L., He, Y. and Wu, J.H. (2018) 'Analysis and experiment of a bio-inspired flyable micro flapping wing rotor', *Aerospace Science and Technology*, 79, pp. 506–517.

Publications that are related to the work of this thesis:

D. Chen, S., Li, H., Guo, S., Tong, M. and Ji, B. (2018) 'Unsteady aerodynamic model of flexible flapping wing', *Aerospace Science and Technology,* 80, pp. 354–367.

E. Wen, Q., Guo, S., Li, H. and Dong, W. (2018) 'Nonlinear dynamics of a flapping rotary wing: Modeling and optimal wing kinematic analysis', *Chinese Journal of Aeronautics*, 31(5), pp. 1041–1052.

TABLE OF CONTENTS

LIST OF FIGURES

viii

LIST OF TABLES

LIST OF ABBREVIATIONS

MAV   Micro Air Vehicle

FE   Finite Element

BWB   Blended-Wing-Body

FWR   Flapping Wing Rotor

AoA   Angle of Attack

UAV   Unmanned Aerial Vehicle

DARPA   US Defence Advanced Research Products Agency

LEV   Leading Edge Vortex

TEV   Trailing Edge Vortex

NAV   Nano Air Vehicle

ISR   Intelligence, Surveillance, and Reconnaissance

VTOL   Vertical Take-Off and Landing

AC   Alternating Current

HALE   High-Altitude-Long-Endurance

UVLM   Unsteady Vortex-Lattice Method

AR   Aspect Ratio

SHF   Simple Harmonic Function

CP   Centre of Pressure

QS   Quasi-Steady

RW   Rotary Wing

HF   Horizontal Flapping Wing

IF   Inclined Flapping Wing

CG   Centre of Gravity

GTOW   Gross Take-Off Weight

LIST OF COMMONLY USED SYMBOLS

Re	Reynolds number
η	Dimensionless wing rotation speed
ϕ	Flapping angle amplitude
f	Flapping frequency
$\dot{\phi}$	Flapping angular velocity
τ	Dimensionless time
α_u	AoA at mid-upstroke
α_d	AoA at mid-downstroke
α_e	Effective AoA
$\Delta\tau_r$	Dimensionless wing pitch time with respect to the flapping period
$\hat{r}_k$	Dimensionless radius of the kth area moment
Ro	Rossby number
C_L	Lift coefficient
C_M	Rotational moment coefficient
$\bar{C}_L$	Mean lift coefficient
$\bar{C}_M$	Mean rotational moment coefficient
St	Strouhal number
k_c	Reduced frequency
$\bar{C}_P$	Mean aerodynamic power coefficient
Pf	Dimensionless power factor
ηp	Propulsive efficiency
C_T	Thrust coefficient
I_k	kth dimensionless moment of wing area
n	Periodic ratio of flapping to rotation
Pfe	Efficiency for producing lift at the rotational equilibrium state
Pfm	Maximum efficiency for producing lift
Stp	St for maximum ηp states
Stm	St for maximum Pf states
Ste	St for equilibrium states

1 INTRODUCTION

1.1 Background

Aeroelasticity of aerial vehicles has been studied extensively since the early stage of aviation history. In the design of conventional aircraft such as fixed wing or rotorcraft, aeroelastic phenomenon is treated as a negative factor to be prevented in the flight envelope. The theory and analytical models for predicting aeroelastic stability except in transonic regime is well understood. The goal of minimizing structure weight subject to aeroelastic constraint to improve the safety margin has attracted large amount of research. Many of these techniques and analysis tools developed for the design, analysis and optimization of composite wing have now become commercialized and widely employed in the design of civil aircraft.

In the last few decades, the development of Unmanned Aerial Vehicles (UAV) and Micro Air Vehicles (MAV) has brought new challenges on aeroelasticity. It is mainly due to the increasing complexity of configuration and flexibility of wing structures that has attracted extensive study. According to the US Defence Advanced Research Products Agency's (DARPA) definition, MAVs generally refers to small aerial vehicles that are less than 10 cm in dimension, less than 10g in weight and fly at very low Reynolds number (Re, ranging from approximately 100 to 10,000 (Weis-Fogh, 1973)). Flying at such small scale poses several challenges for MAV development. First of all, the aerodynamic performance of conventional fixed wing and rotary wing drop dramatically at this low Re regime. Experimental investigations show that the lift-to-drag ratio of conventional airfoil decreases dramatically at Re below 10^5. Furthermore, the extremely light weight wing structure of MAVs results in highly flexible wings that leads to complex aeroelastic behaviours.

Inspired by the extraordinary flight capabilities of flying animals at low Re. The recent MAV research tries to mimic the flapping motion of insect wings. In contrast to the man-made fixed wing or rotors, insect wings make use of flapping motion to create relative velocity with respect to the surrounding air

flow to generate the required aerodynamic forces. The air flow structure associated with flapping wings has quite different features compared with the steady-state flow for fixed wing or rotors. Wind tunnel experiments for insect wings show that approximately 2-3 times more lift are produced for insect flapping wings compared with conventional steady-state aerodynamics (Vogel, 1967; Wakeling and Ellington, 1997), indicating unconventional aerodynamic mechanisms that increases the lift performance for insect flapping wings at low Re.

In addition to manipulating the unsteady aerodynamic forces at low Re, insect flapping wings also demonstrate complex aeroelastic behaviour. Flying insects are capable of manipulating their flexible, morphing wing structures to interact with the air flow to form desirable shapes and motions. Studies on aeroelastic behaviours of flying insects show that active control and wing flexibility has been used to enhance their aerodynamic performances (Dudley, 2002).

Although extensive previous investigations have revealed many details of the high lift mechanism and the aerodynamic basis of flapping wing flight, when applied to MAV design, major challenges still exist for the power efficiency and lift requirements associated with the low Re flight. Therefore, numerous studies have been carried out to explore the kinematic strategies of flapping wings to improve the aerodynamic performance of bio-inspired MAVs. In 2009, Guo et al. (Guo, Li and Wu, 2012) investigated a bio-inspired Flapping Wing Rotor (FWR) MAV, for which a pair of anti-symmetric wings is rotated by the aerodynamic thrust produced by vertical flapping motion, as illustrated in Figure 1-1. By varying the pitch angle of the FWR wing in an asymmetric manner, positive average aerodynamic lift can be obtained. Further numerical investigations based on CFD simulation has shown that the flow on the FWR forms compactly attached 3D vortex ring structure which connects the Leading Edge Vortex (LEV), Trailing Edge Vortex (TEV) and wingtip vortex that enhances lift production (Wu, Wang and Zhang, 2015). Based on these findings, the first flyable FWR model of weight only 2.6g was manufactured, and the first flight test was achieved in 2014 (Guo et al., 2018).
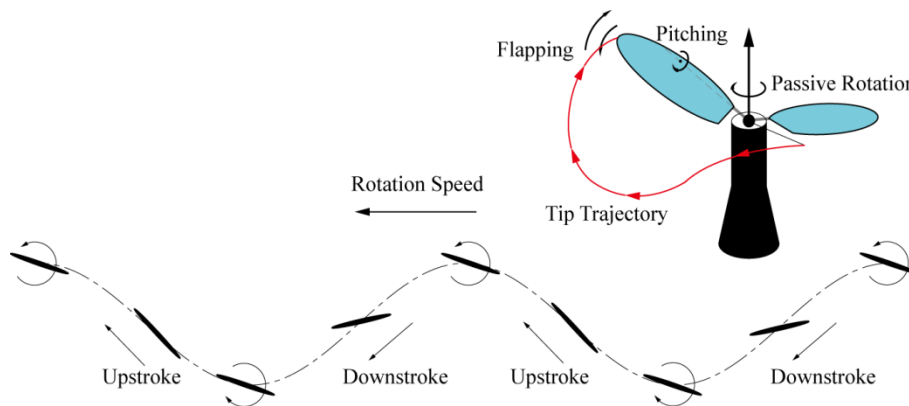
Figure 1-1 Flapping and passive rotation kinematics of FWR.

Despite these new findings, challenges still exist for MAV development in terms of aerodynamic performance and aeroelasticity. For the bio-inspired FWR, the kinematics of wing motion and its implications for aerodynamic performance has not been studied systematically. Also, among the existing MAV types, i.e. the insect-like flapping wing, the rotary wing and the FWR, there are currently very limited studies that compare the aerodynamic performances of these types, especially for the FWR configuration. In terms of aeroelasticity, there are only limited studies concerned with flapping wing. The aeroelastic effect on bio-inspired flapping wings and its implications for MAV design is still not well-understood.

Contrary to the conventional fixed wing, for which the aeroelasticity is primarily focused on preventing the aeroelastic adverse effects such as flutter and divergence, the aeroelasticity of MAVs is more focused on exploring the aeroelastic beneficial effects, i.e. improving the aerodynamic efficiency. Furthermore, the classical methods for aeroelastic study of conventional fixed wing are not applicable to MAVs, due to the complex flow phenomena associated with flapping wings at low Re. Therefore, a research gap exists for a computationally cheap method of unsteady aerodynamics to model the low Re aerodynamics of flapping wing MAVs, and also to investigate the effect of

3

aeroelasticity for the design and aerodynamic performance of flapping wing MAVs at low *Re*.

1.2 Research Aim and Objectives

The aim of this study is to advance the understanding of aerodynamics and aeroelasticity of flapping wing flight applied to MAV design at low *Re*, and further to provide guidance for engineering practices of bio-inspired MAVs. In order to achieve this aim, the objectives of this study are set as follows.

- Firstly, to demonstrate the classical methods of aeroelastic analysis and optimization for conventional fixed wing, identifying the technical connections and requirements for aeroelasticity of MAVs.
- Secondly, to develop and validate an aerodynamic model applicable for unsteady aerodynamic modelling of flapping wings at low *Re*.
- Thirdly, to investigate the aerodynamic efficiency of the FWR kinematics, focusing on both the propulsive efficiency and the efficiency of lift production of the wing.
- Fourthly, to identify the optimal wing kinematics for aerodynamic efficiency and lift production of the FWR MAV, and further to compare the aerodynamic efficiency and lift production capability of FWR with other existing types of MAVs, i.e. the insect-like flapping wing and conventional rotary wing.
- Finally, to investigate the effect of aeroelasticity of the wing on the aerodynamic performance of FWR using experimental methods based on a previously developed flyable model of FWR MAV.

1.3 Contributions

This thesis makes a systematic study on the aeroelasticity of conventional fixed wing and bio-inspired flapping wing MAVs. The main contributions of this thesis are:

- Established a method of aeroelastic optimization for conventional fixed wing based on the existing commercial software MATLAB and NASTRAN.

- Developed a semi-empirical quasi-steady aerodynamic model for modelling the unsteady aerodynamic force of flapping wings at low *Re*.
- Revealed the high efficiency characteristics of the FWR wing kinematics at rotational equilibrium state.
- Obtained the optimal kinematics of FWR for aerodynamic efficiency and lift production, which in comparison with insect-like flapping wing and conventional rotary wing, provided guidance for engineering design of MAVs under specific design requirements.
- Revealed that under proper design of wing elasticity, the aeroelastic twisting of the wing can form desirable variations of wing Angle of Attack (AoA), which helps improving aerodynamic performance of FWR.

1.4 Thesis Structure

This thesis is structured as follows:

Chapter 2 presents the literature review of MAV development, the kinematics and aerodynamic mechanism of flapping wing flight in nature, and the status of aeroelastic study for both large aircraft and small flying animals in nature.

Chapter 3 addresses the classical structural and aeroelastic design and optimization of conventional fixed wings. A few case studies of structural and aeroelastic optimization have been presented using either commercial software or developed analytical methods, which develops preliminary understanding towards aeroelasticity for further investigations of more complex MAVs.

In chapter 4, a semi-empirical quasi-steady aerodynamic model for flapping wing at low *Re* is developed. The model is validated against various cases of CFD results.

In chapter 5, the aerodynamic efficiency of the FWR kinematics is investigated, with focus on both the propulsive efficiency and efficiency of lift production of the wing.

In chapter 6, the aerodynamic efficiency and lift coefficient of FWR under various wing kinematics are calculated based on the quasi-steady aerodynamic

model. The optimal wing kinematics of FWR at a specific *Re* are then obtained, which is further compared with insect-like flapping wings and conventional rotary wings. The benefits and drawbacks of different configurations for MAV design are then discussed.

Chapter 7 presents the experiments and numerical simulations of a flyable FWR model. The instantaneous kinematics of the aeroelastic wing is captured using high speed camera image processing. The effect of aeroelasticity of the wing on the aerodynamic performance of FWR is investigated based on experimental results and numerical analyses.

Finally, chapter 8 presents a summary of the dissertation work, an outline of future research directions, and some concluding remarks.

2 LITERATURE REVIEW

2.1 Micro Air Vehicles

Micro air vehicle or MAV generally refers to the unmanned flying systems of small dimension with wide variety of applications. The early definition of the MAV dates back to 1997, when DARPA started the program called "MAV-project" where they presented some minimal requirements for MAVs. In particular, the maximum physical dimension of a MAV was set to be 15 cm, and the weight, including payload, should be less than 100 g (Mcmichael and Francis, 1997). Furthermore, flight duration should be 20 to 60 minutes. In addition to the MAV-project, DARPA started another program called Nano Air Vehicles (NAV), which focus on the aim "to develop and demonstrate an extremely small (less than 10 cm), ultralight weight (less than 10 g) air vehicle system with the potential to perform indoor and outdoor military missions" (Hylton et al., 2012). As indicated above, although DARPA has initiated the MAV and NAV project separately, in many later research, the term MAV is used more frequently to refer to the general small unmanned flying systems of either micro or nano scale (Bouabdallah, Becker and Siegwart, 2007; Kroo et al., 2000; Kroo and Kunz, 2000; Wood et al., 2007). In the present context, MAV will be used to address any of the miniature flying systems, e.g. flapping wing rotor, insect-like flapping wing and rotary wing, although the size and weight of the designs might fall into the category of NAV according to DARPA's taxonomy.

Due to the small physical dimension and low flight speed, MAVs typically operate at a range of Reynolds number between 10^2 and 10^4, which are much lower than those characteristic for conventional aircraft. The comparison of vehicle gross weight and Reynolds number of MAVs and other flight vehicles are illustrated in Figure 2-1. As can be seen from the figure, the Reynolds number for MAVs has more similarities with that for insects and small birds rather than other conventional aircraft.
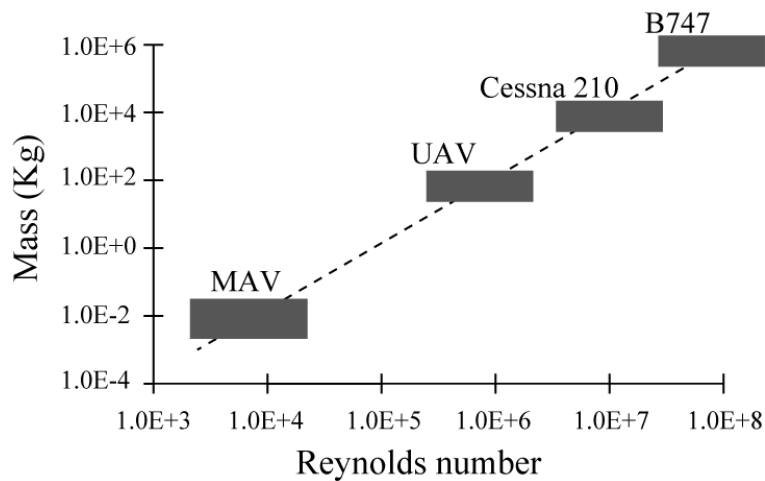
Figure 2-1 The flight regime of MAV compared to other flight vehicles, adapted from (Mueller, 1999).

2.1.1 MAV applications

The unique characteristics of MAVs such as small size and agility manoeuvre make them suitable for a wide range of applications that are often difficult for other systems. MAVs are capable of performing both indoor and outdoor missions in very challenging environments. As a result, one of the main applications for MAVs is to carry out Intelligence, Surveillance, and Reconnaissance (ISR) missions.

MAVs have tremendous advantages in performing ISR missions. They can be remotely operated by individual soldiers in the battle field for local reconnaissance. Thanks to their stealth capabilities in complex environments, they can provide rapid overview in areas around the personnel and reconnaissance inside buildings, without exposing them to danger, thus providing a very useful tactical advantage. With infrared cameras on board, they can give detailed images even in the darkness. As reported in (Bachmann et al., 2009), such small vehicles are currently the only way to remotely "look" inside buildings in the battlefield.

MAVs can also be applied for anti-terrorism missions. By carrying specific sensors such as gas, radiation or other sensors, they can be used to locate

8

biological, nuclear, chemical, or other threats. For instance, they can fly inside toxic clouds and transmit data or bring samples back to the base station, thus providing information on the composition and extent of gaseous clouds and improve the assessment of danger. Furthermore, in some situations, MAVs can be equipped with sensors and miniaturised warheads, thus capable of attacking high-value enemy targets such as radars. The global positioning system allows precise autonomous navigation and position reporting for micro aerial vehicles, which are critical for this type of missions (Pardesi, 2005).

Alongside the above military applications, MAVs also find their applications in the civilian field. For example, the police and the fire brigade could use the indoor flight capability of MAVs for inspecting unsafe or collapsed buildings for search and rescue missions (Paulsen and Muren, 2009). This is particularly useful in the situation of disasters, such as earthquakes, after hurricanes, or in collapsed mines, where fast locating survivors using MAVs increases the probability of saving lives (Bachmann et al., 2009; Petricca, Ohlckers and Grinde, 2011).

Another civilian application of MAVs is structural health monitoring. Large structures such as bridges have to be continually inspected for cracks and fatigue. These inspections can be complicated by areas that are difficult to access by human inspector. MAVs with the ability to hover can perch on the structure, which could provide access difficult areas, so that remote inspections could be performed. Furthermore, health monitoring of large distances of pipeline can also be performed with MAVs equipped with sensors to detect leaks.

There are still various applications of MAVs that have not been listed. Most of the applications are based on the ability of MAVs to operate in confined and complex environments and inside buildings, such as such as traffic control, crowd management or ordinary city surveillances.

2.1.2 MAV challenges

2.1.2.1 Aerodynamics of low Reynolds number flight

The miniaturized sizes of MAVs and their low flight speed pose several challenges on MAV development. One of the main challenges is related to the flow physics associated with the low Reynolds number flight. The Reynolds number Re measures the ratio of inertial to viscous forces in a fluid. For classical steady-state aerodynamics, Re is defined as the product of the characteristic airfoil chord length and velocity divided by the dynamic viscosity μ of the fluid:

$$Re = \frac{\rho V c}{\mu} \tag{2-1}$$

The Reynolds number is known to govern the flow characteristics over the immersed body in the fluid. At low Re, the aerodynamic performance of classical airfoil drop dramatically. Experimental investigations by McMasters and Henderson (McMasters and Henderson, 1979) showed that the airfoil lift-to-drag ratio, which is a measure of aerodynamic efficiency, decreases dramatically for smooth airfoils at $Re<10^5$. In this Re regime, rough airfoils appear to achieve higher lift-to-drag ratio than smooth airfoils. However, at $Re>10^5$, the performance of smooth airfoils greatly improves, as shown in Figure 2-2. This dramatic decrease in lift-to-drag ratio for smooth airfoil at low Re is primarily due to flow separation for the viscous laminar flow in this Re regime (O'Meara and Mueller, 1987; Pelletier and Mueller, 2000; Pines and Bohorquez, 2006). Flow visualization experiments by Bohorquez et al. at $Re=3\times10^4$ for a rotor airfoil revealed that large-scale flow separation exists, with only a fraction of the airfoil having attached flow (Bohorquez et al., 2003). This is largely because in this low Re regime, the relatively low inertia forces in the fluid boundary layer render it unstable, and tends to separate in the face of the adverse pressure gradients after the suction peak on the airfoil (Lin and Pauley, 1996; Pauley, Moin and Reynolds, 1990; Tatineni and Zhong, 2000).

The effect of Re for MAV performances can be further understood by looking at the biological propellers in nature. Observations show that the selection of the

propelling mode for organisms is highly dependent on the *Re*. In the very low *Re* realm (*Re* less than about 15), viscous forces dominate, organisms use the drag-based-propulsion to move through the fluid (Blake, 1978; McHenry, 2003), examples are the oar-like (Williams, 1994), ciliary (Blake and Sleigh, 1974) and flagellar (Lighthill, 1976) propulsion. In the high *Re* regime, inertia effects dominate, and the lift-based steady-state aerodynamics applies, examples are the soaring and gliding of birds' flight (Musiak and Vogel, 1996). The most challenging realm is at the intermediate *Re* (*Re* is of order 10^3), typically employed by flying insects and small birds, where flapping wings are used to generate large vortices and produce high lift (Walker, 2002). This is precisely the realm where the MAVs resides, as indicated in Figure 2-1.
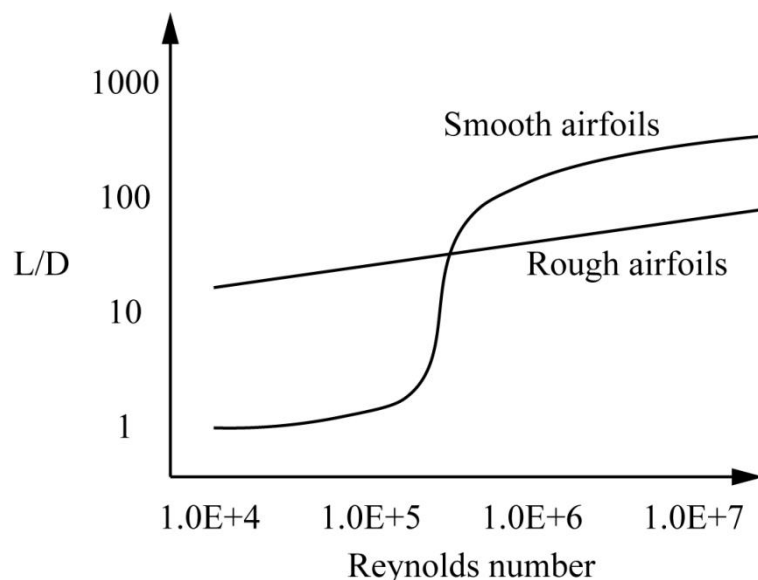
Figure 2-2 Lift-to-drag ratio versus Reynolds number for smooth and rough airfoils, adapted from (McMasters and Henderson, 1979).

Since steady-state aerodynamics has low efficiency at the low *Re* regime of MAVs, endeavours have been made to reveal the unsteady aerodynamic mechanisms employed by insects' flight. Pioneering research by Lighthill (Lighthill, 1997), Rayner (Rayner, 1988, 1979) and Pennycuick (Pennycuick, 1989, 1996) has provided some insight into avian flight. Over the past few

11

decades, biologists and aerodynamicist have made significant advances in understanding the aerodynamic physics of insects' flight. The first unsteady aerodynamic mechanism of insect flight was the 'clap-and-fling' proposed by Weis-Fogh in studying flight characteristics of small wasp (*Encarsia Formosa*) (Weis-Fogh, 1973). In the 'clap-and-fling' hypothesis, the wings of insects first come close dorsally to form a 'clap', and then 'fling' apart to generate bound vortex which increases the lift (Spedding and Maxworthy, 1986). More generally, Ellington (Ellington et al., 1996) proposed that the stability of LEV is responsible for the majority of high lift generated by insect flapping wings, and that the axial flow on the LEV core serves to transport vorticity toward wingtip, thus stabilizes LEV. Later, Dickinson et al. (Dickinson, Lehmann and Sane, 1999; Sane and Dickinson, 2001) proposed several unsteady aerodynamic mechanism associated with insect flapping wings, including rotational circulation and added mass effects which explain how insect wings generate such large aerodynamic forces over a complete wing-beat cycle.

The limited aerodynamic efficiency at the low *Re* regime of MAVs poses significant challenge for MAV design. However, recent investigations on biological flyers have revealed many novel aerodynamic mechanisms employed by nature. Research in this direction has brought bio-inspired design of MAVs which mimic the wing motion of flying insects.

2.1.2.2 Structural miniaturization

In addition to the complex flow physics associated with the low *Re* flight, MAV design is also challenged by the design of light weight and flexible structures of the micro mechanical system. The questions arise when scaling down the size of an air vehicle to MAV scale: How should the structural components, as well as the material and mass properties scale, in order to achieve a certain endurance and payload requirements of MAVs? How to design the light weight and flexible structures of MAVs to improve the mechanical as well as aerodynamic efficiency? In the past decade, researchers and engineers have made significant efforts to address these questions (Ifju, 2005; Pines, Bohorquez and Sirohi, 2005; Shyy, Ifju and Viieru, 2005).

Since geometric similarity provides a means for comparing the structural efficiency, it is desirable to compare MAV structural design parameters with those found in nature. Pines and Bohorquez (Pines and Bohorquez, 2006) compared the geometric scaling relationships for small birds with fixed-wing MAV designs. They found that most MAV designs have shorter wing spans and lower aspect ratios than their biological counterparts. As a result, they proposed that MAVs requires more carefully designed control system and higher bandwidth control for the same Gross Take-Off Weight (GTOW) in comparison with birds. Further, the low aspect ratio of MAVs also implies reduced aerodynamic efficiency of gliding or soaring compared with natural flyers.

Another observation from natural flyers is that their wings are highly flexible, in contrast to conventional air vehicles which uses rigid wing structure, with ribs and stiffeners to suppress deformation. This is most likely due to the extremely light weight bio-structure of biological flyers. In full-scale aircraft, rigid wings with high stiffness are desirable to support the air loads and to minimize structural dynamic effects such as unstable aeroelastic interactions. However, in the MAV scale, natural flyers seem to make use of wing flexibility to manipulate unsteady aerodynamic forces. An example of the potential advantages of flexible wings is passive adaptive washout control that extends the range of the aerodynamic lifting surface. Such wings have the effect of suppressing wind gusts and restoring constant thrust and lift over the airfoil (Pines and Bohorquez, 2006). In previous studies (Ifju, 2005; Shyy, Ifju and Viieru, 2005), numerous flexible fixed-wing designs and manufacturing methods have been developed to understand the performance enhancements of flexible wings for fixed-wing MAVs.

Although the effect of structural flexibility for biological flyers is still an ongoing topic of study, from the MAV design point of view, structural flexibility is unavoidable due to the extreme light weight of the structures. The design of the light weight and flexible wing structure for desirable mechanical and aerodynamic performance is most challenging. Depending on the detailed wing

kinematics of motion, the optimal distribution of wing flexibility can vary significantly.

2.1.2.3 Energy storage, propulsion and actuation systems

The limited aerodynamic efficiency in the low *Re* flight makes the power system design extremely challenging for MAVs. For example, Pines and Bohorquez (Pines and Bohorquez, 2006) gave a detailed breakdown of the mass fractions of some existing MAVs in comparison with a full-scale Boeing 767 commercial jetliner. Their results show that for the small-scale flyers the mass fraction of the propulsion system (including batteries, power and motor) is in excess of 60% of the total vehicle mass, in contrast to the jetliner with propulsion and fuel system weight of less than 40%. Furthermore, the payload mass fraction of small-scale flyers are just around 9% for the examples MICOR (micro coaxial rotorcraft of University of Maryland) (Bohorquez et al., 2003) and Microbat (CalTech Aerovironment) (Kornbluh, 2002; Pornsin-Sirirak et al., 2000), whereas the Boeing 767 has a payload mass fraction of 29%. The relatively high mass fraction of power and propulsion system and relatively low mass fraction of payload for MAV systems reflects the difficulties of scaling down energy storage and motor systems while maintaining acceptable performance for MAVs.

In contrast to the man-made MAVs, the actuation systems of biological flyers seems to be very effective. Insects and birds use muscles to convert chemical energy to mechanical energy to perform large-scale flapping kinematics. According to Rayner (Rayner, 1988, 1979), approximately 16% of the bird's body mass is comprised of the pectoral and supracoracoideus muscles. The pectoral muscle is used in the downstroke of a bird's flapping cycle and is significantly larger compared with the supracoracoideus muscle that is used for the upstroke motion of the wing. Compared with humans, birds have approximately three times the mass fraction of muscles, indicating that the low *Re* flight is still a power intensive endeavor even for the highly evolved biological flyers.

For MAV design, various investigations have been made into the power and propulsion system in the miniature scale. The relevant research in this direction

include the micro gas turbine engines of Massachusetts Institute of Technology (MIT) (Cadou et al., 2003; Epstein and Senturia, 1997), flexible/conformal sheets of lithium ion battery technology, high energy density micro fuel-cell technology (Fu et al., 2001), among others the micro internal combustion engines (Chigier and Gemci, 2003). Despite the developments in the micro energy and propulsion system for MAVs, the endurance capability of current MAVs is still quite limited and rarely satisfactory. A review of some existing MAV designs show that the maximum endurance time of the existing MAVs can rarely achieve the true long-loiter or hovering time requirement (longer than 60 min) (Pines and Bohorquez, 2006).

2.1.3 MAV categories

The majority of the existing MAVs can be divided into three categories. These are the fixed wing, the rotary wing and the bio-inspired flapping wing. Fixed wing MAVs are simply small airplanes that use fixed lifting surfaces to provide lift for flight, and use control surfaces to provide directional control; rotary wing MAVs are essentially small helicopters; bio-inspired flapping wing MAVs are micro robotic systems that mimic the flapping kinematics of wing motion of insects or birds to generate lift and thrust, as well as providing flight control.

Among the different typologies of MAVs, fixed wing is the most developed and the easiest to design and build, since some well established design methods for larger operational fixed wing UAVs can be applied with some precautions and modifications for low *Re* aerodynamics (Al-Qadi and Al-Bahi, 2006). The shortcoming of fixed wing MAVs is that they are incapable of hovering or flying slowly, since the lifting surfaces require certain flight speed to produce enough lift. Therefore, fixed wing MAVs are typically used for comparatively long endurance outdoor missions. Examples of suitable applications are location of forest fires, searching for people at sea, and missions where low speed flight is not required.

Similar to helicopters, rotary wing MAVs are capable of hovering, Vertical Take-off and Landing (VTOL). These features make them perfect for operations in confined spaces such as indoor flight and local reconnaissance. When

miniaturized, rotary wing at low *Re* also subject to low aerodynamic efficiency (Schafroth et al., 2009). Therefore, endurance is also the bottleneck for this kind of MAVs. For classical helicopter configuration, an additional tail rotor is required to counteract the reaction torque, which increases system complexity and costs extra power. Alternate rotary wing configurations include coaxial rotor, tandem and quad rotor (Datta et al., 2000).

Due to the inherent limitation of low *Re* aerodynamics for fixed wing and rotary wing, researchers have been devoted to find alternative strategies for MAV design. Bio-inspired flapping wing was proposed for the design of aerial vehicles since the early stage aviation. However, it was until the recent development need for MAVs that brought much focus on designing flyers with insect-like or bird-like wing motions. This is largely motivated by the extraordinary flight and aerodynamic capabilities of insects and birds in the low *Re* regime.

There are typically two classes of bio-inspired flapping wing for MAV design. The first class mimic the wing motion of birds and are usually called 'Ornithopters', while the second class mimic the wing motion of flying insects and are usually called 'Entomopters' (Petricca, Ohlckers and Grinde, 2011). Ornithopters, like the majority of birds, generate lift and thrust force by flapping their wings up and down with synchronized small variations of AoA. This method of lift and thrust generation requires forward flight similar to a fixed wing (Galiński and Żbikowski, 2007). As a result, ornithopters cannot hover, and they need to obtain an initial airspeed before taking off. On the other hand, entomopters use the kinematics of insects for flying. In a flapping cycle, the wings of entomopters undergo large amplitude flapping and significant variations in AoA. Like the flying insects, entomopters are capable of hovering and VTOL. Therefore, they are of greater interest to MAV developers.

Compared with the fixed wing and rotary wing, bio-inspired flapping wing offers greater manoeuvrability. The entomopters make use of insect-like flapping wing kinematics to manipulate the unsteady aerodynamic mechanism at low *Re*, which is capable of generating higher aerodynamic force compared with fixed

wing and rotary wing of the same size (wing area), and therefore, has greater potential for miniaturization. In fact, a review of data on MAV research shows that nearly half of the research articles on MAVs are focused on bio-inspired flapping wings (Ward et al., 2017).

2.1.4 Research and development of MAVs

Since the initiation of the concept of MAV by DARPA in 1997, great interests and research efforts have been made into the field. The early development of MAVs was marked by a few designs by aerospace engineers and researchers based on fixed wing and rotary wing configurations, including the Black Widow developed by Aerovironment Inc., the MicroStar developed by Lockheed-Martin Inc., the MICOR (Micro Coaxial Rotorcraft) by University of Maryland, and the flexible wing MAV developed by University of Florida (Bohorquez et al., 2003; Ettinger et al., 2003; Ifju, 2005; Morris, 1997). Some of the design and performance parameters of these MAVs are presented in Table 2-1.

Table 2-1 Design and performance parameters of some representative MAVs.

Vehicle parameters	Black Widow (Aerovironment)	MicroStar (Lockheed-Martin)	MICOR (University of Maryland)	Flexible wing MAV (University of Florida)
Configuration	Fixed-wing	Fixed-wing	Rotary-wing	Fixed-wing
GTOW, g	80	110	103	65
Cruise speed, m/s	13.4	13.4-15.6	2	6.7-15.6
Wing span or rotor diameter, cm	15.24	22.86	15.24	15.24
Endurance, min	30	25	3	15
Power source	Lithium-ion batteries	Lithium-ion batteries	Lithium-ion batteries	Lithium-polymer batteries

These early developed prototypes demonstrate the challenges for MAV development. In particular, fixed wing MAVs are incapable of hovering and vertical take-off and landing. Both fixed wing and rotary wing show very limited

endurance, primarily due to the low aerodynamic efficiency of flight at the low *Re*. Inspired by the extraordinary flight capability of natural flyers, flapping wing MAVs were proposed as alternative design for MAVs, which soon attracted most research interests in the field. Caltech and Aerovironment developed the Microbat MAV which uses flapping wings via an electric motor to generate thrust and lift (Pornsin-Sirirak et al., 2000). Delft University of Technology developed the 'DelFly' which make use of insect-like flapping wing kinematics to generate lift and thrust. The DelFly is capable of hovering and VTOL, weighs only 3 g, has a wing span of 10 cm, and is capable of carrying a camera payload (G.C.H.E. et al., 2009, 2012; Kristien M.E. et al., 2009). Wood et al. at Harvard University (Ma et al., 2013; Pérez-Arancibia et al., 2011; Wood, 2008) developed an at scale micro robotic fly that mimic the wing motion of *Diptera* (flies). The robotic fly is the smallest bio-inspired MAV developed so far with only 60 mg weight, and achieved tethered flight through an external power supply. In 2011, Aerovironment (under DARPA funding) announced a hummingbird-like MAV prototype that is capable of flying at 11 miles per hour and perching on a windowsill (Keennon, Klingebiel and Won, 2012). The nano hummingbird has total mass of 19 g, wing span 16.5 cm and endurance 4 min.

The development of bio-inspired flapping wing MAVs is accompanied by the advancements in a number of fundamental areas involving aerodynamics, biology, sensors, actuators, materials and power technology. In the past two decades, most of the research on bio-inspired flapping wing has been focused on the unsteady aerodynamics of the low *Re* flapping wing flight. Many pioneering research done by biologist and aerodynamicist has revealed much of the aerodynamic mechanisms associated with the low *Re* flight of biological flyers. This part of research will be reviewed in the following sections.

2.1.4.1 Bio-inspired robotic actuation systems

One major challenge when designing a practical flapping wing MAV is the efficient actuation system that can generate the large amplitude complex angular motion like the insect wings. Study from insects' anatomy show that two different sets of muscles are primarily responsible for generating the complex

wing motions of insect wings. These muscles either act directly on the wing base and sclerites of the auxiliary apparatus or act indirectly to move the wings via thoracic deformation (Dudley, 2002). Furthermore, the wings and thorax of insects during flight are oscillating systems with high elasticity. At the end of each stroke, the kinetic energy is stored as elastic potential energy in the walls of the thorax, which is released during the subsequent stroke (Ellington, 1984a). Both thorax and wings of insects are resonant structures, storing energy elastically, and tuned to deform appropriately at their operating frequencies (Wootton, 2010). These intricate biomechanical system of insects have inspired many research in the robotics community to replicate the resonant vibrating structures for generating efficient and complex kinematics.

One technology that has been widely researched in application of flapping actuation mechanisms is piezoelectric materials. Piezoelectric materials are materials that produce an electric current when they are placed under mechanical stress. This process is reversible, i.e. by applying an electric current to these materials, they will change shape slightly. This property of piezoelectric materials makes them ideal for application in micro/nano mechanical actuators for extremely small flapping mechanisms. Early applications of piezoelectric actuators for micro flapping wing has been focused on designing the mechanism that amplify the limited travel distance provided by these actuators. Fearing et al. (Fearing et al., 2000) and Avadhanula et al. (Avadhanula et al., 2002) developed a piezoelectric wing driven mechanism with weight only 350 mg to mimic the wing motion of a fruitfly (*Drosophila*). Similarly, Sitti (Sitti, 2003) proposed a simple piezoelectrically actuated four-bar mechanism for micro flapping mechanism design. It was shown that beneficial mechanical efficiency and large amplitude flapping motion can be realized at the resonant frequency of the mechanism. Guo et al. (Guo, Li and Huang, 2009; Guo, Li and Wu, 2012) manufactured and tested a piezoelectric actuated flapping wing rotor model for MAV design. By experimental and numerical investigations, their piezoelectric driven flapping wing rotor was able to achieve self-propelled rotation and generate positive lift. In the robotic fly developed by Wood et al. at Harvard

University (Ma et al., 2013; Pérez-Arancibia et al., 2011; Wood, 2008), a set of piezoelectric actuators were used to drive the flapping motion of the wings.

Although piezoelectric actuators provide very efficient designs that mimic the vibrating biomechanical structure of insects' flapping mechanisms, there is a major limitation to their applications in MAVs: these actuators normally operate in Alternating Current (AC) at very high voltage (typically on the order of ±1000 V), therefore, a high voltage amplification is needed to drive the actuators, which increases system weight and complexity. Currently piezoelectric actuated MAVs can only carry out tethered flight through external power supply.

2.1.4.2 Morphological shape changing wing structures

Observations from natural flyers such as insects or birds show that their wing morphology changes dramatically during flight. Due to the light weight and flexible structure, flapping insect wings undergo large bending and twisting deformations in a flapping cycle. These deformations cause a degree of variation in the wing camber and chord length, providing aerodynamic beneficial effects for flapping wing flight (Dudley, 2002). Similarly, birds (Norberg, 2012) such as falcons use a high-aspect-ratio configuration to circle above until they detect their prey. Upon detection, their wings morphs into a strike configuration to swoop down on unsuspecting prey. This ability to change the wing geometric shapes to improve flight capacity expands the flight envelope of nature's great flyers.

Inspired by these features of natural flyers, morphing wing structure for aerial vehicles has been widely researched since the early 1890s (Barbarino et al., 2011). The morphing wing capability provides several advantages for MAV applications. First of all, the low *Re* flight regime of MAVs poses strict requirements on the aerodynamic efficiency. Second, the small dimensions and light weight of MAVs make it difficult to implement traditional control surfaces on the wings. On the other hand, the relatively simple and flexible structures of the wings are more suitable for morphing wing mechanisms implementation. Currently, the researches on morphing wing structures have been primarily

focused on large aircraft or UAVs. For MAV applications, there are relatively less studies on this topic.

Shkarayev et al. (Shkarayev, Null and Wagner, 2004) built a MAV with variable camber using micro-servos. The wing of the MAV is made of carbon-fibre epoxy laminate. A servomotor was connected to the inflection point of the airfoil through a pushing rod, which under actuation can achieve camber variation from 3% to 9%. Stanford et al. (Stanford et al., 2007) investigated a morphing wing MAV (in the form of asymmetric twisting) through torque-actuated wing structure. Numerical study using a static aeroelastic model and optimization of the design show significant improvements of performance metrics in terms of manoeuvrability and lift-to-drag ratio compared with the baseline design.

In summary, the development of MAVs has seen significant progress in the past two decade. Bio-inspired flapping wings are among others (fixed wing and rotary wing), the most researched type of MAV design, which offers significant potential in terms of low *Re* aerodynamics and structural miniaturization, as demonstrated by many successful prototypes in the field. However, despite these advancements in both the underlying physics of low *Re* flight of biological flyers and the practical implementations of engineering design, MAV design is still challenged by the limitations in endurance, power efficiency and payload carrying capabilities. Design strategies to further explore the unsteady aerodynamic mechanisms and wing kinematics of biological flyers at low *Re* can provide potential for further improvements in the performances of MAVs. Therefore, in the following chapters, the fundamentals of biological flight, including wing kinematics, aerodynamics and aeroelasticity are reviewed.

2.2 Kinematics of animal flight

Flying animals prevail in the world. The sizes of flying animals range from the miniature scale insects to large flying vertebrates such as birds and bats. The earliest flying animals on earth are the insects, which emerged about 350 million years ago (Ellington, 1991, 1999; Wootton, 1981). Over natural evolution, flying animals have evolved fascinating flight capabilities: hovering, escaping, landing, gliding, rapid turning, etc. These intriguing features have

fascinated human inspirations for many years, dating back to the early studies of Leonardo da Vinci's 'Codex on the Flight of Birds' on the flight behaviours of birds (Arasse and da Vinci, 1998) to the many more recent studies on the flight of insects (Ellington, 1984b, 1984c, 1984d, 1984e; Weis-Fogh, 1973).

Flying animals are complex biomechanical systems. Most flying insect wings are formed by the outgrowths of exoskeleton membrane, strengthened by number of longitudinal veins, and with no muscles directly attached. Therefore, during flight, the wings of insects mostly deform passively under the aerodynamic and inertia forces. This is different from birds and bats, for which the wings are formed by many bones, joints and muscles, covered by feathers that composed large area of the wing. As a result, the wings of birds and bats can operate active locomotion to change their wing shape using local muscles on the wing.

Most flying animals interact with the air using the flapping locomotion of their wings. The kinematics of their wings differs by species, the body weight and even by different flight conditions, e.g. cruising or hovering. Usually the wing motion of a flying animal combines two-strokes (Ellington, 1984d; Shyy, Berg and Ljungqvist, 1999), as shown in Figure 2-3. In hovering flight, the typical wing motions employed by insects demonstrate symmetric up and downstrokes, and the wingtip traces has the shape that resembles the figure-of-eight. On the other hand, most cruising animals such as birds have inclined flapping motion, which is characterized by asymmetric up and downstrokes, as shown in Figure 2-3 (b) and (c). Typically, for birds and bats' flight, the wing stretches and twists up in the downstroke, producing large lift and thrust; while in the upstroke, the wing is partly flexed, the outer part of the wing is folded, reducing the moment of inertia and mitigate negative lift (Shyy, Berg and Ljungqvist, 1999). During a flapping cycle, the wing must also twist continuously to adapt the AoA desired for lift production.

(a) Hovering
Figure of eight wingtip path

(b) Slow forward flight
Inclined figure of eight wingtip path

Lift

(c) Fast forward flight
Inclined elliptical wingtip path

Lift
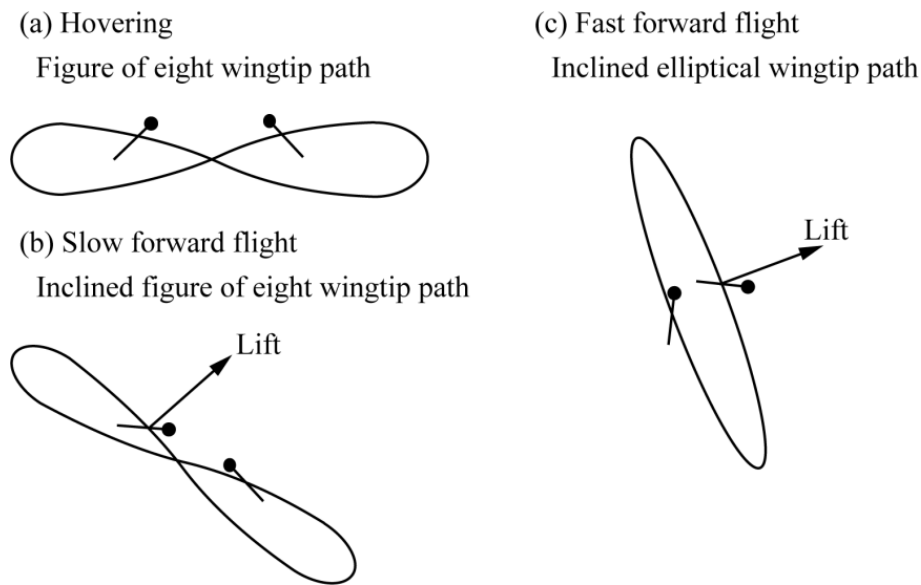
Figure 2-3 Kinematics of aerial animal flight, adapted from (Biewener, 2003).

For flapping wing flyers, the aerodynamic forces generation is susceptible to the detailed kinematic variations of the wing (translation and pitching rotation). Compared with birds and bats, insects manipulate their wing kinematics more delicately: stroke amplitude, angle of attack, timing and duration of wing rotation, and stroke-plane deviation. Insects manipulate these detailed wing kinematics in association with the unsteady aerodynamic effects at low *Re* to change the aerodynamic force production for flight control and manoeuvre. The kinematics of insect flapping wing is firstly reviewed in this section.

2.2.1 Flapping cycle and wingtip paths

The flapping cycle for most flying insects are composed of a downstroke and an upstroke. At each stroke, the wing translates at a relatively constant angle of attack from its most aft (or forward) position to its most forward (or aft) position. The wing accelerates from the beginning of each stroke to a constant or peak angular velocity around mid-stroke, after which the wing begins to decelerate and reverses its direction at the beginning of the subsequent stroke. At the stroke reversal, the wing rotates about a longitudinal axis and changes the angle of attack. The rotations of the wings at the end of upstroke and

downstroke are termed as pronation and supination, respectively. Figure 2-4 shows the typical flapping cycle of insect flapping wing.
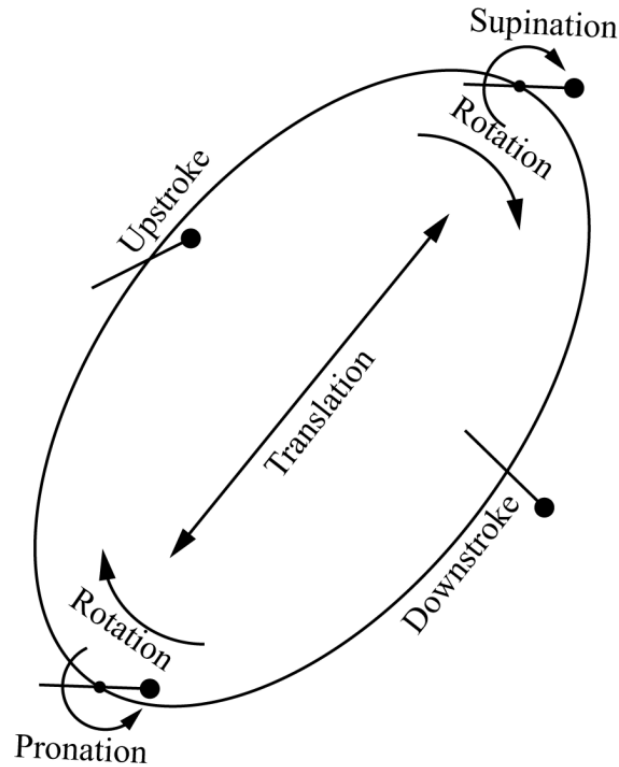
Figure 2-4 Typical flapping cycle of insect flapping wing.

For insect flight, the translation of the wing covers large portion of the flapping period. Supination and pronation are, however, largely confined to the acceleration and deceleration at the end of each half-stroke, and are approximately equal in duration, each of which lasts 10%~20% of the whole flapping period (Ellington, 1984d).

The translation of the flapping wing in the upstroke and downstroke is mainly confined in a stroke plane. However, small deviation from the stroke plane may occur. The wing tip paths of insect flapping wing can take on many shapes, including ellipses, arcs, banana-type shapes and figure-of-eight (Ellington, 1984d). The latter one is most commonly considered for the recent investigations on insect flight and engineering design (Galinski and Zbikowski, 2005; Sane and Dickinson, 2001). Although the tip paths of insect flight vary,

the majority of the aerodynamic force is produced at the mid-stroke, where the translational velocity of the wing reaches its maximum. Therefore, the deviation of the wing from the stroke plane can be neglected in most studies.

2.2.2 Horizontal and inclined flapping motion

There are typically two kinds of kinematic patterns of flapping wing: the first kinematic pattern is typical for most insects in hovering flight (fruit fly, hawkmoth, bumble bee, etc.), where the flapping wing motion is primarily adapted at a horizontal stroke plane in the figure-of-eight kinematics for lift generation. For this flight model, the pitching of the wing is nearly symmetric, and the wings have equal AoAs at upstroke and downstroke. On the other hand, some insects such as dragonfly uses inclined or vertical flapping stroke plane to generate lift. The pitching of the wing at upstroke and downstroke is asymmetric, which leads to a different AoA at each flapping stroke. The two typical kinematic patterns are shown in Figure 2-5 below.
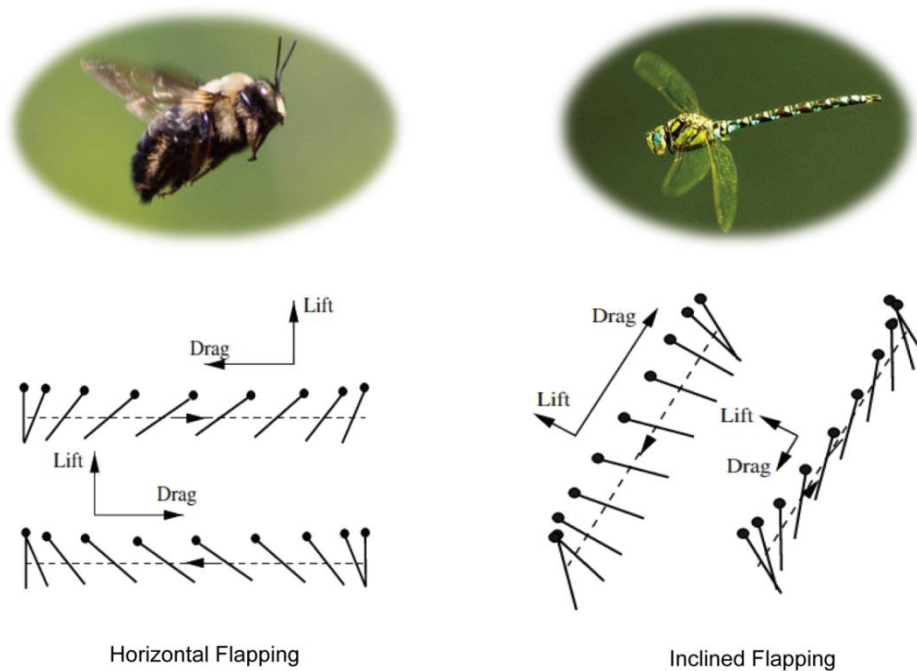
Figure 2-5 Typical kinematic patterns of insect flapping flight.

The asymmetric pitching of the dragonfly wings results in a net drag over a flapping cycle. However, since the flapping stroke plane is inclined, the net drag

results in a contribution to the upward vertical lift (Wang, 2004). This distinct kinematic pattern differs from most of the other insects of the symmetric pitching and horizontal stroke plane, where the drag force is attributed to be the penalty for lift production. By properly manipulate the drag force of the inclined flapping kinematics the aerodynamic efficiency may be substantially improved.

2.3 Flapping Wing Aerodynamics

Associated with the complex cyclic kinematic motion, the aerodynamic force of the wing is highly unsteady. The flow phenomena for a flapping wing are often governed by the continuous formation and shedding of vortices, making the forces generation difficult to be predicted from classical aerodynamic theory. A well-known historical note is that insects cannot fly according to classical aerodynamic theory (Magnan, 1934). Over the last three decades, researchers have been focused on revealing the above mystery of animal flight (Dickinson, Lehmann and Sane, 1999; Ellington, 1984e; Ellington et al., 1996). Several unsteady mechanisms are found to explain the complex three dimensional flow structures associated with flapping wings: the stability of LEV; rotational circulation; the added mass inertia, the wake capture and the clap and fling mechanism.
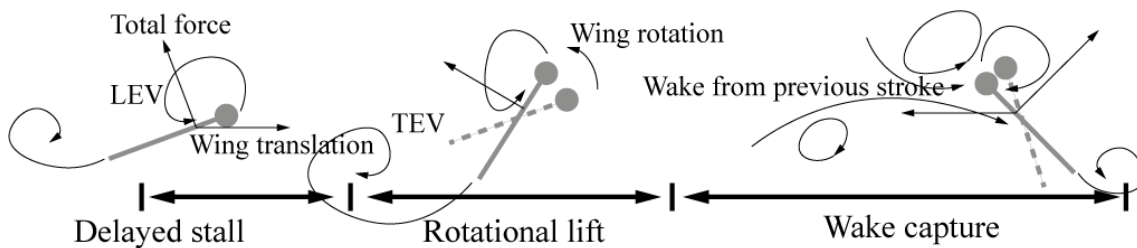
Figure 2-6 Basic unsteady aerodynamic mechanisms of insect flapping flight, adapted from (Dickinson and Dudley, 2009).

During the translational process of the flapping stroke, the flow separates at the leading edge of the wings and grows into a vortex that covers large part of the wing surfaces and merges with the tip vortex at wing tip, this vortex forms a low

pressure region on the upper surface of the wing and therefore increases lift. This flow mechanism for lift production is known as the stable LEV. The stable LEV provides the majority of augmented lift for insect flapping wings (about 80%). Ellington (Ellington et al., 1996) proposed that the stability of LEV is due to the spanwise flow that transports vorticity along the LEV core to the wingtip. In later investigations, it was noticed that revolving wings could also sustain stable LEV. Usherwood and Ellington (Usherwood and Ellington, 2002) found that the stable LEV exists on steadily revolving model hawkmoth (*Manduca sexta*) wing at *Re* on the order of 10^3. This indicates that a rotary wing with low aspect ratio at low *Re* (on the order of 10^3) can also sustain stable LEV and generate high lift force similar to the flapping wing during the translational process.

During the rapid rotation motion, the flapping wings experience a change in fluid force to a level beyond steady state values. When the wing rotates about the pitching axis while translating at the same time, flow around the wing deviates from the Kutta condition and the stagnation point moves away from the trailing edge. This causes a sharp, dynamic gradient at the trailing edge. As the fluids tends to re-establish the Kutta condition at the trailing edge, additional circulation will be generated on the wing. In other words, the wings generate a rotational circulation in the fluid to counteract the effects of rotation. Therefore, rotational forces will be generated that either add to or subtract from the net force due to translation, depending on the direction of rotation (Sane, 2003). This phenomenon is known as the 'Kramer effect' (Kramer, 1932), or alternatively as 'rotational circulation' (Sane and Dickinson, 2002) for flapping wings.

Another unsteady aerodynamic effect that affect insect flapping wings is the added mass inertia. When an insect accelerates its wings, it will set the surrounding air in motion, therefore the inertia of the wing is increased by the mass of the air that is accelerated (Dickinson, Lehmann and Sane, 1999). This apparent increase in wing mass is known as added mass inertia. This virtual

mass can be comparable to the wing mass itself for some insects (Ellington, 1984e).

During the reciprocating motion of flapping wings, the wings in the current half stroke enter into the wake shed in the previous half stroke, thus recapturing the shed vorticity and add to the wing's bound vorticity to enhance lift. This lift augmentation mechanism is known as 'wake capture'. Previous investigations using both experimental and numerical methods show that the wake capture of flapping wings serves as a way to recovers energy from the air that was lost during the previous stroke, which in turn improves the aerodynamic efficiency of force production (Birch and Dickinson, 2003; Dickinson, Lehmann and Sane, 1999; Srygley and Thomas, 2002).

The last unsteady aerodynamic mechanism that is thought to be exploited by some insects is the clap and fling mechanism. Weis-Fogh (Weis-Fogh, 1973) first observed this effect in experimental studies of flight characteristics of small wasp (*Encarsia Formosa*). In this hypothesis, the wings come together dorsally at the end of the upstroke to perform a 'clap', after the clap the wings 'fling' apart, the air is sucked in as the wings start to move downwards creating a bound vortex on each of the wings, which produces an instantaneous high lift force.

In the above unsteady aerodynamic mechanisms, the clap and fling does not apply to most insects. The most prominent aerodynamic mechanism for insect flapping wings at low *Re* is the stable LEV, which accounts for approximately 80% of lift enhancement (Sun, 2005), the remaining mechanisms are significant at the beginning and ending of each flapping half stroke, where the acceleration or deceleration of the wings are very large.

2.4 Aeroelasticity of Large and Micro Flyers

Aeroelasticity is concerned with the deformation of elastic structure interacting with airflow and the resulting aerodynamic forces. Depending on whether inertial forces are taken into account, it is further categorised by static and dynamic aeroelastic problems(Bisplinghoff, Ashley and Halfman, 1996). Static

aeroelasticity is concerned with the interplay of aerodynamics and elasticity; while dynamic aeroelasticity is further combined with dynamics, leading to dynamic problems such as aeroelastic flutter (Hodges and Pierce, 2014).

The aeroelastic phenomenon prevails in the world of flying vehicles and animals. The airframes of large aircraft undergo aeroelastic deformation under the large lift produced by their wings. Control effectiveness and flutter occur when the vibration of the wing structure interact with the aerodynamic force in undesirable ways. For civil aircraft, aeroelastic detrimental effects could result in undesirable effects or catastrophic failure of the aircraft (such as flutter), therefore, are of greatest concern for designers. On the other hand, for modern UAVs and MAVs, due to their high acceptable safety risk, aeroelastic beneficial effects can be used to exploit the potential of performances and structural weight saving. Design concepts that take advantage of light-weight, flexible structure to increase manoeuvrability and aerodynamic efficiency of aircraft have been investigated. Typical examples include the Active Flexible Wing program of NASA (1980's~1990's)(Pendleton, Lee and Wasserman, 1992), and the solar powered high-altitude long-endurance (HALE) air vehicle.

In the biological world, flying animals mastered aeroelasticity by manipulating their flexible wings in the unsteady flow. The wings of birds are covered by flexible feathers, stretch and deform whilst flying in a favourable manner, which increases aerodynamic efficiency as well as perform flight control. Insects on the other hand, fly in extremely low *Re*, the flexural pitching of their wing under aerodynamic and inertia forces helps the wings produce higher lift and consume less power. In this section, the physics of aeroelastic phenomena and effects are reviewed on the basis of both large manmade aircraft and small biological flyers.

2.4.1 Aeroelasticity of large aircraft

2.4.1.1 Classical aeroelasticity for aircraft

Conventionally the aeroelastic effects for aircraft are categorised into static and dynamic aeroelastic effects. The interplay of aerodynamic force with structural

restoring force of the airframe leads to static aeroelasticity. Several phenomena could occur for static aeroelasticity, including aerodynamic load redistribution, divergence and control system reversal.

In static aeroelasticity, the inertial force of the wing does not play any role. Traditional aircraft wing undergo bending and twisting deformation under aerodynamic load. Wing twist produces change of the local AoA of the airfoil. For swept-back wing, the deformation reduces the local AoA, whereas for swept-forward wing, it increases the local AoA. The change of the local AoA thus alters the distribution of the aerodynamic force along the wingspan of a flexible wing in comparison with a rigid wing. Figure 2-7 shows the redistribution of lift of a flexible wing compared with rigid wing due to static aeroelastic effect. The total lifts of the two wings (area under each respective curve) are equal, but the swept-back flexible wing has much larger AoA at wing root than the rigid wing. Lift effectiveness is defined as the ratio of the total lift of a flexible wing divide by the lift of the rigid wing with identical geometry and operating condition (AoA, dynamic pressure, etc.). Usually the lift effectiveness of a swept-back wing is less than unity, but for unswept wing it is greater than unity.

Divergence happens when the wing deformation couples with the aerodynamic force in a positive manner. For example, for unswept wing, the aerodynamic force produces a nose-up twist of the wing, which increases the local AoA, but the increase of the local AoA will in return yield greater aerodynamic force and torque, therefore, larger deformation is required to balance the torque increment. When the deformation of the wing structure builds up to a certain degree, aeroelastic divergence occurs and causes structure failure.
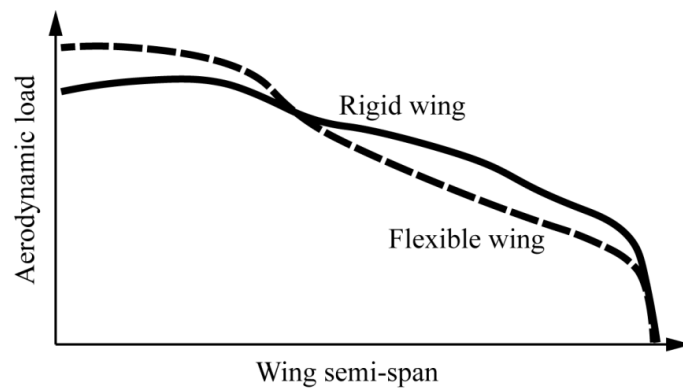
Figure 2-7 Flexible swept-back wing lift redistribution.

Control effectiveness is used to describe the ability of the control surface of the aircraft such as the aileron or rudder to produce control force or moment for the aircraft to perform manoeuvre during flight. Compared with a rigid wing, flexibility of the wing also affects the effectiveness of the control surface due to elastic deformation. For example, when the aileron was set to rotate down to produce a lift increment, the aerodynamic moment also increases and making the airfoil twist nose-down, which decreases the local wing AoA as well as the total lift and moment. The equilibrium of the elastic restoring moment and aerodynamic moment balances with each other. The resulting manoeuvre acceleration of the aircraft is therefore expected to be less than a rigid aircraft. Moreover, when the dynamic pressure at the situation is high and the airfoil structure is very flexible, the response of the aircraft to the control surface rotation can be completely nullified by the elastic deformation and even in the opposite manner.

For flying aircraft, the vibration of the structure interacting with aerodynamic force causes dynamic aeroelastic phenomena. The aerodynamic force involved in this situation is unsteady. Typically, the oscillation of the aerodynamic force can be induced by internal or external factors. The shed vortices of the lifting surface, aileron hinge, fuselage and blunt edges are the internal factors that cause the variation of the aerodynamic force of an aircraft, although usually small, at high AoA and high dynamic pressure, the unsteady variation of the aerodynamic force may cause transient dynamic response of the aircraft from

31

moderate to severe (i.e. buffeting). An external impulse such as the abrupt control moment or gusts usually produces large oscillation of the aerodynamic force and thus large transient response of the aircraft structure.

The most extreme case when the unsteady aerodynamic force couples with vibration of the aircraft structure is flutter. The physics of flutter is understood by the oscillatory unsteady aerodynamic force couples with the vibration mode of wing structure at a resonant frequency, where the input energy of the in-phase impulsive aerodynamic force cannot be damped off by structure and the out-of-phase aerodynamic damping force. The wing vibration thus absorbs energy from the surrounding airflow, and the amplitude of vibration build up rapidly to a degree of structure failure.
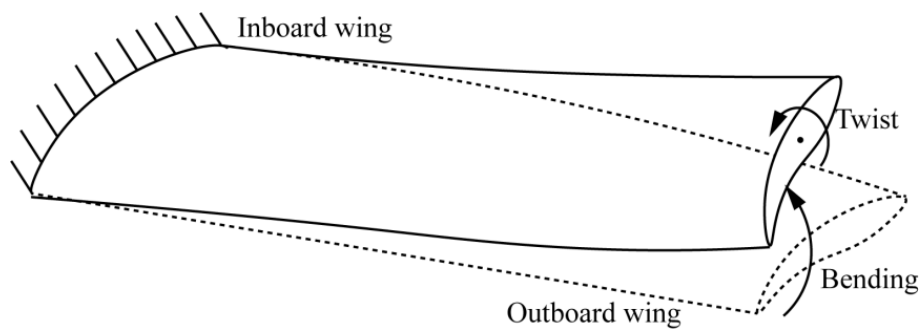
Figure 2-8 Bending and twist deformation of an aircraft wing.

There are usually multiple vibration modes of aircraft structure that couples with unsteady aerodynamic force leading to flutter. The most common case of the modes is the bending-torsion coupling of the aircraft wing. Other representative modes include: control surface coupling, i.e. control surface rotation-wing bending; empennage, i.e. fuselage torsion-tail torsion; stall, i.e. wing torsion; and body freedom coupling, i.e. wing bending-fuselage pitching (Wilson, 2002). In the classical bending-torsion case, the resonant natural frequencies of the two modes come closer to each other as the airspeed increases, as shown in Figure 2-9. At point A, the bending and torsion modes of the wing are decoupled. The disturbances in this situation decay with time. When the

dynamic pressure increases to point B, the disturbance produces harmonic oscillatory motion of the wing with fixed amplitude. When the two natural frequencies come further close to each other with the airspeed, the disturbance grows rapidly and flutter occurs at point C.
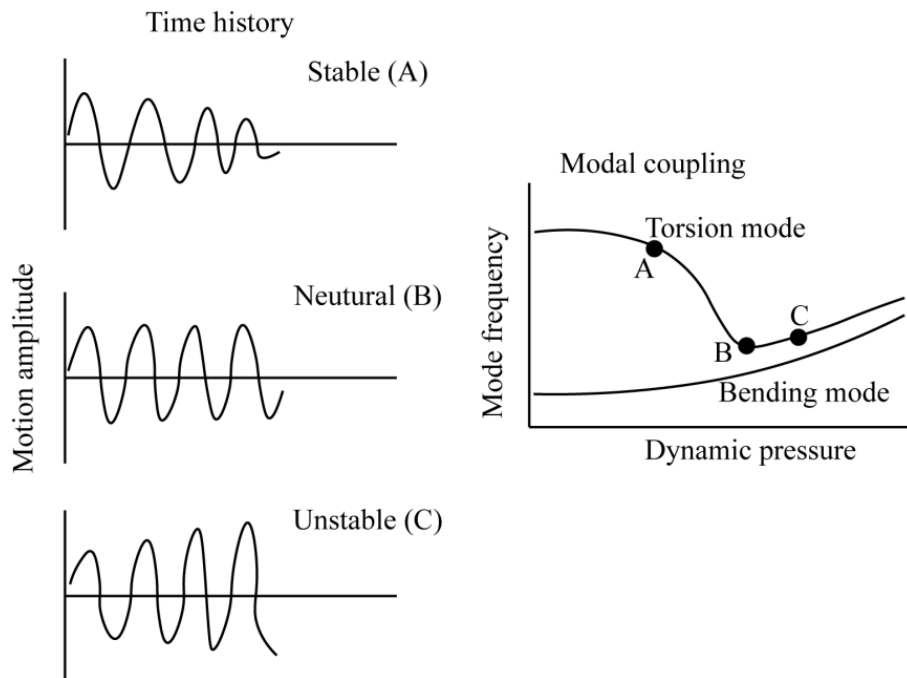
Figure 2-9 Bending-torsion coupling leads to flutter, adapted from (Ricketts, 1983).

The mechanism of this bending-torsion instability for aircraft wings can be explained in a more delicate manner. Assuming a steady freestream with constant velocity during aircraft cruising, the torsional oscillation of the wing changes the AoA of the wing periodically thereby produces an oscillatory aerodynamic force in the same frequency with the structural torsional vibration. The vertical displacement of the wing due to bending is therefore under forced vibration by the oscillatory lift. In this situation, the condition that leads to flutter is therefore that the frequency of the oscillatory impulsive force approaches the natural frequency of the structure (bending mode), which is expected to give the largest amplitude of the dynamic system.

2.4.1.2 Aeroelasticity of highly flexible aircraft

The recent development in UAVs and MAVs has led to air vehicle design using light weight and highly flexible structures. The aeroelastic problem for these highly flexible aircraft differs from the classical aircraft. For example, the rigid-body motion and the dynamics of structure of highly flexible aircraft can be tightly coupled, leading to complex dynamic behaviour which affects the performance of the air vehicles significantly (Livne, 2003; Livne and Weisshaar, 2003). A representative example of highly flexible aircraft is the solar powered NASA Helios prototype UAV. The Helios UAV is developed for conducting long duration and high altitude atmospheric research. It features light wing with very high aspect ratio to maximize the lift to drag ratio for aerodynamic efficiency. The long and slender wing is highly flexible, exhibiting large deformations under normal operating load. In the flight experiment at Hawaii on 26 June 2003, the aircraft aeroelastic wings (body) entered an unstable phugoid mode, experienced abnormally-high dihedral deflections, and broke apart. The coupled behaviour of flight dynamics and aeroelasticity plays central role in the Helios mishap, as recommended by the NASA investigation panel (Su and S. Cesnik, 2011): "(It is necessary to) develop more advanced, multi-disciplinary (structures, aeroelastic, aerodynamics, atmospheric, materials, propulsion, controls, etc.) 'time-domain' analysis methods appropriate to highly flexible, 'morphing' vehicles."

The analysis of nonlinear aeroelastic aircraft have been previously conducted by several researchers. Wang et al. (Wang et al., 2006) used a time-domain aeroelastic framework to analysis the aeroelastic behaviour of HALE aircraft with high aspect ratio and highly flexible wing. They used a geometrically exact nonlinear beam model developed by Hodges et al. (Hodges, 1990, 2003; Popescu and Hodges, 2000; Yu et al., 2002) combined with unsteady vortex-lattice method (UVLM) to model the aircraft flexible wing. Their results indicate that the aeroelastic stability of the HALE wing depends on the deformation of the wing shape. At small or moderate deformation, the HALE wing is aeroelastically stable but it becomes unstable when the deformation of the wing is large. Love et al. (Love et al., 2005) studied the body-freedom flutter of a

high-aspect-ratio flying wing configuration aircraft. Their results indicate that the body-freedom flutter may happen for low altitude flight and suggested that active flutter suppression need be considered. Gu et al. (Yingsong, Zhichun and Shun, 2015) studied body-freedom flutter of aeroservoelastic system of a Blended-wing-body Model. They found that wing stiffness has strong influence on the closed loop flutter characteristics and that while the static unstable unaugmented Blended-wing-body aircraft can be stabilized by proper designed flight control system, the closed loop body freedom flutter speed is still quite low and needs further consideration in flight control system synthesis. Shearer and Cesnik (Shearer and Cesnik, 2007; Shearer and S. Cesnik, 2008) analysed the dynamic responses of very flexible aircraft using geometrically nonlinear formulation, coupled with a finite state aerodynamic model and nonlinear rigid body equations. Their results show that the vehicle trajectories obtained by nonlinear rigid-body model and linearized model differ significantly from the ones based on fully nonlinear model for very flexible aircraft. Therefore, fully nonlinear simulations that take into account the coupling of rigid body and flexible structures are necessary to properly predict the vehicle trajectories.

2.4.2 Aeroelasticity of biological flyers

One intriguing feature of animal flight is that their wings are highly flexible. During flight, the wings of birds and insects deform continuously as a result of inertial and fluid dynamic forces, the deformation changes the instantaneous wing shape and AoA, and thus the aerodynamic forces on the wing. A typical example is the wing of insects. During flight, insect wings need to twist continuously in the up and downstroke, reversing the wing surfaces up and down to form a positive AoA. Experimental tests have shown that the torsional wave of an insect wing propagates along the trailing edge from tip to root (Ennos, 1988; Mountcastle and Daniel, 2010), indicating that pitching reversal is driven passively by wing inertia and aerodynamic forces. This coupling of the elastic structure and fluid flow is essentially complicated by the nonlinear rigid body motion of the wing. Its implication on the performance of natural flyers remains an active research field.

Katz and Weihs (Katz and Weihs, 1978) numerically modelled a flexible foil in large amplitude heaving and pitching motion in inviscid flow, they found that flexibility can increase propulsive efficiency by 20% compared with a rigid foil. Shyy et al. (Shyy, Jenkins and Smith, 1997) studied the lift-to-drag ratio of cambered airfoil with different flexibility, immersed in an oscillating freestream. They found that flexible membrane wing exhibits better performance at higher AoA than the rigid wing; and a hybrid wing (combination of rigid and flexible wing) exhibits high lift-to-drag ratio at all AoA compared to the flexible and rigid wing and is not sensitive to the freestream velocities. From this, they concluded that modulating the flexibility of the wing can improve aerodynamic performance. Lian et al. (Lian et al., 2003) numerically modelled three-dimensional flexible flapping wings and found that wing flexibility can delay the appearance of stall to higher AoA. Prempraneerach et al. (Prempraneerach, Hover and Triantafyllou, 2003) experimentally studied the effect of chord-wise flexibility to flapping foil, they found that propulsive efficiency of the flexible foil is increased up to 36% compared to a rigid foil. Alben (Alben, 2008) studied the thrust generation of a flexible body pitching periodically at the leading edge, he found that the propulsive efficiency is related with the resonance bending mode and affected by the bending rigidity of the wing. Moore (Moore, 2015) studied the effect of chord-wise distribution of wing stiffness to wing aerodynamic performance. He found that focusing wing flexibility at the leading edge maximizes the thrust production. Shoele and Zhu (Shoele and Zhu, 2013) studied the aerodynamic performance of insect wings with non-uniform flexibility along chord-wise, they found that stiffening the leading edge of the wing produces significantly higher lift force with less consumed power, in a wide range of kinematic parameters. Nakata and Liu (Nakata and Liu, 2012) used a fluid–structure interaction scheme to analysis the hawkmoth wing kinematics. They found that wing flexibility can increase both stroke-averaged lift production and efficiency, compared with rigid wings.

Alongside the numerous numerical studies on flexible flapping wings, experimental biologists have also provided many investigations to reveal the role of flexibility for biological flyers. Zhao et al. (Zhao et al., 2010) used

dynamically scaled models of insect wing (*Drosophila*) with different rigidity on the trailing edge to measure the aerodynamic force production. Their kinematics mimics insect flight at Reynolds number (*Re*=2000). They found that the lift production decreases monotonically with the increase of flexibility of the wing. Tanaka et al. (Tanaka, Whitney and Wood, 2011) used a piezo-electric actuated robotic flapping mechanism to measure forces on an at-scale model wing with similar average flexural stiffness to a natural insect wing. They found that the flexible wing generates lower mean lift than a rigid carbon fibre wing flapped with the same actuation pattern. On the contrary, Mountcastle and Combes (Mountcastle and Combes, 2013) directly tested the lift force of live bumblebees with flexible (original) wings and artificially stiffened wings. By applying a micro-splint to the flexible vein joints of the live bee wings, the flexural stiffness of the wings increased up to 37.6% with minimal additional mass. They found that the maximum lift of the stiffened wings show 8.6% reduction compared with the flexible wings, which implies that the flexible wings of bumblebees, as well as other flying animals, plays important role in maximizing the aerodynamic force production and therefore has strong implication on their ecological fitness.

3 DESIGN, OPTIMIZATION AND AEROELASTIC ANALYSIS TECHNIQUES FOR LARGE AIRCRAFT

In this chapter, the design, analysis and optimization techniques for large aircraft structures and aeroelasticity are presented based on a few case studies including a commercial composite aircraft wing and a Blended-wing-body fuselage. This study aims at presenting the state-of-art design and analysis techniques for large aircraft. For this purpose, the commercial FE solver NASTRAN is used as the primary tool for structure and aeroelastic analysis; the software package MATLAB is used as optimization toolbox. Additionally, an analytical curved beam model is developed for the analysis and optimization of the non-circular BWB fuselage cross section.

3.1 FE Analysis of Large Aircraft Wing

3.1.1 Model wing information

In this study, a composite commercial aircraft wing is chosen for investigation. The baseline composite wing FE model is shown in Figure 3-1. The wing box structure can be divided into six different components, the wing-stub-box, the inner-wing-box, the landing-gear-box, the outer-wing-box, the aileron-box and engine and pylon.
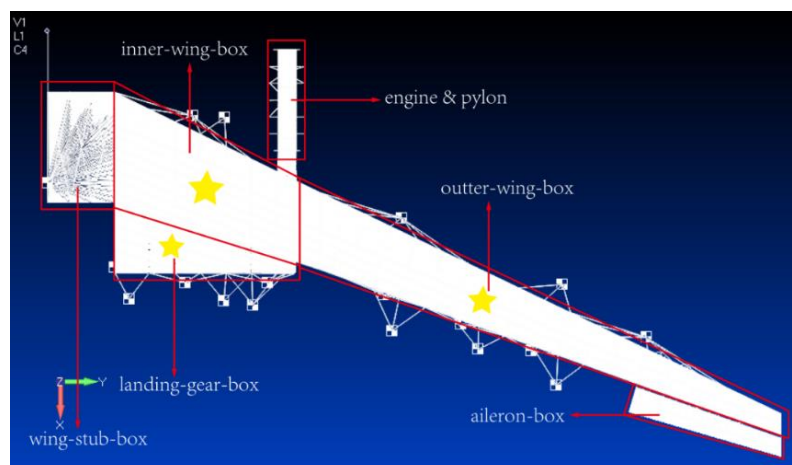
Figure 3-1 FE model of composite aircraft wing.

The aircraft wing model has half span 15.21m and total structural weight 1800kg. With regard to the mass distribution of the model, half of the fuselage weight and the engines, landing gears, control surfaces and fuel were taken into account. This has given rise to a total weight of 29 tons for the whole FE model. The mass for half of the fuselage was placed at the centre of the fuselage near the root of the starboard wing. The total non-structural mass of a single wing is 27.2 tons which includes half of fuselage, pylon, nacelle, engine, landing-gear, actuation systems and fuel. The general geometric and mass information of the baseline wing model is provided in Table 3-1.

Table 3-1 Particulars of the baseline composite wing.

Wing Aspect Ratio (AR)	10
Wing area (including left wing)	92.25 m^2
Wing half span	15.21 m
Wing structural weight	1800 kg
Lumped mass subtotal (half fuselage, engine, landing gear and fuel)	27200 kg

3.1.2 Baseline wing structure properties

The FE model of the wing was created using 25543 structural elements including shell and bar elements for FE analysis in NASTRAN. Bar elements of T-shape cross sections were used to model all of the spar caps, stringers, rib flanges and web stiffeners. The cross sections of the spars and stringers in the model have the same constant dimensions from root to tip. Plate elements with varying degrees of complexities were used to model the skin covers, spar and rib webs. Furthermore, the wing skins were modelled by using composite material in quasi-isotropic layup (Ex=Ey). Material with equivalent properties like aluminium alloy was employed for the stiffeners which were modelled by bar elements. As for the pylon, isotropic aluminium material was utilised in a similar manner. A brief summary of the material properties used in modelling the wing is given in Table 3-2.

Table 3-2 Material properties of different parts of the wing model.

Type	Location	Density (kg/m³)	E (Pa)		G (Pa)		Nu
Isotropic	Beams	2700	7.0e10		2.69e10		0.3
Quasi-isotropic	Skins	Density (kg/m³)	Ex (Pa)	Ey (Pa)	G (Pa)	Exy (Pa)	G13 (Pa)
		1580	6.32e10	6.32e10	2.21e10	1.90e10	0

The baseline wing is divided into seven parts from wing tip to root. Each part of the wing box has upper & lower skin and front & rear spar. Part six and part seven also include the landing-gear box upper, lower skin and rear spar. The panel thicknesses (including skin panels and web panels) for the wing are shown in Table 3-3 and Figure 3-2. The cross section dimension of the beam elements are shown in Figure 3-3 and Table 3-4.

Table 3-3 Panel thicknesses for the baseline wing (mm).

Location	Upper skin	Lower skin	Front spar web	Rear spar web	Landing gear box		
					Upper skin	Lower skin	Rear spar web
Skin part 1	3.660	3.660	3.660	3.660			
Skin part 2	4.392	4.392	4.392	4.392			
Skin part 3	5.124	5.124	5.124	5.124			
Skin part 4	6.222	6.222	5.856	6.222			
Skin part 5	6.954	6.954	6.954	6.954			
Skin part 6	7.686	7.686	7.686	7.686	7.686	7.686	7.686
Skin part 7	8.418	8.418	8.418	8.418	8.418	-	8.418
Rib web panels (28)				2.928			
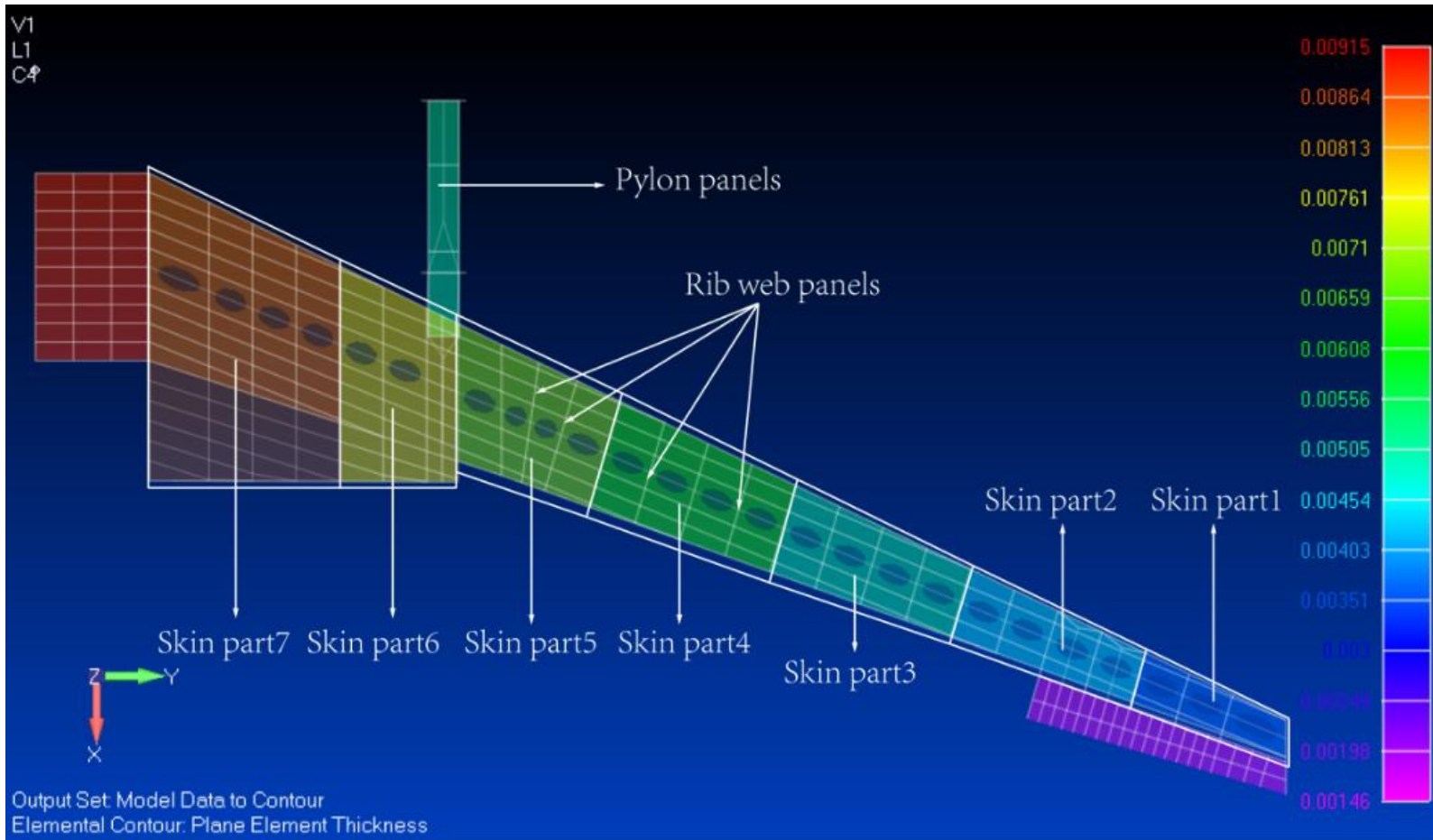
Figure 3-2 Panel thicknesses distribution for the baseline wing.
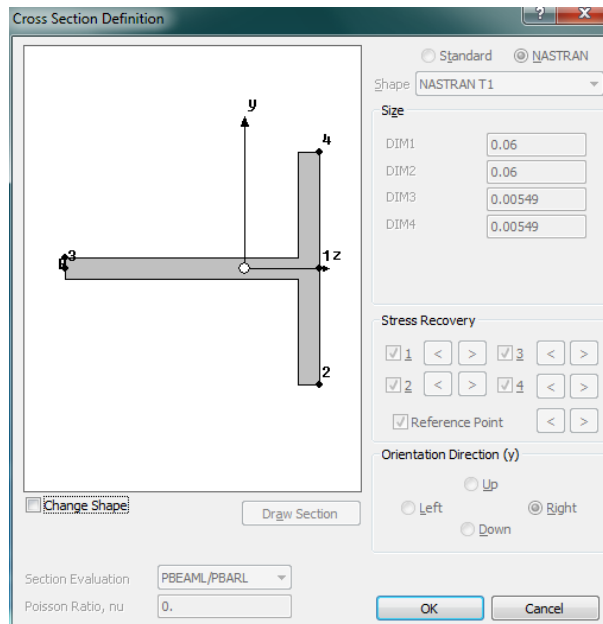
Figure 3-3 Stringers, spars, ribs and web stiffeners elements in the baseline wing.

Table 3-4 Cross section information of stringers, spars, ribs and web stiffeners elements for the baseline wing.

T section height	60 mm
T section width	60 mm
Height of flange	5.49 mm
Width of web	5.49 mm
Cross section area	658.8 mm^2

3.1.3 Baseline wing NASTRAN analysis

Based on the FE model, the static stress, strain, buckling and modal, flutter analyses of the baseline wing are carried out. In this analysis, the baseline wing is fixed at the root (the inner wing chord section of the inner-wing-box) so as to make it a cantilever. The static analyses (stress, strain and buckling) are performed under load factor 2.5 using the commercial solver NASTRAN. For this case, both aerodynamic load and inertia load are applied. The distributed

aerodynamic load along the span has a total value of 710000N (approximately 2.5 times the total weight of the wing), and the applied inertia load (vertical acceleration) is -2.5g, i.e. 24.5m/s^2. The applied load distribution on the wing is shown in Figure 3-4.
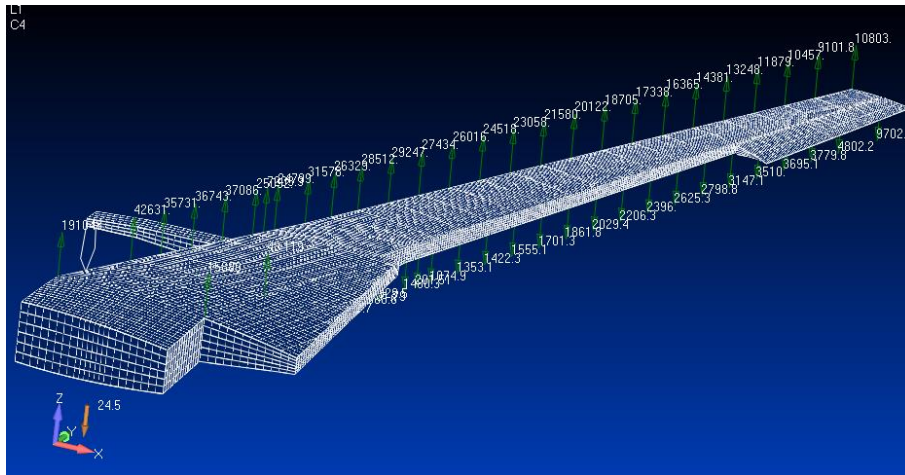
Figure 3-4 Applied load distribution on the wing for 2.5g load factor.

3.1.3.1 Static analyses results

The static stress, strain and buckling analyses results for the baseline wing are summarized in Table 3-5. The first buckling location and the stress state under buckling load at the location are shown in Figure 3-5.

Table 3-5 Static stress, strain and buckling analyses results for the baseline wing.

Applied load factor	2.5g upward vertical
Wing tip displacement	1.08 m
Maximum major principal stress	352 MPa
Maximum major principal strain	6740 $\mu\varepsilon$
First buckling eigenfactor	1.2
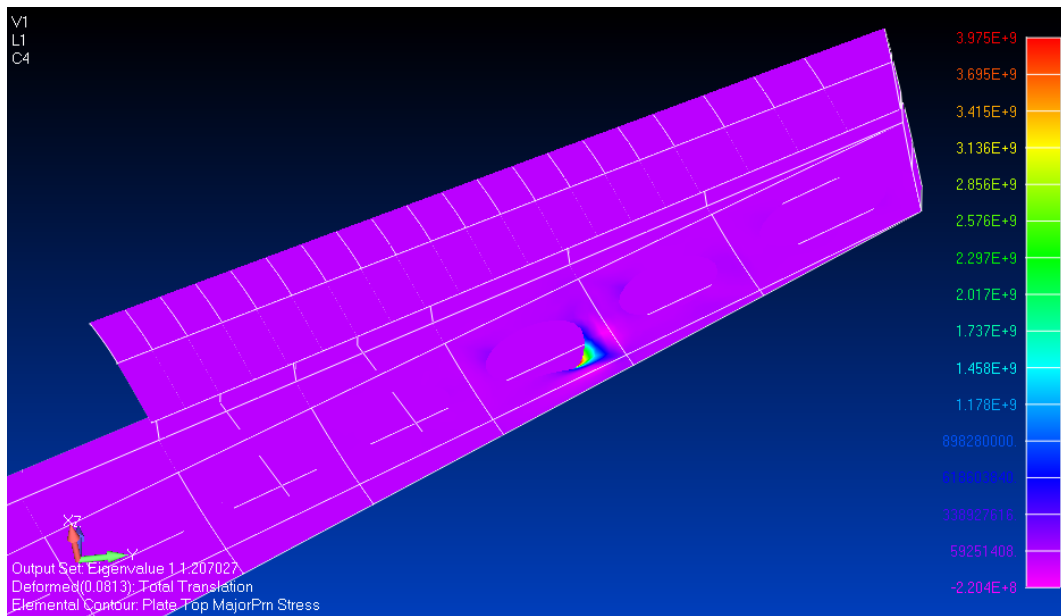
Figure 3-5 First buckling location of baseline wing, maximum principal stress at buckling location 397 MPa.

From Table 3-5, it is noted that for the applied 2.5g load, the maximum strain of the baseline wing exceeds the damage tolerant limit. However, the maximum strain mainly occurs locally near the man-hole area of the lower skin, which for a practical wing may be reinforced to reduce the high strain in this area.

3.1.3.2 Modal and flutter analyses results

The modal and flutter analyses of the baseline wing is performed under the same boundary condition as the static analyses. The normal modes of the baseline wing are summarized in Table 3-6.

The flutter analysis of the baseline wing is carried out at zero altitude and zero Mach number (artificial settings in NASTRAN). The flutter results are summarized in Table 3-7, the velocity-damping (V-g) and velocity-frequency (V-*f*) graphs for flutter are shown in Figure 3-6 and Figure 3-7.

From Figure 3-6 and Figure 3-7, it is noted that the flutter speed of the baseline wing is 306 m/s at frequency 3.72 Hz, dominated by the pitching mode of the engine & pylon. However, Figure 3-6 shows that the engine & pylon pitching

mode has consistently very small damping for the whole range of investigated velocity. Therefore, an alternative divergence velocity on the V-g plot dominated by the second bending mode of the wing is selected as the flutter speed. This flutter speed is at 405 m/s and the frequency is 8.57 Hz.

Table 3-6 Normal modes of the baseline wing.
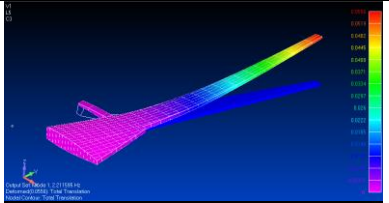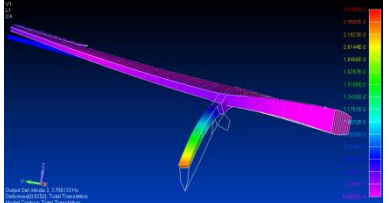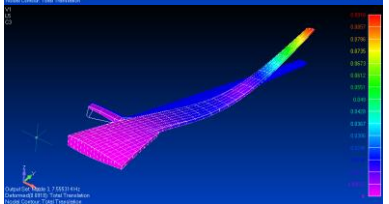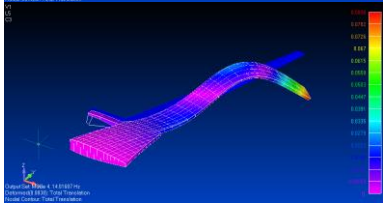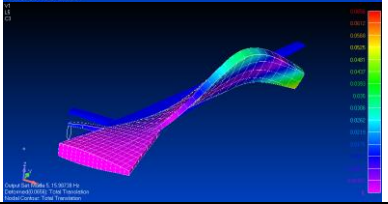
Mode No.	Frequency (Hz)	Mode shape
First Bending (1st mode)	2.12	
Pylon pitching (3rd mode)	3.76	
Second bending (7th mode)	7.19	
Third bending (8th mode)	11.38	
First torsion (9th mode)	13.96	

Table 3-7 Flutter analysis results of the baseline wing.

Dominating modes	Flutter speed (m/s)	Flutter frequency (Hz)
Second bending (7th mode)	405	8.57
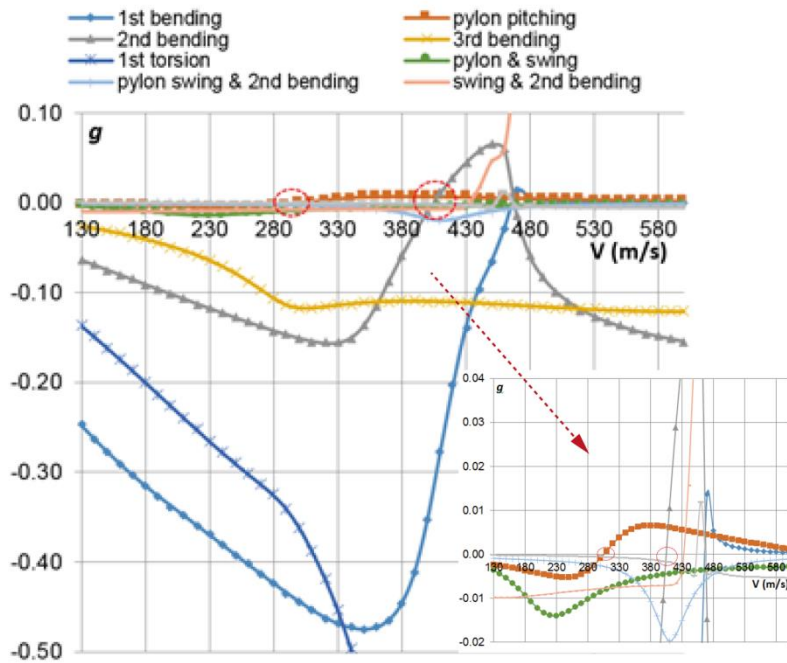
Figure 3-6 V-g plot of flutter for the baseline wing.
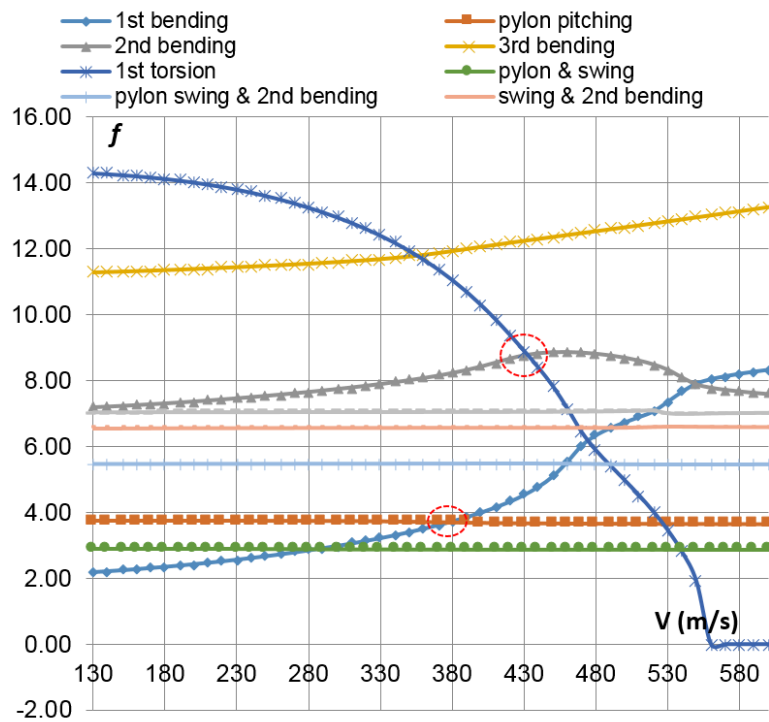
Figure 3-7 V-*f* plot of flutter for the baseline wing.
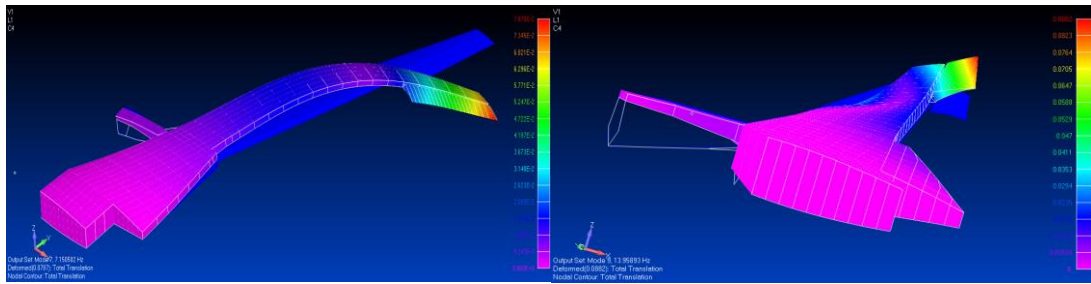
Figure 3-8 Dominating modes that lead to flutter: second bending (left) coupled with first torsion (right) mode of the baseline wing.

3.2 Structure and Aeroelastic Optimization of Large Aircraft Wing

3.2.1 Optimization method

Based on the analyses for the baseline aircraft wing, an optimization study is then carried out. In this optimization study, the aim has been set to optimize the wing box structure, i.e. the inner-wing-box, the outer-wing-box and the landing-gear box, subject to static (strength and buckling) and aeroelastic (flutter speed) constraints. The structure properties of the wing-boxes including skin & web thicknesses, beam cross section area and the composite laminate layup of the wing skin are all set as optimization variables.

In this optimization, the objective is to find a design of the composite wing with minimal weight that satisfies the static strength, buckling and aeroelastic constraints. The initial optimization target is therefore to minimize the wing structural weight. For this weight optimization, the optimization variables are set as the skin, web thicknesses (t) and the beam cross section areas (A). Alternatively, for the composite wing skins, the laminate layups of the wing can be tailored to improve the aeroelastic response. Therefore, a secondary optimization can be carried out which takes the wing skin laminate layups as optimization variables and the optimization target becomes to maximize the flutter speed while maintaining the wing structural weight of the design.

In this investigation, the wing structure optimization has been divided into two steps. The first step multi-constraint optimization is aimed at minimizing the wing structural weight subject to static strength and aeroelastic constraints. In this step, the panel thicknesses and beam cross section areas are set as the design variables, the cross section shape of the beam elements (relative dimensions of T section height and width) are kept unchanged. In addition to the first step weight optimization, an aeroelastic tailoring using the skin laminate layups as design variables is carried out. This step of optimization is aimed at maximizing flutter speed for a given wing design.

In order to make use of the available high-fidelity tools and the existing models, an FEM-based optimization program using the structure solver NASTRAN and the numerical tool MATLAB for the wing is developed. The program makes use of the MATLAB function (fmincon) as the optimizer, while the structure calculations of the wing FE model are carried out using NASTRAN. The MATLAB function (fmincon) is a gradient based optimizer, that solves the following problem,

$$\min_{x} f(x) \ such \ that \begin{cases} c(x) \leq 0 \\ lb \leq x \leq ub \end{cases} \qquad \textbf{(3-1)}$$

where, $f(x)$- nonlinear objective function

$c(x)$- nonlinear constraint functions

lb, ub- lower and upper bounds for variables

In the optimization program, the objective is set to minimize the wing weight or maximize the flutter speed; the skin, web thicknesses and the beam cross section areas or the wing skin laminate layups are the variables; the static stress, strain, buckling eigenfactor and flutter speed are set as nonlinear inequality constraints.
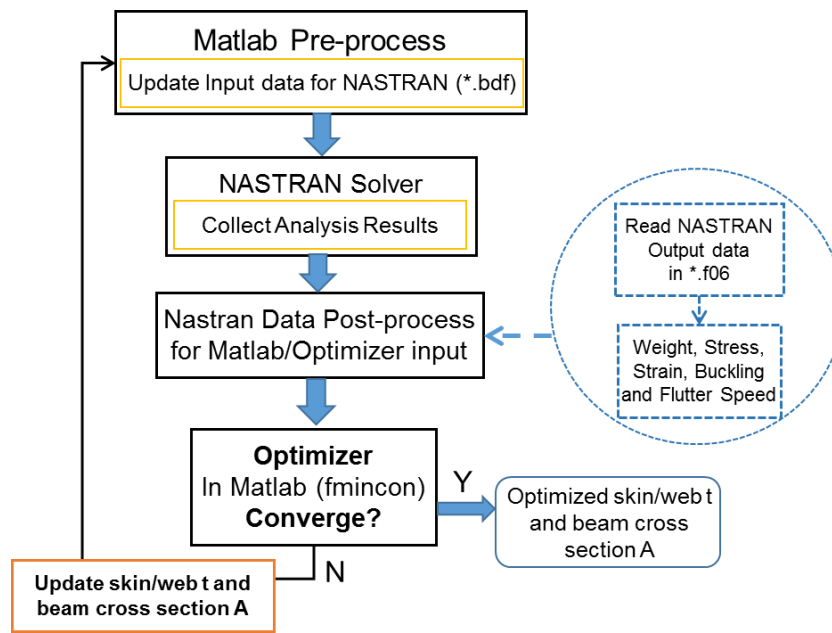
Figure 3-9 Flow chart for FEM-based weight optimization for target wing.
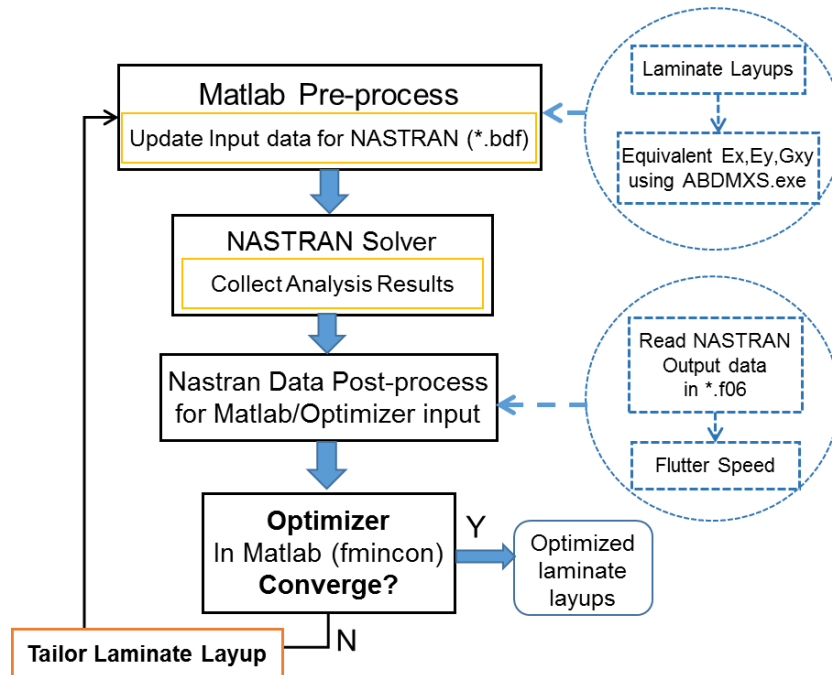
Figure 3-10 Flow chart for FEM-based aeroelastic tailoring of composite laminate layups for target wing.

For aeroelastic tailoring of the wing, an in-house program 'ABDMXS.exe' is used to transform the elastic properties of single lamina layers into the

equivalent elastic properties of the laminate skins. Figure 3-9 and Figure 3-10 summarizes the flow of data for the optimization program in the weight optimization and aeroelastic tailoring, respectively.

3.2.2 Optimization results

3.2.2.1 Weight optimization results

In this optimization, the wing structural weight is set as the objective function; the skin, web thicknesses (t) and the beam cross section areas (A) are set as the optimization variables. From the FE model of the baseline wing, the total number of design variables for the first step optimization, including the panel thicknesses and beam cross section areas on the inner-wing-box, outer-wing-box and landing-gear box is 296. The optimization constraints are the static stress, strain, buckling eigenfactor and the flutter speed. It should be noted that in this optimization, it is assumed that the wing skin and web laminate layups are not changing with the wing skin or web laminate thicknesses, therefore, the equivalent elastic properties of the composite wing skin and web are kept the same in this optimization. A total number of 296 design variables are optimized in this case study, consisting of 67 panel thicknesses (Skin panels and web panels) and 229 beam cross section areas. A summary for the optimization setting is shown in Table 3-8.

Table 3-8 Summary of weight optimization settings for baseline wing.

Optimization objective	Minimize wing weight
Optimization variables	Skin, web T and beam cross section A (No. of panel elements: 67 No. of beam elements: 229)
Constraint 1: major principal stress	≤ 400 Mpa
Constraint 2: major principal strain	≤ 4000 $\mu\varepsilon$
Constraint 3: 1st buckling eigenfactor	≥ 1
Constraint 4: flutter speed	≥ 400 m/s
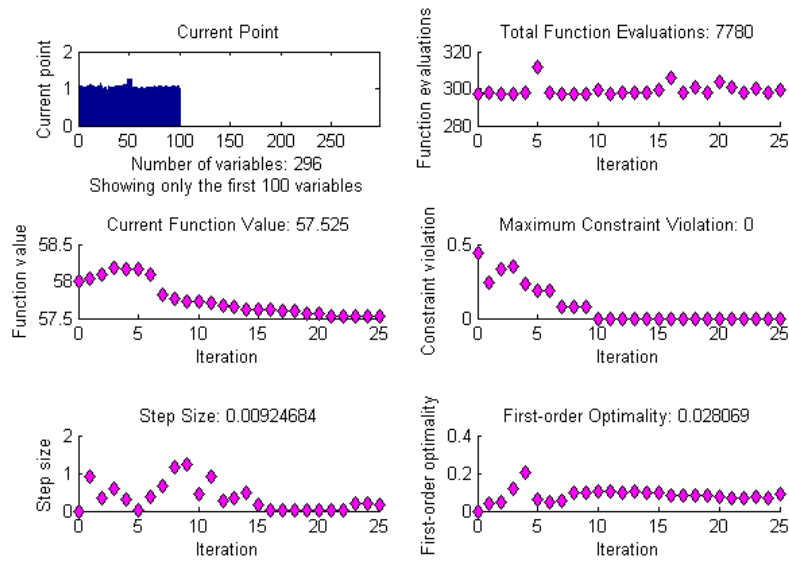
Figure 3-11 Convergence history for weight optimization, function value indicates normalized wing weight.

Based on the above setting, the weight optimization for the baseline wing is carried out. After 26 steps of calculations, the optimizer converged. The convergence history of the program is shown in Figure 3-11.

In Figure 3-11, the current point indicates the current values of skin, web thicknesses and the beam cross section areas (all variables are normalized as one for baseline wing). The function value is the total weight of the wing FE model (divided by 500). The result shows that the structural weight of the wing is reduced by 242 kg (13%) in this optimization. The optimized skin thickness is shown in Table 3-9 and Figure 3-12, below.

As shown in Figure 3-12, after the weight optimization, the upper skin, front spar and rear spar panel thicknesses reduced, but the lower skin thickness of the wing is increased, especially on the middle parts of the wing, i.e. part 4~6. This may be due to the large strain near the man-hole area of the baseline wing at these locations, which exceeded the strain constraint of 4000 $\mu\varepsilon$ of this optimization.

Table 3-9 Optimized skin thicknesses of the wing (mm).

Panel location	Upper skin	Lower skin	Front spar web	Rear spar web	Landing gear box		
					Upper skin	Lower skin	Rear spar web
Skin part1	1.745	3.614	2.854	2.473			
Skin part2	3.142	4.564	3.308	2.910			
Skin part3	4.363	6.237	3.814	3.447		/	
Skin part4	5.318	10.280	4.600	4.227			
Skin part5	6.633	14.077	5.095	4.783			
Skin part6	5.478	12.286	5.928	6.457	5.832	6.841	6.417
Skin part7	5.579	8.667	7.373	6.313	5.234	-	6.868
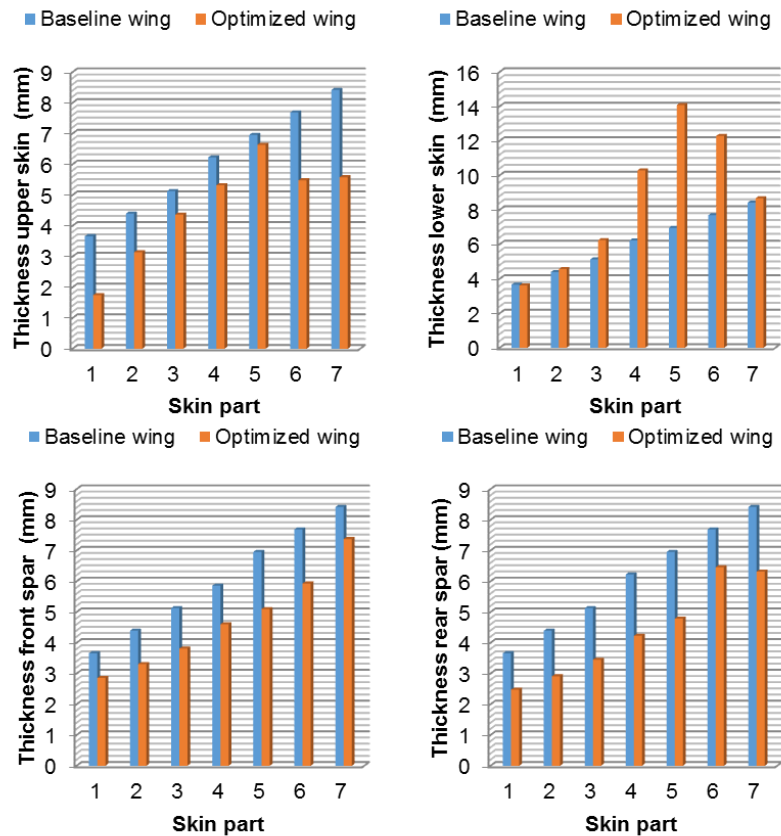
Figure 3-12 Comparison of skin thicknesses of baseline wing and optimized wing: upper skin, lower skin, front spar and rear spar.

Based on the optimized FE model of the wing, the static stress, strain, buckling and modal, flutter analyses of the optimized wing are further carried out. The

comparison of the optimized wing and baseline wing analyses results are summarized in Table 3-10.

Table 3-10 Comparison of static and aeroelastic response of the baseline and optimized wing.

FE model results	Baseline wing	Optimized wing
Structural weight	1800 kg	1558 kg (13% weight reduction)
Maximum major principal stress (2.5g load)	352 MPa	207 MPa
Maximum major principal strain (2.5g load)	6740 $\mu\varepsilon$	3740 $\mu\varepsilon$
First buckling eigenfactor (2.5g load)	1.20	1.14
Flutter speed	405 m/s	608 m/s

As shown in Table 3-10, the static stress and strain for the optimized wing is reduced significantly. In particular, the maximum major principal strain under 2.5g load factor has been reduced to 3740 $\mu\varepsilon$, which is below the damage tolerant limit. Both the baseline wing and the optimized wing has buckling eigenfactor above one, therefore, no buckling occurs at the applied 2.5g load. Furthermore, the flutter speed of the optimized wing is increased significantly.

Figure 3-13 shows the comparison of strain distribution of the baseline wing with the optimized wing. Figure 3-14 shows the first buckling locations of the respective wings. It is noted that the maximum strain for both the baseline wing and the optimized wing are near the man-hole area on the lower skin. However, for the baseline wing, the maximum strain is localized at the kink area; while for the optimized wing, the maximum strain is evenly distributed on each part of the lower skin.

The modal results comparison of baseline wing and optimized wing is shown in Table 3-11. The velocity-damping (V-g) and velocity-frequency (V-f) graphs for flutter of the optimized wing are shown in Figure 3-15 and Figure 3-16.
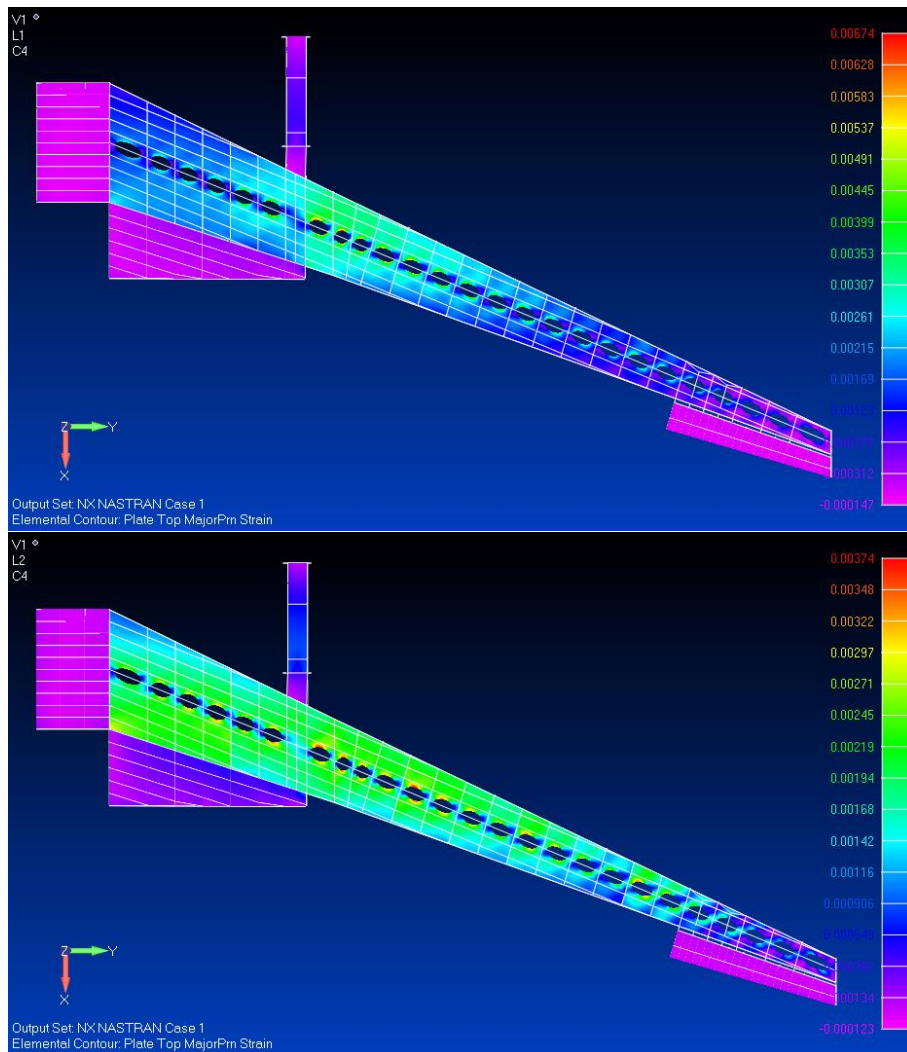
Figure 3-13 Comparison of strain distribution of baseline wing (up) with the optimized wing (down).
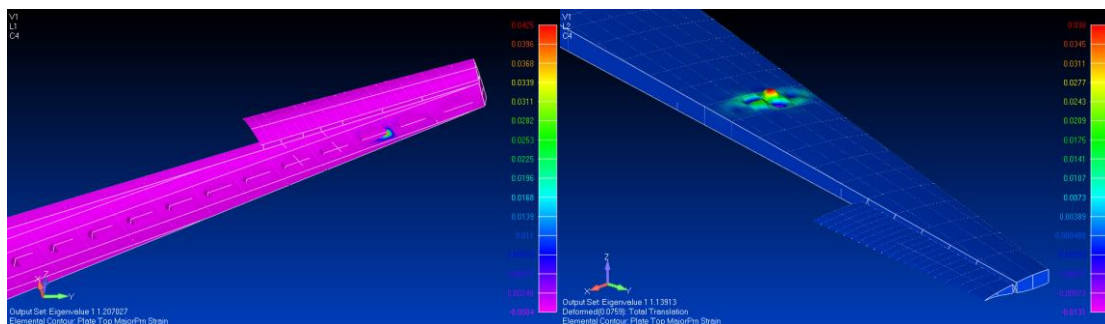
Figure 3-14 First buckling location of baseline wing (left) and the optimized wing (right).

Table 3-11 Normal modes comparison of the baseline wing and the optimized wing.

FE model results	Baseline wing	Optimized wing
First Bending	2.12 Hz (1st mode)	2.18 Hz (1st mode)
Pylon pitching	3.76 Hz (3rd mode)	3.69 Hz (3rd mode)
Second bending	7.19 Hz (7th mode)	7.05 Hz (7th mode)
Third bending	11.38 Hz (8th mode)	10.98 Hz (8th mode)
First torsion	13.96 Hz (9th mode)	14.17 Hz (10th mode)

In Table 3-11, it is observed that the normal modes of the optimized wing are similar to the baseline wing, the pylon pitching and second bending mode frequencies decrease slightly, while the first torsion mode frequency increase slightly. Figure 3-15 and Figure 3-16 shows that the dominating modes for flutter of the optimized wing are the same with the baseline wing (shown in Figure 3-6 and Figure 3-7), where the pylon pitching dominated mode leads to flutter speed of 395 m/s and flutter frequency 3.64 Hz, and the second bending dominated mode leads to flutter speed of 608 m/s and flutter frequency 8.20 Hz. Also, it is noted that the coupling modes for flutter of the optimized wing has changed to the coupling of second bending with first bending, in contrast to the baseline wing which was second bending coupled with first torsion. Both the pylon pitching and second bending dominated flutter speed of the optimized wing increased significantly compared to the baseline wing.
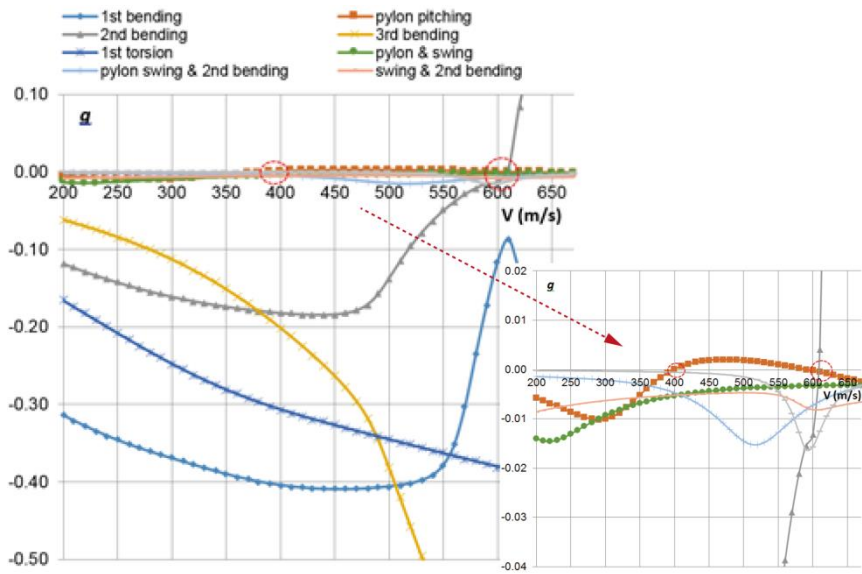
Figure 3-15 V-g plot of flutter for the optimized wing.
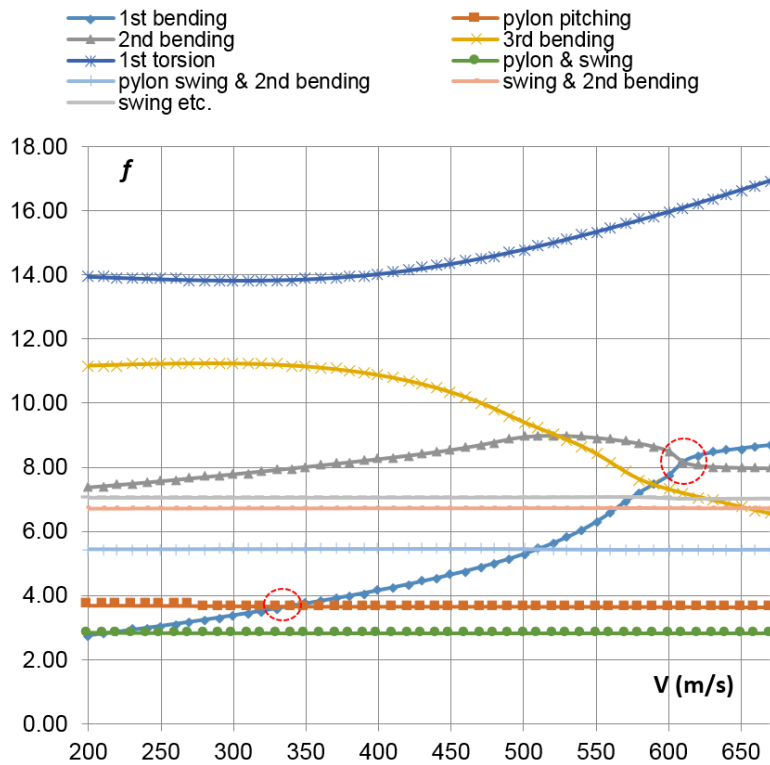
Figure 3-16 V-*f* plot of flutter for the optimized wing.

56

3.2.2.2 Aeroelastic tailoring results

One advantage of using the composite skin and web for aircraft wing design is that the laminate layups can be tailored to modify the stiffness of the wing structure, which can be used to optimize the dynamic response, especially the flutter response of the wing. In this study, the laminate layups of the composite baseline wing skins are taken for aeroelastic tailoring. As shown in Figure 3-2, the composite wing skin is divided into 7 parts; each part of the skin consists of upper and lower skin, front and rear spar web, and additionally the skins and webs of the landing gear box on the inner wing. Each composite skin of the wing has different number of layers; there are totally 572 ply angles to optimize. In this study, firstly, an aeroelastic tailoring study for maximum flutter speed for all the laminate layups (572 ply angles) is carried out. Subsequently, in order to investigate the effect of different parts of the wing skins for the flutter behaviour of the wing, the strategy of optimizing the skin layups independently at different parts is applied, which greatly saves the computational time and allows to identify the most sensitive part of the wing skin that influences the wing flutter characteristics. A summary for the optimization setting is shown in Table 3-12.

Table 3-12 Summary of aeroelastic tailoring settings.

Optimization objective	Maximize flutter speed
Optimization variables	Skin composite laminate layups of different wing parts Total number of ply angles: 572
Optimization constraint	No constraints

Based on the above settings, the aeroelastic tailoring for the baseline wing is carried out. The convergence history of the program of the skin is shown in Figure 3-17.
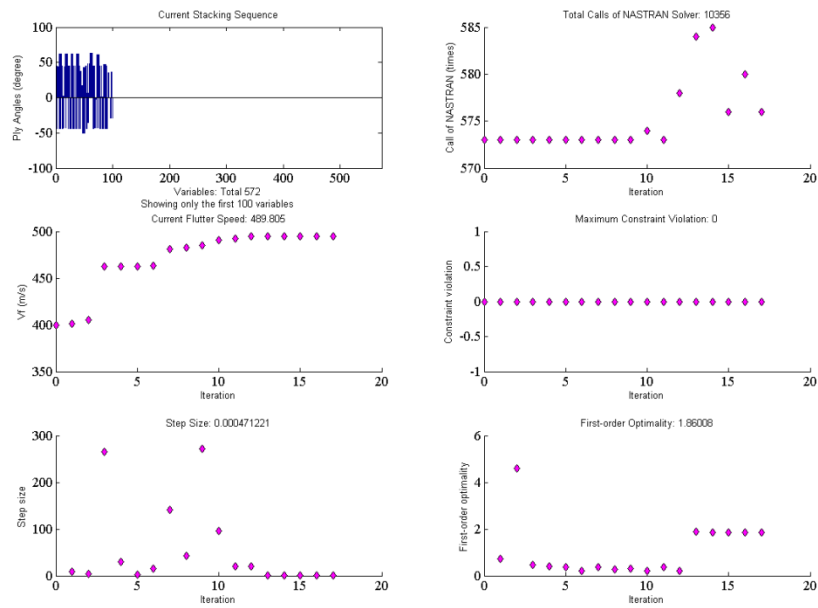
Figure 3-17 Convergence history for aeroelastic tailoring of baseline wing.

Table 3-13 Aeroelastic tailoring results of baseline wing.

Baseline wing model	Baseline wing	Optimized Wing
Flutter speed (m/s)	405	480
Flutter frequency (Hz)	8.57	8.80

In Figure 3-17, the current point indicates the current values of ply angles of the composite laminates. The function value is the flutter speed of the wing obtained from NASTRAN. The result shows that the flutter speed of the wing increased significantly with respect to the baseline wing. The baseline wing laminate layups and the optimized layups (trimmed into integer numbers) is provided in Appendix A. The flutter results of the optimization are given in Table 3-13, and the flutter V-g and V-f plots are shown in Figure 3-18 and Figure 3-19.
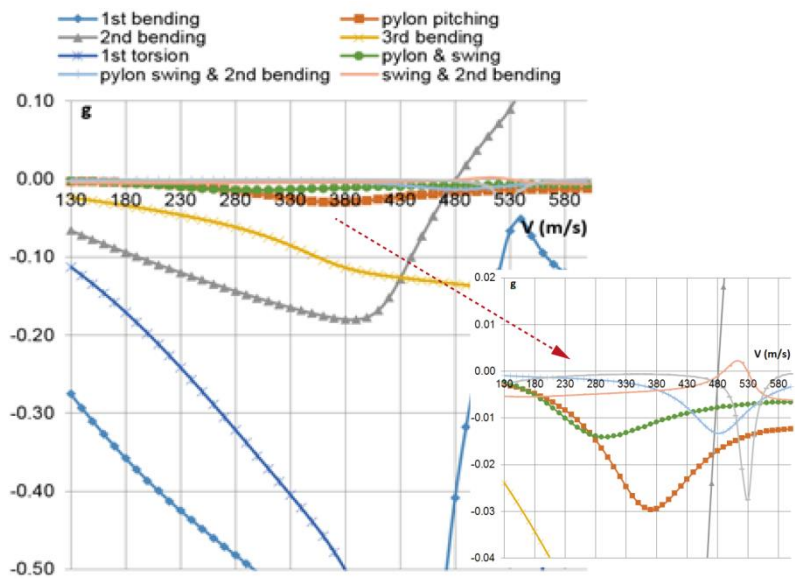
Figure 3-18 V-g plot of flutter for the optimized wing.
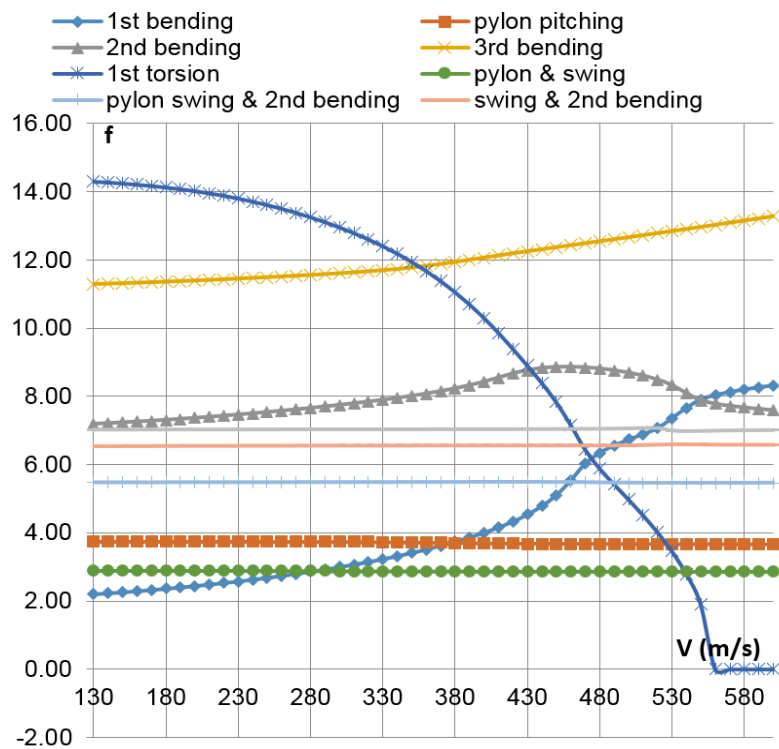
Figure 3-19 V-*f* plot of flutter for the optimized wing.

As shown in Table 3-13 and Figure 3-18 and Figure 3-19, the aeroelastic tailoring of the composite wing skins increases the flutter speed significantly.

The flutter speed of the wing increased from 405 m/s of the baseline wing to 480 m/s of the optimized wing, the flutter speed increment is 18.5%.
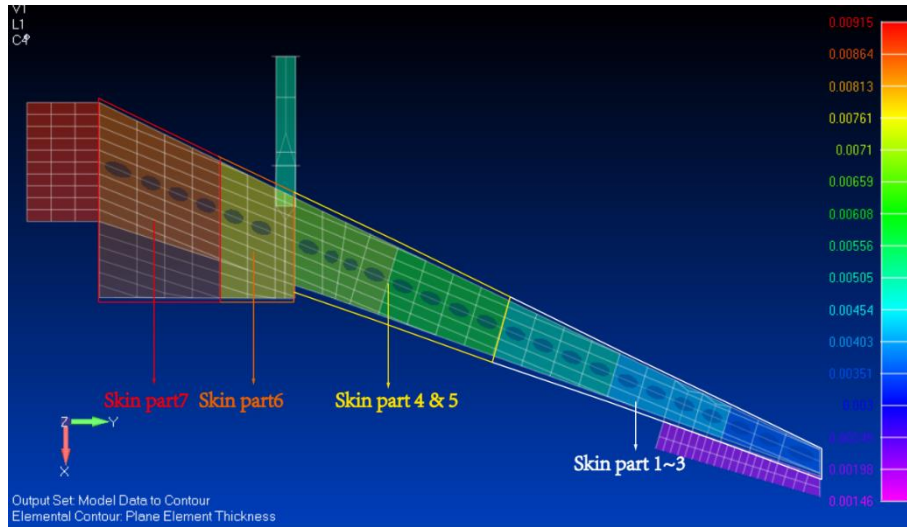
Figure 3-20 Regrouped baseline wing skin parts for independent optimization.

Table 3-14 Aeroelastic tailoring results of baseline wing for different wing parts.

Wing model	Baseline wing	Optimized for part 1~3	Optimized for part 4 and 5	Optimized for part 6	Optimized for part 7
Flutter speed (m/s)	405	314	468	411	399
Flutter frequency (Hz)	8.57	3.72	7.12	3.72	8.45

Following the above aeroelastic tailoring of whole wing, a subsequent optimization for independent wing parts is carried out. The 7 parts of the wing skin laminated are first regrouped into 4 independent parts as shown in Figure 3-20; aeroelastic tailoring is carried out for each regrouped part. The optimization settings are similar with the whole wing case, but this time we have taken only one or two of the wing skin parts for optimization, while keeping the rest skin parts unchanged. The results of this optimization are summarized in Table 3-14.

As shown in Table 3-14, for the laminate layup of the inboard and mid wing box 4~7, has relatively larger influence on the flutter behaviour of the wing, in particular, the parts 4~5 are the most effective and sensitive portions of the wing for aeroelastic tailoring, which leads to a significant increase of flutter speed from Vf=405 m/s of the baseline wing to the optimized design of Vf=468 m/s, almost reached the whole wing optimization result of 489m/s; while for the outer wing boxes (part 1~3), the aeroelastic tailoring has relatively small effect to improve the flutter speed of the wing.

3.3 Optimization of Non-circular Cross Section Fuselage for BWB Aircraft

Since 1940's, various conceptual design of aircraft including BWB configuration has been proposed and demonstrated. The main motivation and focus of study on the BWB aircraft has been driven by the advantage of aerodynamic efficiency relative to the conventional aircraft. However insufficient aircraft data exist to form empirical formula for BWB structure initial sizing like those employed in conventional aircraft design. Also inadequate study has been carried out to evaluate the structural weight of BWB aircraft especially in conceptual phase (Liebeck, 2004; Mukhopadhyay, 2005; Vos, Geuskens and Hoogreef, 2012). In this case study, the optimal design of BWB skin under internal pressure is considered. The non-circular cross section of BWB aircraft is used for optimization, which is the most concerned part of BWB structure that causes weight penalty. A theoretical model was developed to calculate the membrane stress and bending moment along the skin of a noncircular shape body under internal pressure.

3.3.1 Structure model of 2D non-circular cross section

3.3.1.1 Geometry of arbitrary 2D curve
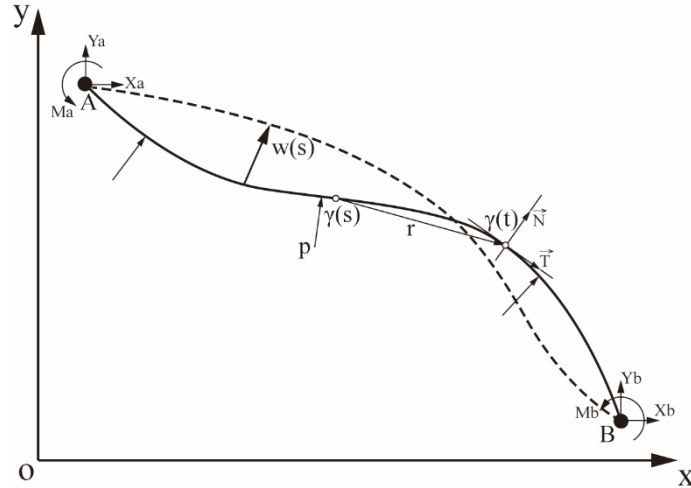
Figure 3-21 Deformation of arbitrary curve.

The arbitrary curve γ parameterized by arc length s is shown in Figure 3-21. The one-manifold is embedded in R^2 by its graph:

$$\gamma: s \rightarrow \big(x(s), y(s)\big) \tag{3-2}$$

The coordinates $x(s)$ and $y(s)$ are marked by the global Cartesian system. The unit tangent vector at a particular location s is obtained by direct differentiation:

$$\vec{T}(s) = \big(x'(s), y'(s)\big) \tag{3-3}$$

The unit outward normal vector defined by 90 degree anti-clockwise rotation of the tangent is easily obtained:

$$\vec{N}(s) = \big(-y'(s), x'(s)\big) \tag{3-4}$$

3.3.1.2 Kinematics of deformation

The fundamental differential equation for beams with arbitrary neutral curve axis is given by the moment-curvature equation,

$$M(s) = EI\varphi'(s) \tag{3-5}$$

where φ is the cross section rotation angle, M is cross section bending moment, EI is bending stiffness. The differential equation for the extension of the beam is given by,

$$FN(s) = EAh'(s) \tag{3-6}$$

where FN is membrane extensional force, h is beam extension function.

The unit tangent vector of the deformed beam $\vec{D}$, which we call it 'director', can be obtained from $\vec{T}$ by rotation about the angle φ,

$$\vec{D}(s) = R(s) \cdot \vec{T}(s) \tag{3-7}$$

where R is the rotation matrix. The deformed line element can be obtained from the director $\vec{D}$ and the extension h' as,

$$\vec{D}dl = (1 + h')R(s) \cdot \vec{T}(s)ds \tag{3-8}$$

which gives the differential displacement as,

$$d\vec{w} = \vec{D}dl - \vec{T}(s)ds = [(1 + h')R(s) - I] \cdot \vec{T}(s)ds \tag{3-9}$$

The displacements u and v in the respective directions can be obtained by integration,

$$
\begin{aligned}
(u, v) = \vec{w}(s) + \vec{w}_a &= \int_0^s [(1 + h')R - I] \cdot \vec{T}\, dt + (u_a, v_a) \\
&= \int_0^s \begin{bmatrix} (1 + h')\cos\varphi - 1 & -(1 + h')\sin\varphi \\ (1 + h')\sin\varphi & (1 + h')\cos\varphi - 1 \end{bmatrix} \cdot \begin{bmatrix} x' \\ y' \end{bmatrix} dt \\
&\quad + (u_a, v_a) \\
&= \int_0^s \begin{bmatrix} (1 + h')(\cos\varphi x' - \sin\varphi y') - x' \\ (1 + h')(\sin\varphi x' + \cos\varphi y') - y' \end{bmatrix} dt + (u_a, v_a)
\end{aligned}
\tag{3-10}
$$

where (u_a, v_a) is the boundary displacement vector at $s = 0$. Equation (3-10) gives,

$$u(s) = \int_0^s (1 + h')(\cos\varphi x' - \sin\varphi y') \, dt - x + u_a \qquad \text{(3-11)}$$

$$v(s) = \int_0^s (1 + h')(\sin\varphi x' + \cos\varphi y') \, dt - y + v_a \qquad \text{(3-12)}$$

For small angle φ and negligible extension $h' \approx 0$, the above displacements reduce to the linear equations,

$$u = \int_0^s -\varphi y' \, dt + u_a \qquad \text{(3-13)}$$

$$v = \int_0^s \varphi x' \, dt + v_a \qquad \text{(3-14)}$$

3.3.1.3 Curved beam with distributed pressure

Under distributed pressure, the total force produced by distributed pressure from location $s = 0 \sim s$ can be expressed by,

$$\vec{F}(s) = \int_0^s p(t)\vec{N}(t)dt = -\int_0^s py' \, dt\vec{i} + \int_0^s px' \, dt\vec{j} \qquad \text{(3-15)}$$

where we have assumed the origin of the global coordinate system is at the location $s = 0$. By forces equilibrium, we obtain the equations,

$$X(s) = \int_0^s py' \, dt - X_0(s) - X_a \qquad \text{(3-16)}$$

$$Y(s) = -\int_0^s px' \, dt - Y_0(s) - Y_a \qquad \text{(3-17)}$$

where X_a and Y_a are the boundary constraint forces at $s = 0$, X_0 and Y_0 corresponds to the forces due to initial deformation. The internal pressure

applied at location t exerts a bending moment on the beam element at location s (see Figure 3-21):

$$dM_p(t) = p(t)\vec{r} \times \vec{N}(t)dt = p(t)[\gamma(t) - \gamma(s)] \times \vec{N}(t)dt$$
$$= p(t)\{[x(t) - x(s)]x'(t) + [y(t) - y(s)]y'(t)\}dt$$

(3-18)

Therefore, the total moment produced by the internal pressure from $s = 0$ to s is obtained by integration:

$$M_p(s) = \int_0^s dM_p(t) = \int_0^s p\{[x - x(s)]x' + [y - y(s)]y'\}dt$$

(3-19)

Similarly, the constraint force at $s = 0$ exerts on the beam element at location s the moment:

$$M_c(s) = -\gamma(s) \times \vec{F}(0) = -xY_a + yX_a$$

(3-20)

The equilibrium of moment at location s gives the equation:

$$M_p(s) + M_c(s) + M_0(s) + M_a + M(s) = 0$$

(3-21)

where M_a is the boundary constraint moment at $s = 0$, M_0 is the moment due to initial deformation. Substitute (3-19) and (3-20) into (3-21), we obtain,

$$M(s) = -\int_0^s p\{[x - x(s)]x' + [y - y(s)]y'\}dt - M_0 - yX_a + xY_a - M_a$$

(3-22)

Letting,

$$a = \int_0^s py' \, dt - X_0$$

(3-23)

$$b = -\int_0^s px' \, dt - Y_0$$

(3-24)

$$c1 = -\int_0^s p\{[x - x(s)]x' + [y - y(s)]y'\}dt - M_0$$

(3-25)

$$c2 = -y \tag{3-26}$$

$$c3 = x \tag{3-27}$$

From (3-16), (3-17) and (3-22), we obtain,

$$\begin{cases} X = a - X_a \\ Y = b - Y_a \\ M = c1 + c2X_a + c3Y_a - M_a \end{cases} \tag{3-28}$$

Substitute M of (3-28) into (3-5), integrate both sides give the cross section rotation function,

$$\varphi = d1 + d2X_a + d3Y_a + d4M_a + \varphi_a \tag{3-29}$$

where φ_a is the boundary cross section rotation angle at $s = 0$. The coefficients di are given by,

$$di = \int_0^s \frac{1}{EI} ci \, dt, \qquad i = 1,2,3 \tag{3-30}$$

$$d4 = -\int_0^s \frac{1}{EI} dt \tag{3-31}$$

3.3.1.4 Linear system solution

Substitute (3-29) into the linear system (3-13) and (3-14), we obtain,

$$u = e1 + e2X_a + e3Y_a + e4M_a + e5\varphi_a + u_a \tag{3-32}$$

$$v = f1 + f2X_a + f3Y_a + f4M_a + f5\varphi_a + v_a \tag{3-33}$$

where the coefficients ei and fi are given by,

$$ei = -\int_0^s di y' \, dt, \qquad i = 1,2,3,4 \tag{3-34}$$

$$fi = \int_0^s di x' \, dt, \qquad i = 1,2,3,4 \tag{3-35}$$

$$e5 = -\int_0^s y'dt = -y, \qquad f5 = \int_0^s x'dt = x \qquad \textbf{(3-36)}$$

Equations (3-28), (3-29), (3-32) and (3-33) can be combined to give the linear system,

$$\begin{bmatrix} X \\ Y \\ M \\ \varphi \\ u \\ v \end{bmatrix} = \begin{bmatrix} -1 & 0 & 0 & 0 & 0 & 0 \\ 0 & -1 & 0 & 0 & 0 & 0 \\ c2 & c3 & -1 & 0 & 0 & 0 \\ d2 & d3 & d4 & 1 & 0 & 0 \\ e2 & e3 & e4 & e5 & 1 & 0 \\ f2 & f3 & f4 & f5 & 0 & 1 \end{bmatrix} \cdot \begin{bmatrix} X_a \\ Y_a \\ M_a \\ \varphi_a \\ u_a \\ v_a \end{bmatrix} + \begin{bmatrix} a \\ b \\ c1 \\ d1 \\ e1 \\ f1 \end{bmatrix} = [Q(s)] \cdot [Z_a] + [Z_p] \qquad \textbf{(3-37)}$$

where $[Z_a] = (X_a, Y_a, M_a, \varphi_a, u_a, v_a)$ is the column vector of boundary values, $[Z_p]$ is the independent vector. Equation (3-37) can be solved for a given set of boundary conditions. In particular, 6 parameters are required to uniquely determine the linear system. Let H_a be the set of i ($0 \leq i \leq 6$) unknown boundary conditions at end A ($s = 0$), $\mathrm{T_a}$ be the set of j ($j = 6 - i$) known boundary conditions at end A, and T_b be the set of i known boundary conditions at end B, respectively. Then (3-37) gives the equation,

$$[T_b - Z_p]_i = [Q1]_{i \times j} \cdot [T_a]_j + [Q2]_{i \times i} \cdot [H_a]_i \qquad \textbf{(3-38)}$$

where the vector $[T_b - Z_p]$ are seen to be chosen from the known i indices, $[Q1]$ and $[Q2]$ are the corresponding sub-matrices of $[Q]$, the matrix $[Q1]$ has dimension i by j, and $[Q2]$ is square matrix and has dimension i by i, therefore, the unknowns $[H_a]$ can be solved by,

$$[H_a] = [Q2^{-1}] \cdot [T_b - Z_p] - [Q2^{-1}] \cdot [Q1] \cdot [T_a] \qquad \textbf{(3-39)}$$

When the initial conditions $[H_a]$ are solved, the distribution of the forces, moments and deformation along the curved beam can be obtained directly from (3-37).

3.3.1.5 Nonlinear system solution

The membrane extensional force in (3-6) can be obtained by,

$$FN = (X, Y) \cdot \vec{T} \tag{3-40}$$

Substitute (3-28) into (3-40) we obtain,

$$FN = ax' + by' - X_a x' - Y_a y' \tag{3-41}$$

Substitute (3-6) into (3-11) and (3-12) we obtain,

$$u = \int_0^s \zeta(\vec{Z}_a)\, dt - x + u_a \tag{3-42}$$

$$v = \int_0^s \xi(\vec{Z}_a)\, dt - y + v_a \tag{3-43}$$

where the nonlinear functions ζ and ξ are given by,

$$\zeta = \left(1 + \frac{FN}{EA}\right)(\cos\varphi x' - \sin\varphi y') \tag{3-44}$$

$$\xi = \left(1 + \frac{FN}{EA}\right)(\sin\varphi x' + \cos\varphi y') \tag{3-45}$$

Combining (3-28), (3-29) and (3-42) and (3-43), we obtain the system of nonlinear equations,

$$[Z] = \Lambda(\vec{Z}_a) \tag{3-46}$$

where $[Z] = (X, Y, M, \varphi, u, v)$ is the column vector of beam functions, $\vec{Z}_a$ is the boundary value vector. To solve the nonlinear system (3-46), a Newton–Raphson method can be employed. We first give the linear approximation of the nonlinear system in a neighbourhood of a particular point $\vec{Z}_a = \vec{Z}_n$,

$$[Z] = \Lambda(\vec{Z}_n) + [QN]_{\vec{Z}_n} \cdot [\Delta Z_a] + O(|\Delta Z_a|^2) \tag{3-47}$$

where the matrix of partial derivatives (Jacobian) is given by,

$$[QN] = \begin{bmatrix} -1 & 0 & 0 & 0 & 0 & 0 \\ 0 & -1 & 0 & 0 & 0 & 0 \\ c2 & c3 & -1 & 0 & 0 & 0 \\ d2 & d3 & d4 & 1 & 0 & 0 \\ \zeta_1 & \zeta_2 & \zeta_3 & \zeta_4 & 1 & 0 \\ \xi_1 & \xi_2 & \xi_3 & \xi_4 & 0 & 1 \end{bmatrix}$$ (3-48)

where,

$$\zeta_i = \int_0^s \frac{\partial \zeta}{\partial Z_{ai}} dt, \qquad \xi_i = \int_0^s \frac{\partial \xi}{\partial Z_{ai}} dt, \qquad i = 1,2,3,4$$ (3-49)

By (3-41) and (3-44), (3-45), the partial derivatives are given as,

$$\zeta_1 = -\int_0^s \left\{ \frac{1}{EA + FN} x' \zeta + d2\xi \right\} dt$$ (3-50)

$$\zeta_2 = -\int_0^s \left\{ \frac{1}{EA + FN} y' \zeta + d3\xi \right\} dt$$ (3-51)

$$\zeta_3 = -\int_0^s d4\xi \, dt$$ (3-52)

$$\zeta_4 = -\int_0^s \xi \, dt$$ (3-53)

and,

$$\xi_1 = \int_0^s \left\{ -\frac{1}{EA + FN} x' \xi + d2\zeta \right\} dt$$ (3-54)

$$\xi_2 = \int_0^s \left\{ -\frac{1}{EA + FN} y' \xi + d3\zeta \right\} dt$$ (3-55)

$$\xi_3 = \int_0^s d4\zeta \, dt$$ (3-56)

$$\xi_4 = \int_0^s \zeta \, dt \qquad \textbf{(3-57)}$$

Having obtained the matrix $[QN]$, the system (3-47) can be solved for a step vector $[\Delta Z_a]$ by choosing the appropriate indices and sub-matrices according to the boundary conditions, as in the linear system solution,

$$[\Delta Z_a]_i = [QN2^{-1}]_{i \times i} \cdot \left[T_b - \Lambda(\vec{Z}_n)\right]_i \qquad \textbf{(3-58)}$$

where $[QN2]$ is the corresponding sub-matrix of $[QN]$. The Newton–Raphson scheme is applied by successively replacing the current solution $\vec{Z}_n$ by the better approximation,

$$\vec{Z}_{n+1} = \vec{Z}_n + \Delta\vec{Z}_a \qquad \textbf{(3-59)}$$

and update the associated functions ζ and ξ and the matrix $[QN]$, until a sufficiently accurate boundary value $\left|\vec{Z} - \Lambda(\vec{Z}_N)\right| < \delta$ is satisfied.

3.3.2 Structural model validation

An example case of elliptical curved beam is defined by the function,

$$\frac{x^2}{300^2} + \frac{y^2}{200^2} = 1 \qquad \textbf{(3-60)}$$

The boundary value problem for this given curve is solved based on the method we have developed with material properties, loads and cross section dimension of the beam defined in Table 3-15. The solutions obtained and comparisons with FEM package (NASTRAN) results for different boundary conditions (simply supported, fixed) are given in Table 3-16 and Table 3-17.

70
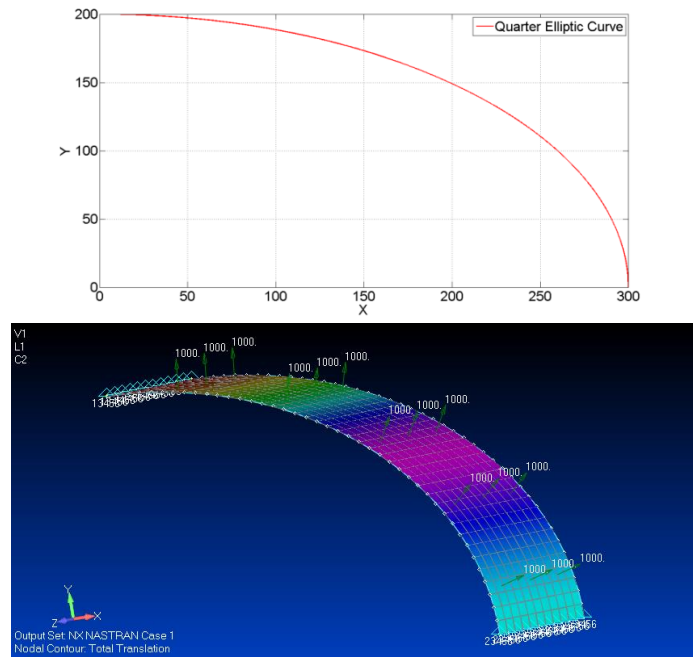
Figure 3-22 Quarter elliptic shape curve.

Table 3-15 Material properties, loads and cross section dimension of the curved beam.

Properties	Values
Elastic Modulus (E)	7e10 Pa
Cross Section Width (W)	100 cm
Cross Section Height (Thickness t)	0.6 cm
Applied Internal Pressure	1e3 Pa

As shown in the above tables, the developed model for both simple supported and fixed boundary condition achieved very good agreement with the commercial FE solver NASTRAN.

Table 3-16 Simply supported on both ends-Results and comparisons with FEM package (NASTRAN).

Boundary Condition Input	Result Quantity	Results Comparison
	X Displacement (m)	
$T_a = \begin{bmatrix} M_a \\ u_a \\ v_a \end{bmatrix}$ $T_b = \begin{bmatrix} M_b \\ u_b \\ v_b \end{bmatrix}$ $T_a = T_b = \mathbf{0}$	Y Displacement (m)	
	Cross Section Rotation Angle	
	Bending Moment Distribution (Nm)	

Table 3-17 Fixed on both ends-Results and comparisons with FEM package (NASTRAN).

Boundary Condition Input	Result Quantity	Results Comparison
	X Displacement (m)	
	Y Displacement (m)	
$T_a = \begin{bmatrix} \varphi_a \\ u_a \\ v_a \end{bmatrix}$ $T_b = \begin{bmatrix} \varphi_b \\ u_b \\ v_b \end{bmatrix}$ $T_a = T_b = \mathbf{0}$	Cross Section Rotation Angle	
	Bending Moment Distribution (Nm)	

3.3.3 Optimization of BWB fuselage under internal pressure

Based on the above method, an optimization study is carried out for a typical BWB fuselage cross section. A 2D section of the BWB aircraft fuselage nose position is chosen for this optimization, as shown in Figure 3-23. The resulting 2D non-circular cross section has width approximately 3.5m and height 3m (half) as shown in Figure 3-24.
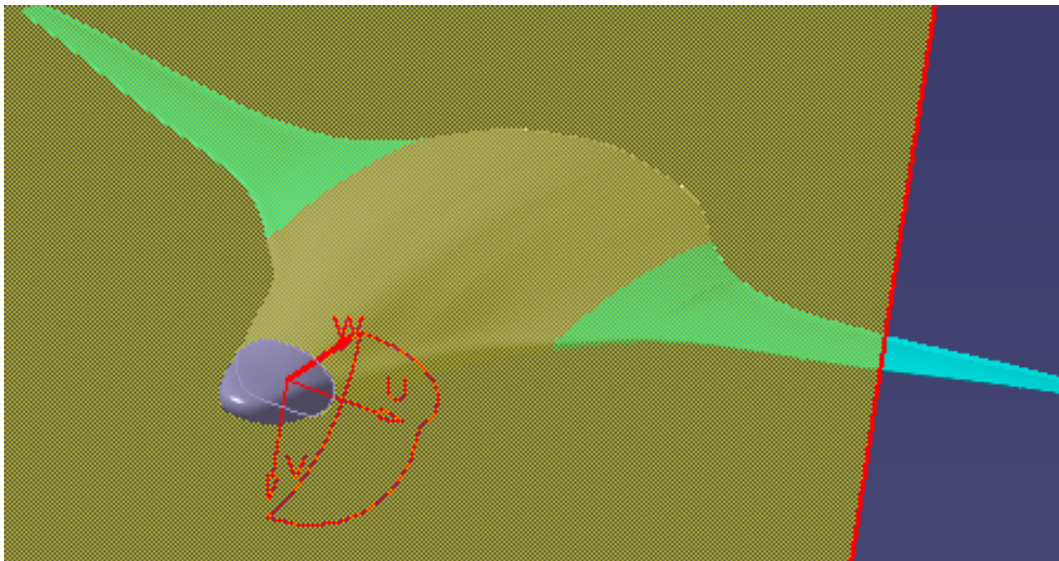
Figure 3-23 BWB Fuselage sectional curve cut position.
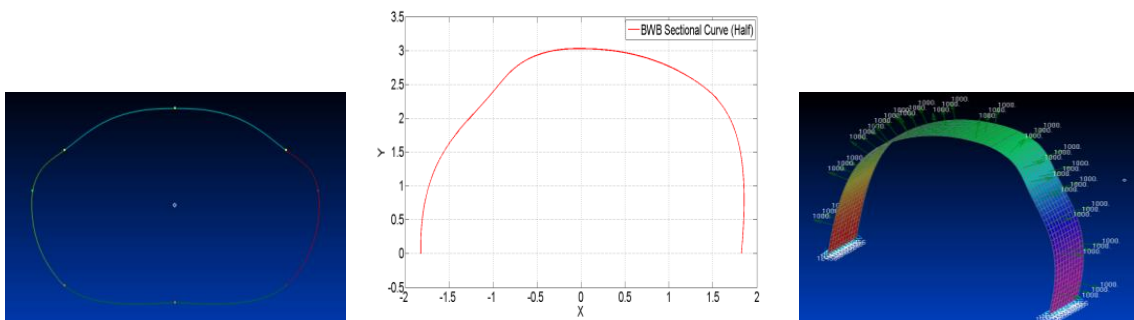
Figure 3-24 BWB Fuselage sectional curve. In the 2D coordinate system, x corresponds to v axis and y corresponds to u axis in figure 3-23.

The cross section of the BWB body as shown in Figure 3-24 has irregular shape, with one axis of symmetry. The right half of the cross section is therefore

chosen for this study. The material properties, loads and cross section dimension of the beam are defined in Table 3-18. In this study, the initial skin thickness of the cross section is set as t=0.023m.

Table 3-18 Material properties, loads and cross section dimension of the BWB cross section.

Properties	Values
Elastic Modulus (E)	7e10 Pa
Cross Section Width (w)	1 m
Skin Thickness (t)	0.023 m
Applied Internal Pressure	4e4 m

3.3.3.1 Stress analysis of BWB cross section

Based on the above model parameters and definitions, the BWB body cross section under internal pressure is used for stress analysis. For the half cross section, the boundary condition of this analysis is set as fixed on both ends. The bending stress and tensile stress along the 2D cabin curve is recovered by the equations:

$$\sigma_M = \frac{M \cdot t}{2I} \tag{3-61}$$

$$\sigma_N = \frac{FN}{w \cdot t} \tag{3-62}$$

where *M* is the bending moment and *FN* is the tensile force on the beam cross section along the curve. The resulting deformed shape, displacement and stress distribution of the BWB cross section under internal pressure is shown in Figure 3-25, Figure 3-26 and Figure 3-27. Under the applied pressure of 4e4 Pa, the maximum displacement of the structure is 0.2m, the maximum total stress is 350Mpa, which is primarily contributed by the bending stress, as shown in Figure 3-27.
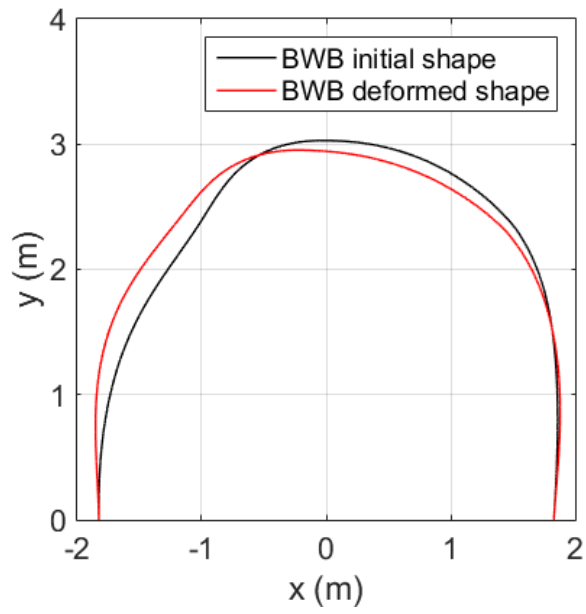
Figure 3-25 BWB fuselage cross section initial and deformed shape.
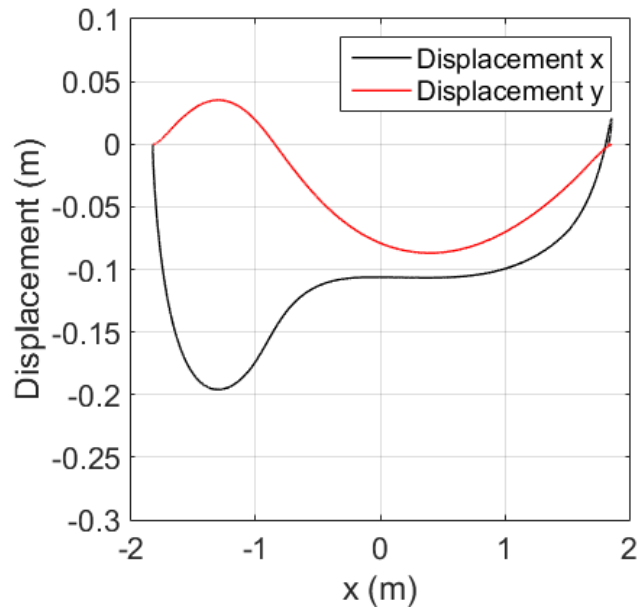
Figure 3-26 BWB Fuselage cross section displacement.
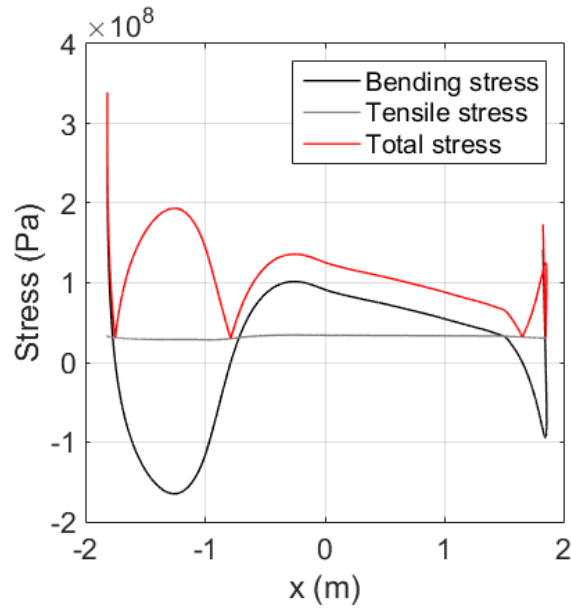
Figure 3-27 BWB Fuselage cross section stress distribution.

3.3.3.2 Optimization of BWB cross section

Based on the above definitions, the optimization is carried out for the skin thickness of the cross section. For this optimization, the fmincon function in MATLAB is used. The cross section skin thickness is divided into 10 parts, as shown in Figure 3-28. The setting of this optimizer is similar to that in section 3.2. The optimization is aimed at minimizing the structural weight subject to maximum stress, which is summarized in Table 3-19.
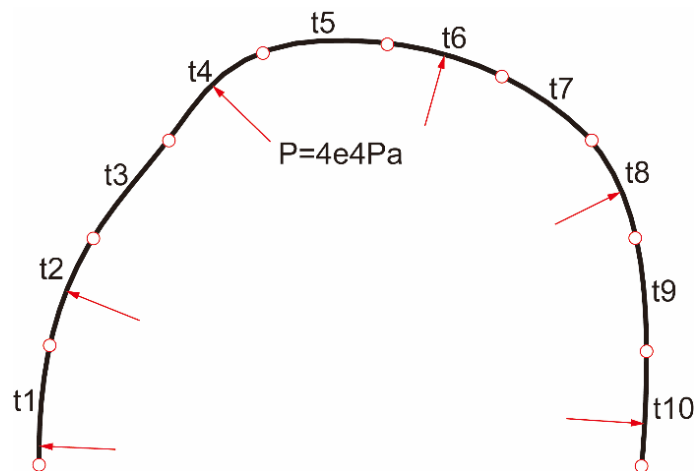
Figure 3-28 BWB Fuselage cross section skin thicknesses.

Table 3-19 Summary of optimization settings for BWB cross section.

Properties	Values
Optimization objective	Minimize structural weight
Optimization variables	Skin thickness (t)
Optimization constraint1	$0.01 \leq t \leq 0.025$ (m)
Optimization constraint2	Maximum stress $\leq$ 350Mpa

Based on the developed method, the optimization is carried out. The comparison of initial and optimized design is shown in Table 3-20. The optimized skin thickness distribution is shown in Table 3-21. The deformed shape, displacement and stress distribution along the 2D cabin curve of optimized design is shown in Figure 3-29, Figure 3-30 and Figure 3-31.

Table 3-20 Comparison of initial and optimized design of BWB fuselage cross section.

Structural parameters	Baseline fuselage	Optimized fuselage
Total weight, kg	486	401 (17% structural weight saving)
Maximum stress, Mpa	350	347

Table 3-21 BWB cross section optimized skin thickness distribution, m.

part1	part2	part3	part4	part5
2.50e-02	1.89e-02	2.38e-02	1.72e-02	1.68e-02
part6	part7	part8	part9	part10
1.63e-02	1.61e-02	1.61e-02	1.94e-02	1.72e-02
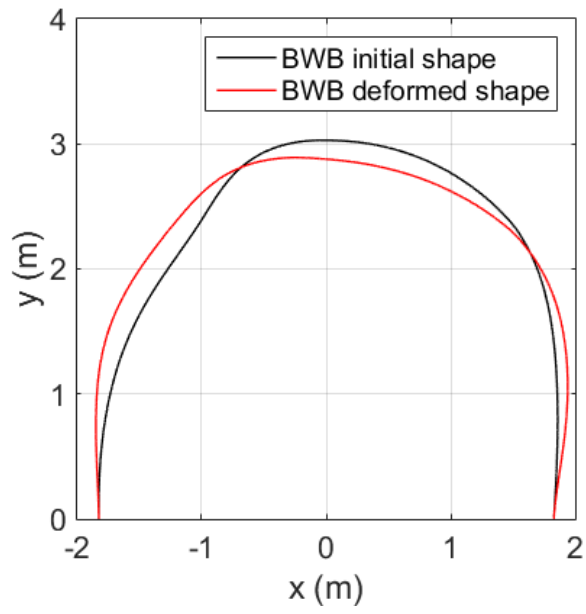
Figure 3-29 Optimized BWB fuselage cross section initial and deformed shape.
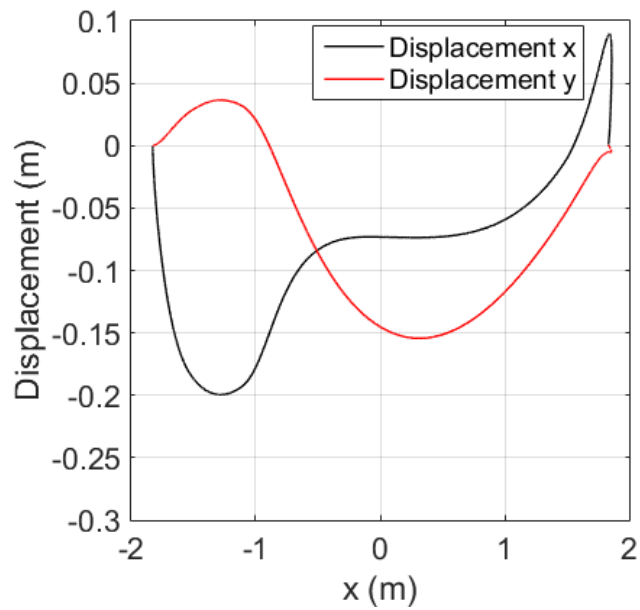
Figure 3-30 Optimized BWB fuselage cross section displacement.
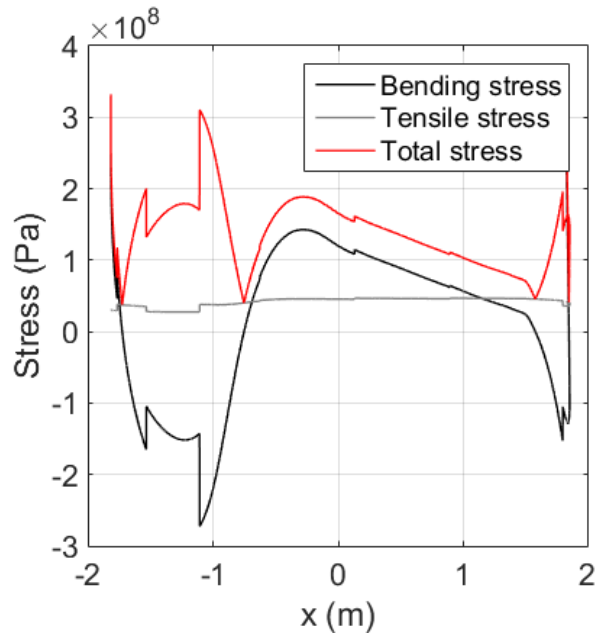
Figure 3-31 Optimized BWB fuselage cross section stress distribution.

Compared with the initial design, the optimized BWB cross section under the same applied internal pressure has achieved weight reduction of 17%. Despite the small variations in the displacement distribution, the maximum displacement of the optimized design is the same as the initial design of 0.2m. The stress distribution of the optimized design show significant variations along the 2D cabin curve, due to the discontinuous thicknesses of the optimized design.

3.4 Summary

In this chapter, the design, analysis and optimization techniques for conventional aircraft structure and aeroelasticity are presented. These classical techniques for conventional aircraft design are primarily based on the well-developed FE package such as NASTRAN or simplified analytic methods, which have been presented respectively in this chapter.

The aeroelasticity of conventional fixed wing is investigated using the commercial FE package NASTRAN. To facilitate the optimization of conventional fixed wing, a MATLAB-NASTRAN interfaced optimization platform is created. The optimization results show that significant weight reduction (13%)

can be obtained which satisfies the static stress, buckling and aeroelastic constraints if minimal weight is set as the objective of optimization. On the other hand, aeroelastic tailoring results for composite laminate layups of the wing show that the flutter speed can be increased by 18.5%. Furthermore, aeroelastic tailoring by different wing parts show that the most sensitive part of the wing for aeroelastic optimization is near the engine location, which contributes to the majority of flutter speed increase for optimization.

In order to facilitate the structural design of non-circular cross section fuselage of Blended-Wing-Body (BWB) aircraft, an analytical model of a 2D non-circular cross section is developed, which provides efficient design and optimization of the structure without referring to FE models. A case study based on a typical BWB fuselage using the developed model shows that by optimizing the fuselage structure, significant weight saving (17%) can be obtained.

These design, analysis and optimization techniques for conventional aircraft have been heavily used in industry. In these application scenarios, the design objectives for aerospace structures have been primarily focused on preventing or supressing the adverse behaviour of aircraft structure or aeroelasticity, e.g. strength, buckling, control effectiveness and flutter, which could result in undesirable effects or catastrophic failure of aircraft structures. However, the recent development in UAVs and MAVs has imposed new challenges for aeroelastic investigations. Flying animals in nature manipulate wing aeroelasticity. Their active or passive wing deformation and morphological shape changing improve their flight efficiency and increase their flight capacity. These fascinating features of animal flight have inspired aeroelastic research to explore aeroelastic beneficial effects of extremely light weight and flexible structures for UAVs and MAVs.

In the following chapters, the aerodynamic and aeroelasticity of bio-inspired flapping wing MAV is investigated. Different from the classical methods for large aircraft, the design and analysis methods for flyers at such micro scale has not been well studied. In particular, one biggest challenge for flight at such small scale (Re range between 100 and 10000) is the aerodynamics in the viscous

and separating flow. Furthermore, the extremely light weight and flexible wing structure result in large and nonlinear bending and twisting deformation of the wing. These challenges and features of flapping wing MAVs will be addressed by numerical modelling as well as experimental investigations and presented in the following chapters.

4 AERODYNAMIC MODELLING OF FLAPPING WINGS AT LOW REYNOLDS NUMBER

The aerodynamics of flapping wing flight at low *Re* has quite different features to that of the steady-state aerodynamics for large aircraft. In the low *Re* regime, the weak inertia of fluid flow leads to flow separation at small incident angle. In particular, the unsteady reciprocal flapping motion of the wings leads to significant vortices shedding for flapping wing flyers. In order to model the unsteady aerodynamic force of flapping wing flight, the CFD method with moving grid technique can be employed (Liu et al., 1998; Mao and Hamdani, 2001; Sun, Tang and Tang, 2002). However, the CFD method for 3D flapping wing model often requires large computational time. In this chapter, a quasi-steady aerodynamic model is developed for the low *Re* flapping wing aerodynamics. This model makes use of empirical data for correction of the unsteady effects such as stable LEV, rotational circulation and added mass effects. This model is validated against various wing kinematic cases with both 2D CFD and 3D CFD results.

4.1 Coordinate and Kinematics Definition

The coordinate system to define the FWR wing motion is shown in Figure 4-1. The kinematics of the wing is defined by three elementary motions: rotation, flapping and pitching. The wing rotates about the vertical y axis, and the rotation speed is fixed constant and indicated by $\dot{\psi}$. The dimensionless wing rotation speed is defined as:

$$\eta = \frac{\dot{\psi}}{2\Phi f} \qquad \textbf{(4-1)}$$

where Φ is the flapping angle amplitude and f is the flapping frequency.

The wing flaps vertically with the flapping angular velocity $\dot{\phi}$ described by the Simple Harmonic Function (SHF):

$$\dot{\phi} = -\pi f \Phi sin(2\pi\tau) \qquad \textbf{(4-2)}$$

where $\tau=ft$ is the dimensionless time ranging from 0~1 in a flapping period.

The wing pitches at the same frequency f, with a phase shift of $\pi/2$. The pitch motion of the wing is confined to stroke reversals. At the mid-upstroke and mid-downstroke, the wing has AoA denoted by α_u and α_d, respectively. In the reversal phase at the end of each stroke, the pitch angular velocity of the wing $\dot{\alpha}$ is described by the following equation:

$$\dot{\alpha} = \frac{2f(\alpha_u - \alpha_d)}{\Delta\tau_r}\left\{(-1)^{[2\tau+0.5]} - cos\left(\frac{4\pi\tau}{\Delta\tau_r} - \lfloor 2\tau - 0.5\rfloor\pi\right)\right\} \qquad \textbf{(4-3)}$$

where $\Delta\tau_r=0$~1 indicates the dimensionless wing pitch time with respect to the flapping period, and the bracket notation $\lfloor\cdot\rfloor$ indicates the floor function giving the greatest bounding integer. In the present study, the wing pitch time takes half of the flapping period, corresponding to $\Delta\tau_r=0.5$.
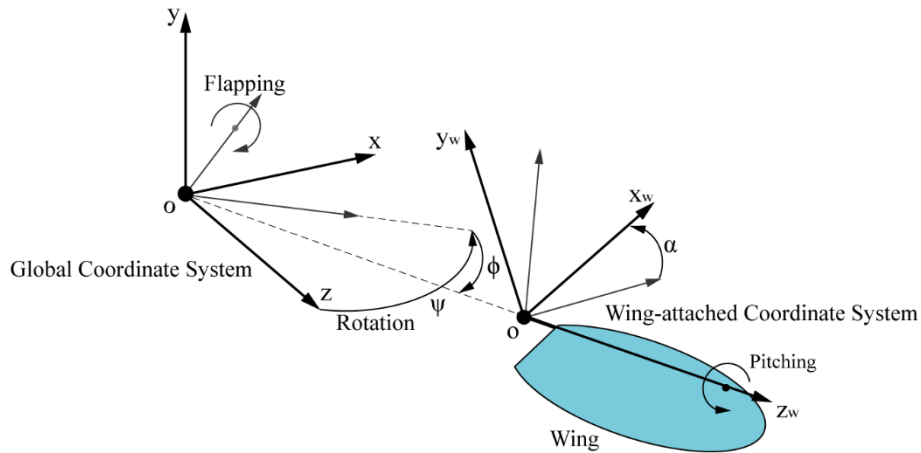
Figure 4-1 Coordinate systems definition for the FWR wing.

4.2 Quasi-steady Aerodynamic Model

4.2.1 Quasi-steady equations and coefficients

The wing planform is in ellipse as illustrated in Figure 4-2. The pitching axis of the wing (z_w) is located near the leading edge; c is the local chord length at a 2D wing strip dr; h is the vertical distance between the mid-chord axis and the pitching axis of the wing. The pitching axis of the wing is taken to be located at

0.25 chord (Ellington, 1984c; Sane and Dickinson, 2002), corresponding to h=0.25c. The dimensionless radius of the first, second and third area moments $\hat{r}_1$, $\hat{r}_2$ and $\hat{r}_3$ of the wing are defined by:

$$\hat{r}_k = \sqrt[k]{\frac{AR \int_0^R cr^k dr}{R^{k+2}}}, \qquad k = 1,2,3 \tag{4-4}$$

where R is the wing semi-span, AR=3.6 is the aspect ratio. These are the shape parameters for the wing geometry. In order to keep the morphological similarity with insect wings, the parameters $\hat{r}_1$, $\hat{r}_2$ and $\hat{r}_3$ are constrained by the numbers 0.45~0.55, 0.5~0.6 and 0.55~0.65, respectively (Ellington, 1984c). In addition, the Rossby number Ro is defined by (Lentink and Dickinson, 2009):

$$Ro = \frac{R_2}{\bar{c}} \tag{4-5}$$

where $R_2 = \hat{r}_2 R$ is the radius of the second area moment, and $\bar{c} = \frac{R}{AR}$ is the mean chord length. For hovering flight, Ro is equivalent to AR and is given by the value Ro=2.1 in the current study. The geometric parameters of the FWR wing are listed below:

$$AR = 3.6, \ Ro = 2.1, \ \hat{r}_1 = 0.55, \ \hat{r}_2 = 0.59, \ \hat{r}_3 = 0.63 \tag{4-6}$$
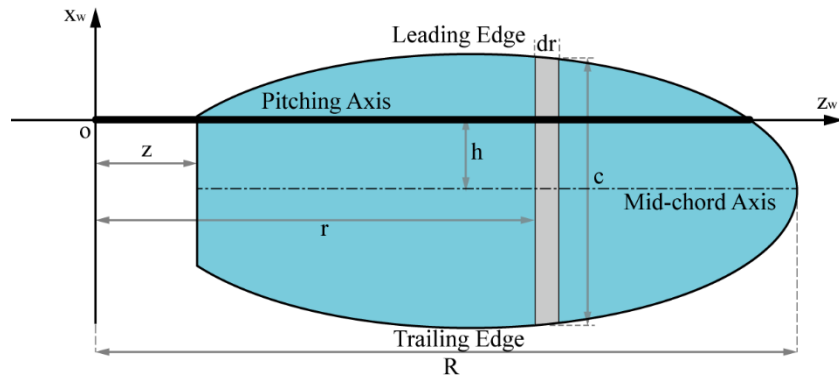
Figure 4-2 Geometry and parametric definitions of the wing.

The aerodynamic force of the wing is solved by employing a quasi-steady aerodynamic model. Some basic definitions for descriptions of the rigid body

rotation of the wing are provided in (Li et al., 2016). On a 2D wing strip, the aerodynamic forces and pitch moment in the local wing-attached frame (x_w, y_w and z_w) are obtained by the equations:

$$dF_x = \left\{ \frac{1}{2} \rho U^2 C_H c + \left[\lambda_y u_y \omega_z + \lambda_{y\omega} \omega_z^2 \right] \right\} dr \tag{4-7}$$

$$dF_y = \left\{ \frac{1}{2} \rho U^2 C_V c + C_{ROT} \rho U \omega_z c^2 - \left[\lambda_y \dot{u}_y + \lambda_{y\omega} \dot{\omega}_z \right] \right\} dr \tag{4-8}$$

$$d\tau_z = \left\{ -\frac{1}{2} \rho U^2 C_V \hat{x}_{CP} c^2 - \frac{1}{2} \rho \omega_z |\omega_z| C_{RD} \hat{x}_{RD} c^4 \right. $$
$$ \left. + \left[\lambda_y u_x u_y + \lambda_{y\omega} (\dot{u}_y + u_x \omega_z) + \lambda_\omega \dot{\omega}_z \right] \right\} dr \tag{4-9}$$

where ρ is the air density; U is the translational velocity; ω_z and $\dot{\omega}_z$ are the wing pitch rate and pitch acceleration; u_x, u_y and $\dot{u}_y$ are the translational velocity components in the x and y axes and the acceleration; λ_y and $\lambda_{y\omega}$ are the added mass force coefficients, which are given by $\lambda_y = \pi/4 \rho c^2$ and $\lambda_{y\omega} = \pi/4 \rho h c^2$; λ_ω is added mass moment coefficient, which is given as: $\lambda_\omega = \pi/4 \rho h^2 c^2 + \pi/128 \rho c^4$ (Sedov, 1965).

The quasi-steady aerodynamic coefficients C_H, C_V and C_{ROT} are empirical coefficients for the translational force and rotational force (Sane and Dickinson, 2001, 2002); C_{RD} is the rotational damping moment coefficient; $\hat{x}_{CP}$ is the dimensionless Centre of Pressure (CP) of the translational force; $\hat{x}_{RD}$ is the dimensionless location of the rotational damping force; The relation of the empirical coefficients with the effective AoA α_e are provided in (Li et al., 2016).

The 2D aerodynamic forces and pitch moment for each wing strip are integrated along the wing-span to obtain the 3D forces and moments. The vertical lift force and rotational moment of the wing can then be obtained by projecting the 3D force and moment vectors onto the global y axis of the coordinate, as shown in Figure 4-1. The lift and rotational moment coefficients are defined as:

$$C_L = \frac{l}{0.5 \rho U_2^2 S} \tag{4-10}$$

$$C_M = \frac{m}{0.5\rho U_2^2 S\bar{c}} \qquad\qquad \textbf{(4-11)}$$

where l is the vertical lift force and m is the rotational moment, i.e. moment along the global y axis, $\bar{c}$ is the mean chord length, S is the wing area. The reference velocity U_2 is defined by:

$$U_2 = 2\Phi f\hat{r}_2 \qquad\qquad \textbf{(4-12)}$$

where $\hat{r}_2$ is the radius of the second moment of wing area. The mean coefficients $\bar{C}_L$ and $\bar{C}_M$ are defined similarly with the mean lift force ($\bar{l} = \frac{\int_0^T l\,dt}{T}$) and rotational moment ($\bar{m} = \frac{\int_0^T m\,dt}{T}$) put into the equations instead of the instantaneous values.

The dimensionless parameters that govern the flow and the shedding of vortices are the Strouhal number and the reduced frequency. The Strouhal number St is defined by:

$$St = \frac{fA}{U} \qquad\qquad \textbf{(4-13)}$$

where the characteristic width A is taken to be the stroke amplitude at the wingtip, and the forward speed U is taken to be the rotation speed of the wing at the wingtip (Taylor, Nudds and Thomas, 2003). For a 2D airfoil, the reduced frequency k_c is defined by:

$$k_c = \frac{2\pi f c}{U_c} \qquad\qquad \textbf{(4-14)}$$

where U_c is the rotation speed at the specific chord.

4.2.2 Aerodynamic power and efficiency measures

Based on the above definitions, the mean aerodynamic power over a flapping cycle T can be obtained by summing the aerodynamic power of each independent axis of rotation:

$$\bar{P} = \sum_{i=x,y,z} \bar{P}_i \tag{4-15}$$

where $\bar{P}_i = -\frac{\int_0^T \omega_i \tau_i dt}{T}$ is the mean aerodynamic power of the ith axis. The mean aerodynamic power coefficient can be defined as:

$$\bar{C}_P = \frac{\bar{P}}{0.5\rho U_2^3 S} \tag{4-16}$$

The mean aerodynamic power $\bar{P}$ is the total power required for the wing to overcome the fluid forces. Therefore, when measuring the efficiency of lift production, $\bar{C}_P$ can be used directly to define the dimensionless power factor *Pf* (Lentink and Dickinson, 2009; Wang, 2008), which measures the power efficiency of flying animals and vehicles for sustaining a specific weight:

$$P_f = \frac{\bar{C}_l^{1.5}}{\bar{C}_P} \tag{4-17}$$

However, when measuring the propulsive efficiency, the mean aerodynamic power of each independent axis $\bar{P}_i$ needs to be treated separately. The propulsive efficiency of the wing ηp is defined by the ratio of aerodynamic power output (for propulsion) to the power input:

$$\eta_p = \frac{|\bar{P}_y|}{\bar{P} - \bar{P}_y} \tag{4-18}$$

When the flapping wing is producing positive propelling moment, this definition agrees with the usual definition of propulsive efficiency for oscillating foils in the free stream (Triantafyllou, Triantafyllou and Grosenbaugh, 1993; Triantafyllou, Triantafyllou and Gopalkrishnan, 1991).

4.3 Aerodynamic Model Validation

4.3.1 Comparison with 2D CFD results

In order to validate the Quasi-Steady (QS) aerodynamic model, firstly, a 2D CFD analysis is carried out using the commercial CFD solver ANSYS Fluent,

which solves the 2D unsteady, incompressible Navier-Stokes equations based on a finite volume method. The accuracy of this solver has been extensively validated against several experimental and numerical studies in flapping wing aerodynamics (Bos et al., 2008). The 2D airfoil is chosen as flat plate of 2% thickness. The QS model and 2D CFD model is then further compared with the high fidelity 3D CFD results from previous study.

A particular kinematic case from Wu et al. (Jianghao, Chao and Yanlai, 2017) is chosen with the kinematic parameters of the wing specified by: ф=70º, α_u=60º, α_d=-20º and the rotation speed η=1.10. In this case, the wing model is of rectangular shape and aspect ratio 5.8 (*AR=R*/c). The wingspan *R* and the flapping frequency *f* are given by *R*=98mm and *f*=10Hz, corresponding to *Re*=1600 ($Re = \frac{U_2\bar{c}}{\nu}$, where U_2 is the mean flapping velocity at the radius of the second moment of wing area r_2, ν is the kinematic viscosity). For the 2D CFD analysis, a series of wing chords located along the wing-span (ranging between 0.2~0.7 wing-spans) is taken for investigation. To compare the 2D model with 3D results, the thrust coefficient of the 2D results ($C_T = \frac{T}{0.5\rho\bar{U}^2c}$, where *T* is the thrust force and $\bar{U}$ is the local mean flapping velocity) is converted to the 3D rotational moment coefficient Cm using a scale factor of ARI_3/I_2 obtained from a standard blade element analysis, I_k is the *k*th dimensionless moment of wing area defined by the equation:

$$I_k = \frac{\int r^k dS}{R^k S} \tag{4-19}$$

The time courses of the forces and rotational moments by different models are shown in Figure 4-3 (a), the flow field for the 2D wing chord is shown in Figure 4-3 (b), where red and black colour indicates anti-clockwise and clockwise rotating vortices respectively. All the cases have the same *St*=0.45; the 2D CFD result presented here is taken at 0.35 wing-span, with reduced frequency *kc*=1.15. The full spectrum of 2D results at different span-wise locations ranging between 0.2*R*~0.7*R* is shown in Figure 4-4.
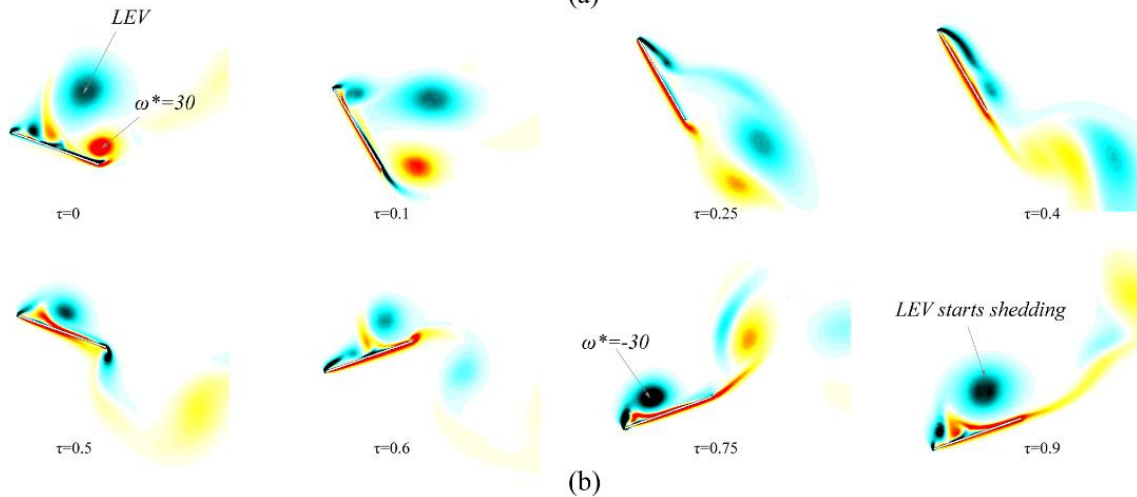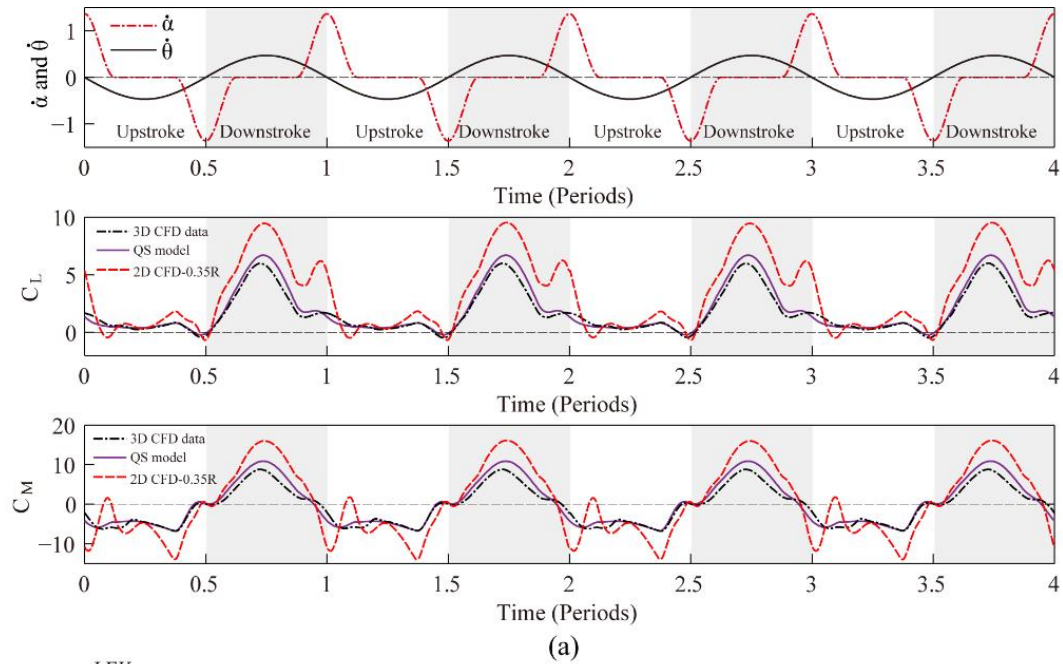
Figure 4-3 (a) Comparison of C_L and C_M by QS, 2D and 3D CFD model results; (b) Contour of flow vorticity for 0.35R (k_c=1.15) 2D wing.

From the results in Figure 4-3 (a), it is clear that the time courses of the 3D QS forces and moments agree very well with the 3D CFD results; while for the given wing chord at 0.35 wing-span, the 2D CFD results appear larger due to the well-known downwash of the wingtip vortex for a 3D wing. However, the variation of the 2D transient forces agrees qualitatively with the 3D transient forces.

In Figure 4-3 (b), the flow over the 2D wing chord shows a dynamic formation and shedding of vortices that closely resembles the dynamic stall of conventional airfoil. In the downstroke, a strong LEV first forms on the upper surface until a reverse flow emerges from the trailing edge and the LEV starts to shed from the surface. The shedding of the LEV is near the end of the downstroke, corresponding to a decrease in lift coefficient.

The particular choice of wing chord at 0.35R to represent the flow field follows from the observation that the shedding of LEV is at the end of downstroke. In previous studies on 2D flapping wing, the frequency of LEV shedding was shown to play significant role in determining the transient forces. Lewin and Haj-Hariri (Lewin and Haj-Hariri, 2003) and Wang (Wang, 2000) used numerical simulation to analyse an airfoil in 2D flow undergoing heaving oscillating. They show that the dimensionless reduced frequency k_c and the Strouhal number St serve to govern the time scale associated with the growth and shedding of the vortices on the wing. The number k_c is the primary factor governing the LEV shedding and St the secondary factor related to the growth of LEV. For a smaller value of k_c, the LEV tends to separate and advect along the freestream, leading to an early separation of the LEV; while for larger k_c, the LEV tends to separate later and stays longer on the wing in each flapping stroke. A similar flow phenomenon is observed in the present study. The LEV on the outer wing chords (with smaller k_c) tends to separate early while it stays longer on the inner wing chords with larger k_c, as shown in Figure 4-4 (b).
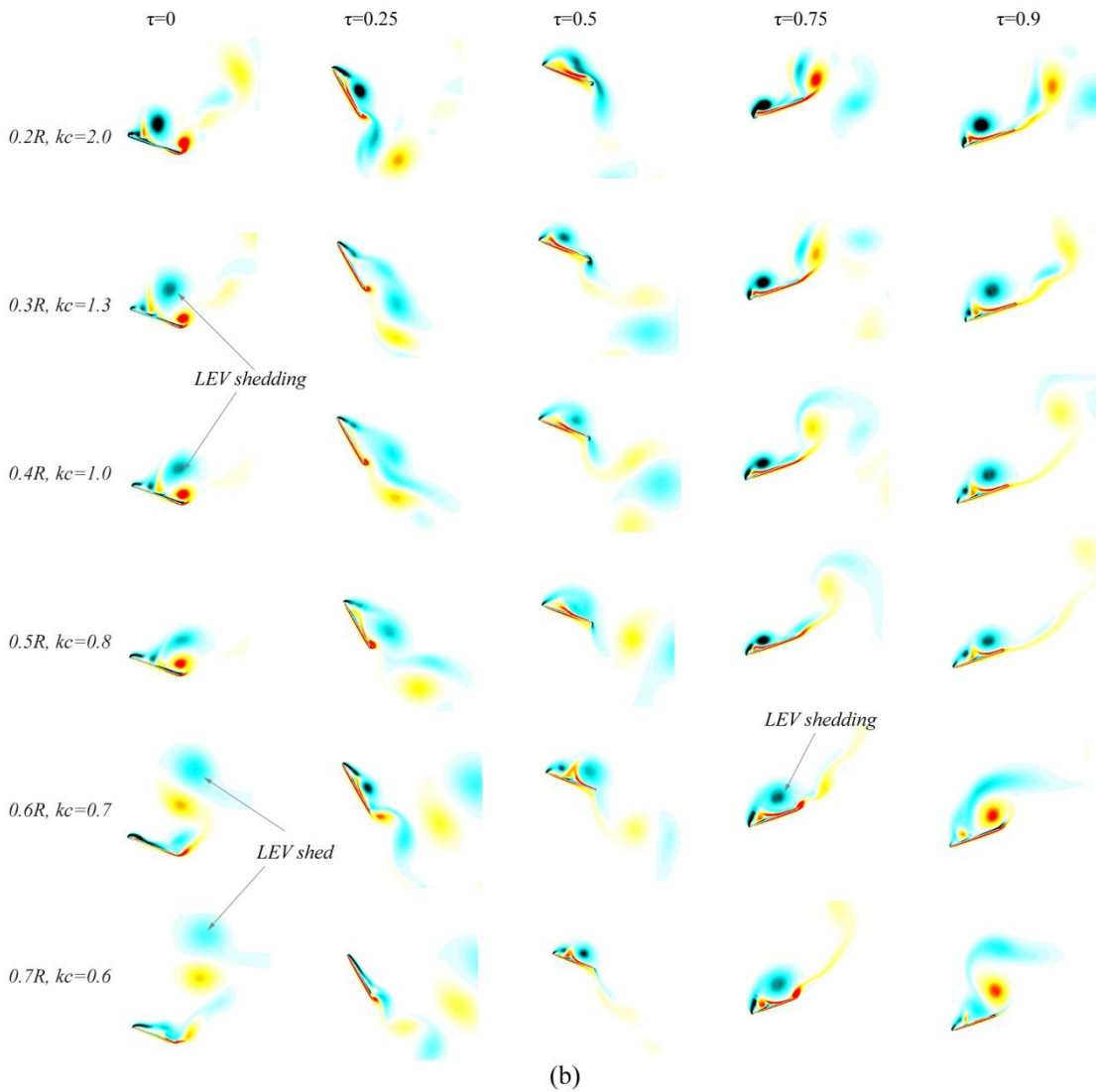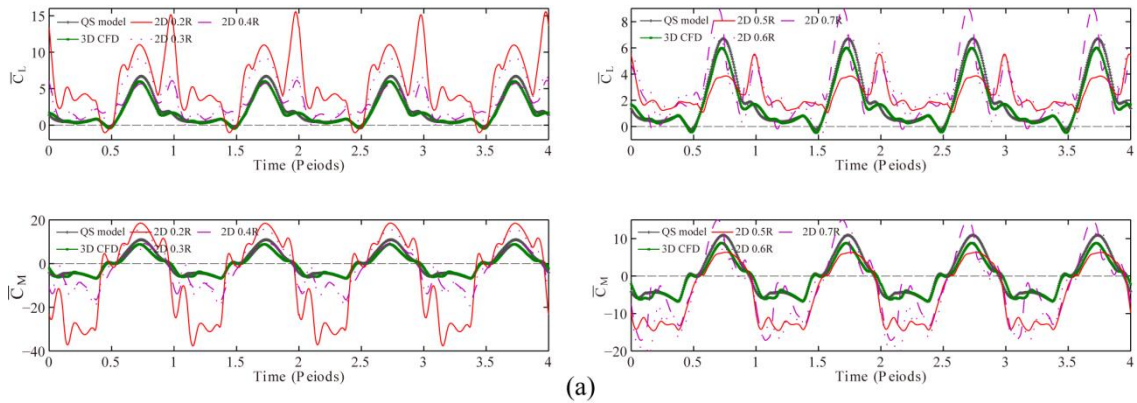
Figure 4-4 (a) Time courses of C_L and C_M by QS, 3D CFD and 2D CFD model at different chord-wise locations; (b) Contour of flow vorticity for 2D wing chords. St=0.45 for all cases.

From the above results, it is clear that the 2D CFD results can achieve qualitative agreement with 3D CFD results when the LEV shedding frequency of the 2D wing matches with the flapping frequency of the wing (i.e. LEV shed at the end of the downstroke). This indicates that the flow characteristics can be captured relatively well when this flow condition is achieved. This result provides a means of investigating the complex 3D flow using simplified 2D model, and will be used for flow analysis of flapping wings in the following chapter. Furthermore, the above results also show that the QS model results are in quantitative agreement with 3D CFD results from previous study for the specified wing kinematic case.

4.3.2 Comparison with 3D CFD results

To further validate the compatibility of the QS aerodynamic model in different kinematic conditions, the aerodynamic lift and rotational moment at different Re and wing kinematics are compared with the results from 3D CFD method. For this calculation, the wing geometry and kinematic definitions follows the data provided in (Wu, Wang and Zhang, 2015).

Different kinematic cases varying the flapping amplitude ϕ, the geometric AoAs (α_u and α_d), and the periodic ratio of flapping to rotation n (defined as the ratio of flapping period Tf to rotation period Tr: $n=Tf/Tr$ (Wu, Wang and Zhang, 2015)) are used for this calculation. The kinematic parameters and the resulting mean lift and rotational moment coefficients are presented in Table 4-1. Figure 4-5 shows the comparison of instantaneous lift and rotational moment coefficients (C_L and C_M).

For the FWR wing, the applicability of the quasi-steady model relies essentially on the stability of LEV. This flow structure has been observed on insect wings by both experimental and numerical methods. By observing the flow structure of a hawkmoth (Manduca sexta) wing in a typical motion, Ellington et al. (Ellington et al., 1996) found a strong spanwise flow along the LEV core. Based on this observation, they proposed that LEV could be stabilized by the spanwise flow which transports vorticity of the LEV towards wingtip, thus delays the shedding of LEV. Lim et al (Lim et al., 2009) through experimental and numerical

methods found that the LEV could be stabilized due to vortex stretching even with a weak spanwise flow. By examining the LEV dynamics of unidirectional rotating wing with different *Ro*, Lentink and Dickinson (Lentink and Dickinson, 2009) found that the LEV could be stabilized at low *Ro* by centripetal and Coriolis accelerations, which mediates the spanwise flow by the effect of 'Ekman pumping' of the boundary layer flow. In the numerical study of Wu et al (Wu, Wang and Zhang, 2015) on FWR, a strong spanwise flow on the wing was observed, and the LEV on the FWR wing merged with the tip vortex and the TEV, forming a vortex ring structure that stayed attached on the wing throughout the flapping cycle. These findings suggest that the quasi-steady model is applicable for modelling the aerodynamic forces of FWR and other wing motions in low *Ro* and *Re* flight.

For a particular wing, the quasi-steady coefficients are sensitive to the wing geometry and flow conditions. Lee et al (Lee, Lua and Lim, 2016) numerically investigated the effect of *Ro* and AR for revolving rectangular wings. They found that both *Ro* and AR have considerable effect on the vortex dynamics and thus the forces production on the wing. In particular, increasing the AR reduces the three-dimensional tip effect and is thus beneficial to lift generation, while increasing the *Ro* increases LEV instability, which is detrimental to lift production. In the current study, the quasi-steady coefficients for FWR are obtained by an empirical fit of CFD data for our particular wing geometry, *Ro* and *Re*. The results of our model are in good agreement with CFD method in full range of investigations. As shown in Figure 4-5 and Table 4-1, compared with CFD, the current model yields maximum differences in lift and rotational moment coefficients of less than 12% and 15%, respectively.

Table 4-1 Time averaged coefficients ($\bar{C}_L$, $\bar{C}_M$) by quasi-steady model and CFD method.

Kinematic Parameters					CFD Results		QS Results	
Case No.	φ	n	$α_u$	$α_d$	$\bar{C}_L$	$\bar{C}_M$	$\bar{C}_L$	$\bar{C}_M$
1	20°	0.25	25°	5°	5.11	-2.38	5.06 (-1.0%)	-2.42 (1.6%)
2	30°	0.25	30°	10°	3.27	-1.57	3.32 (1.4%)	-1.69 (7.4%)
3	30°	0.25	30°	0°	2.81	0.77	2.68 (-4.6%)	0.76 (-2.1%)
4	30°	0.13	25°	5°	1.00	1.33	1.08 (8.6%)	1.42 (6.2%)
5	70°	0.42	50°	-30°	0.92	2.39	1.02 (11.7%)	2.55 (6.8%)
6	70°	0.33	60°	-20°	1.55	1.53	1.70 (9.5%)	1.75 (15%)
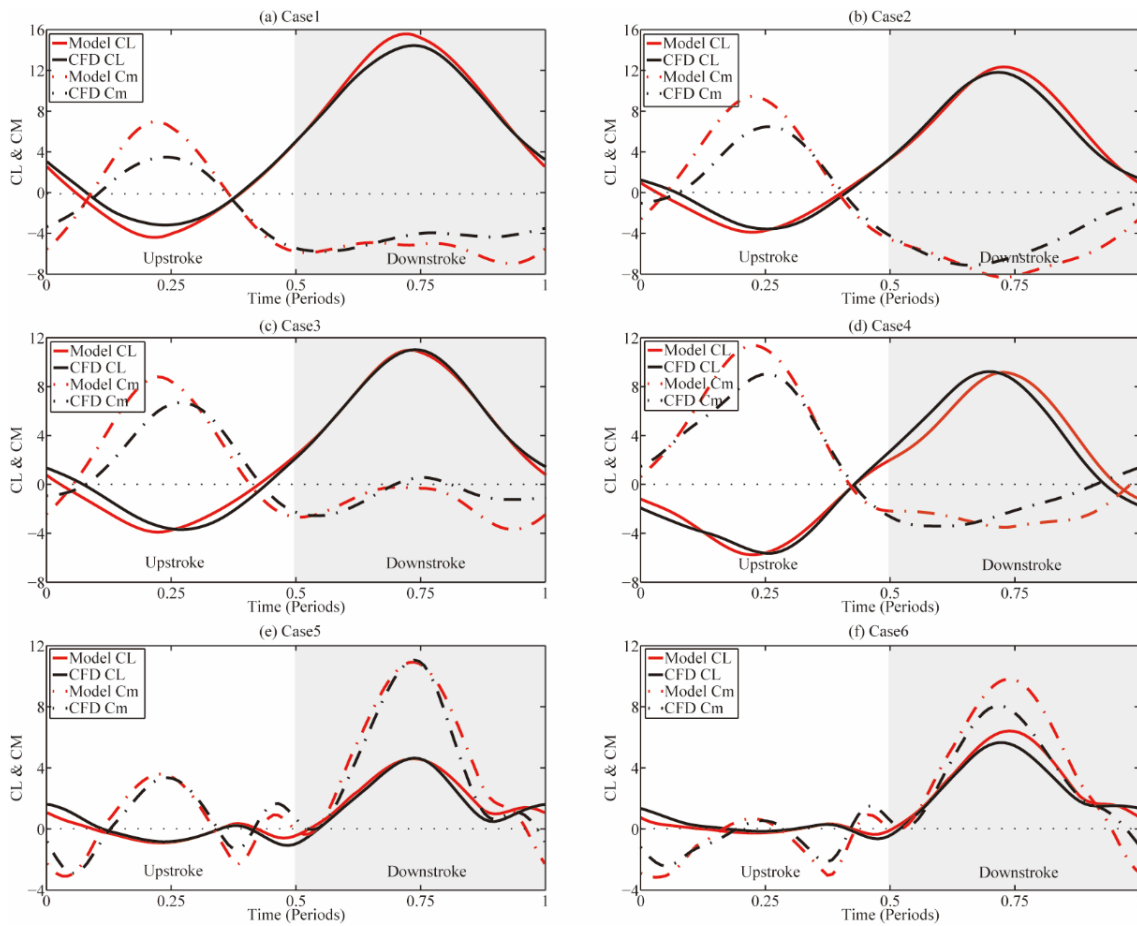
Figure 4-5 Lift and rotational moment coefficients (C_L and C_M) comparisons of the quasi-steady model and CFD method.

4.4 Summary

In this chapter, a quasi-steady aerodynamic model for flapping wing flight at low *Re* is developed and validated. The applicability of the aerodynamic model relies essentially on the fact that the flow associated with the flapping wing at low *Re* has the well-established structure of a stable LEV, i.e. a vortex structure accumulated on the leading edge of the wing and stay attached throughout the flapping cycle. Empirical data from previous experiments and CFD analysis are used in this model to account for various unsteady effects, including stable LEV, rotational forces and added mass effects.

The QS model is first compared with 2D CFD modelling at different span-wise locations for a particular wing and kinematic case. The results show that the QS model results for the instantaneous forces of flapping wing are in qualitative agreement with the 2D CFD results. In addition, the results imply that when the LEV shedding frequency of the 2D wing matches with the flapping frequency, the vortices structure obtained from 2D CFD modelling would be in close agreement with that of the flow structure of a 3D wing with stable LEV.

A further comparison of the QS model with 3D CFD analysis results is carried out by setting the wing motion in various kinematic cases with different flapping amplitude, wing pitch angle and rotating speeds. The results show that both the instantaneous force production and the averaged values of the QS model are in good agreement with 3D CFD results in full range of investigations.

5 AERODYNAMIC EFFICIENCY OF A NOVEL BIO-INSPIRED FLAPPING WING ROTOR

As indicated in section 2.1, bio-inspired flapping wing has several aerodynamic benefits for the application of MAV in comparison with the conventional fixed wing or rotor. The superiority of flapping wings is demonstrated by the extraordinary flight skills of natural flyers such as insects or birds. In particular, flapping wing produces higher lift force than conventional airfoil at AoA above the stall angle, due to the delayed stall of the LEV (Berg and Ellington, 1997a, 1997b; Ellington et al., 1996). On the other hand, flying insects and birds have shown extraordinary capability of vertical take-off, landing, hovering and manoeuvrability. These features of the flapping wing have brought strong interest in developing MAVs that mimic the wing motion of insects or birds(Lentink, 2013; Ma et al., 2013).

In this chapter, investigations are made into the kinematics of a flapping wing rotor described in the previous chapter, which combines bio-inspired flapping wing and man-made rotor. Based on the quasi-steady aerodynamic model developed in the previous chapter, the aerodynamic efficiency of the two functions of the wing, i.e. generating propulsive thrust and producing weight suspending lift are investigated, respectively. The dimensionless Strouhal number *St*, which governs the vortices shedding for oscillating airfoil in the free stream and is closely related to flapping wing propulsion are further analysed for the FWR wing motion. Finally, the aerodynamic efficiency of FWR at equilibrium rotating speed is studied in comparison with the optimal efficiency for prescribed wing kinematics.

5.1 Propulsion and Weight Suspension of Flapping Wing

One of the features that differentiate animal flapping wings from conventional fixed wing and rotors is that flapping wings produce both propelling thrust against the aerodynamic drag and vertical lift sustaining the body weight. For flapping wing flight, the efficiency that measures the wing motions is therefore defined by either the efficiency for producing propulsive thrust or vertical lift,

depending on the situation. For both aeronautical vehicles and flying animals, their wings produce lift to support weight in the air, the aerodynamic efficiency for these flyers is therefore often defined by the cost of energy to stay aloft or to travel a certain distance. For example, the current studies on insect flight primarily focus on a 'normal hovering' state, where the aerodynamic force of the flapping wings in a flapping cycle averages to a net lift. The aerodynamic efficiency for such wings is therefore mainly concerned with the production of lift for a given power. On the other hand, moving animals such as swimming fish and cruising flyers use their wings or fins to produce thrust against the drag of the fluid, for which the propulsive efficiency associated with thrust production is often used to measure the efficiency of their movement of wings or fins.

For flying and swimming animals, a dimensionless parameter which describes the kinematics of their wings or fins is the Strouhal number St (Taylor, Nudds and Thomas, 2003; Triantafyllou, Triantafyllou and Grosenbaugh, 1993; Triantafyllou, Triantafyllou and Gopalkrishnan, 1991). This dimensionless number is known to govern a well-defined structure of the wake shed from an oscillating airfoil in the free stream, and is closely related to the efficiency of flying and swimming animals for propulsion (Taylor, Nudds and Thomas, 2003; Triantafyllou, Triantafyllou and Grosenbaugh, 1993). In particular, optimum propulsive efficiencies are found for wing motions with St lying between 0.2 and 0.4, corresponding to a stably formed wake structure and average velocity profile equivalent to a jet (Anderson et al., 1998; Read, Hover and Triantafyllou, 2003; Taylor, Nudds and Thomas, 2003; Triantafyllou, Triantafyllou and Grosenbaugh, 1993; Triantafyllou, Triantafyllou and Gopalkrishnan, 1991). Further extensive literature reviews on data from flying and swimming animals showed that many animals cruise at this interval of St (Taylor, Nudds and Thomas, 2003; Triantafyllou, Triantafyllou and Grosenbaugh, 1993).

The existing studies on flapping wing efficiencies have been primarily focused on one of the above two aspects. For the normal hovering kinematics of insects, since the body assumes no forward speed, the flapping wing produces no net thrust in a flapping cycle. Thus, the aerodynamic efficiency for producing lift is of

primary concern. On the other hand, most studies on the undulatory swimming fish tails have been devoted to propulsion, while the force perpendicular to the free stream in the form of lift is of secondary factor. However, natural flyers in cruising flight use their flapping wings to generate both lift and thrust. The aerodynamic efficiency of such wing motion in terms of both propulsive efficiency and efficiency of lift production has received less study.

For animals in cruising flight, the equilibrium between the thrust produced by the flapping wing and the aerodynamic drag results in a wing kinematics pattern that closely resembles the wing motion of the FWR, as shown in Figure 1-1. In this study, the dichotomy of the two functions for flapping wing flight is addressed. Investigations have been made into the aerodynamic efficiency for producing both vertical lift and horizontal thrust of the FWR kinematics. The QS aerodynamic model presented in chapter 4 is used to calculate the aerodynamic force and power of the wing. Additionally, analysis using a 2D CFD model is carried out to capture the transient status of the flow field and unsteady forces. A typical wing model of elliptical shape and aspect ratio λ=3.6 and semi-span R=98mm is chosen for the FWR wing model. The wing flapping motion follows a simple harmonic function at a constant rotating speed. The wing flapping frequency is f=10Hz, flapping amplitude ϕ=70° corresponding to Re of 2500.

The results of this study show that both the propulsive efficiency and efficiency for producing lift of the FWR wing peaks within a narrow interval of St: between 0.1 and 0.5 for certain range of wing pitch angles, which agrees closely with reported data of natural flyers in cruising flight (Taylor, Nudds and Thomas, 2003); however, the St for high efficiency of lift and high efficiency of propulsion in general differs. The higher propulsive efficiency corresponds to St between 0.2~0.5 and the higher efficiency of lift corresponds to St between 0.1~0.3; in particular, the St for the rotational equilibrium state of the wing lies between the maximum propulsive efficiency state and the state with maximum efficiency of lift state. Furthermore, systematic calculations show that high efficiency of lift (above 85% with respect to maximum Pf) can be obtained at the natural equilibrium state for wide range of prescribed wing kinematics. Insights of the

results for biological flyers in cruising flight as well as for MAVs design are provided.

5.2 Propulsive Efficiency versus the Efficiency of Lift

5.2.1 Flapping flight efficiency against the Strouhal number

The FWR kinematics makes use of aerodynamic thrust produced by flapping motion to drive the wings rotate about the vertical axis. At the same time, lift is obtained by biasing the pitch angle of the wing in the upstroke and downstroke. In this study, both the propulsive efficiency ηp and the efficiency for producing lift Pf are investigated for the FWR kinematics. These two efficiency measures are calculated in different kinematic conditions defined by the dimensionless St and wing pitch angles.

A FWR wing model with wing shape illustrated in Figure 4-2, and wing semi-span R=98mm, aspect ratio λ=3.6, flapping amplitude ϕ=70°, flapping frequency f=10Hz at Re=2500 is taken for this study. The wing pitch angles are defined for 4 cases, varying from symmetric pitching to asymmetric pitching as: α_d=-15° and α_u=15°, 30°, 45°, 60°. The St for each of the above cases are chosen to vary between St=0.1~1, which determines the rotation speeds of the wing uniquely (η=0.5~5 for the given St range). The computed results for aerodynamic efficiencies (ηp and Pf) and force (moment) coefficients ($\bar{C}_L$ and $\bar{C}_M$) against the St are shown in Figure 5-1, where the open circles indicate rotational equilibrium states $\bar{C}_M = 0$. The St for maximum ηp and Pf at different α_u cases is given in Table 5-1.

As shown in Figure 5-1 (a), the variations of the propulsive efficiency ηp and the efficiency of lift Pf against the St follow a similar trend. As the St increases from 0.1 to 1, both ηp and Pf first increase rapidly to the maximum values and then decrease. It is also observed that both the maximum ηp and Pf occur within a narrow interval of St=0.15~0.5 when the wing upstroke pitch angle is within 15°~45°. However they are complementary hence do not reach maximum at the same time. In one of the extreme cases at the lower end of St=0.19, the

flapping motion of symmetric up and down-stroke pitching (α_d=-15º, α_u=15º) leads to the optimal propulsive efficiency η_p=0.37 at the cost of zero mean lift coefficient (Figure 5-1 (b)) and efficiency *Pf*. When the flapping motion becomes asymmetric with α_u=30º~45º, Figure 5-1 (b) shows that the $\bar{C}_L$ and $\bar{C}_M$ and also *Pf* increased dramatically, but the η_p is reduced. The complementary nature of η_p and *Pf* can also be seen from Figure 5-1 (a) and (b) that the maximum *Pf* always occur at small *St* with negative $\bar{C}_M$, where the FWR wing produces net drag instead of thrust.

(a)

(b)
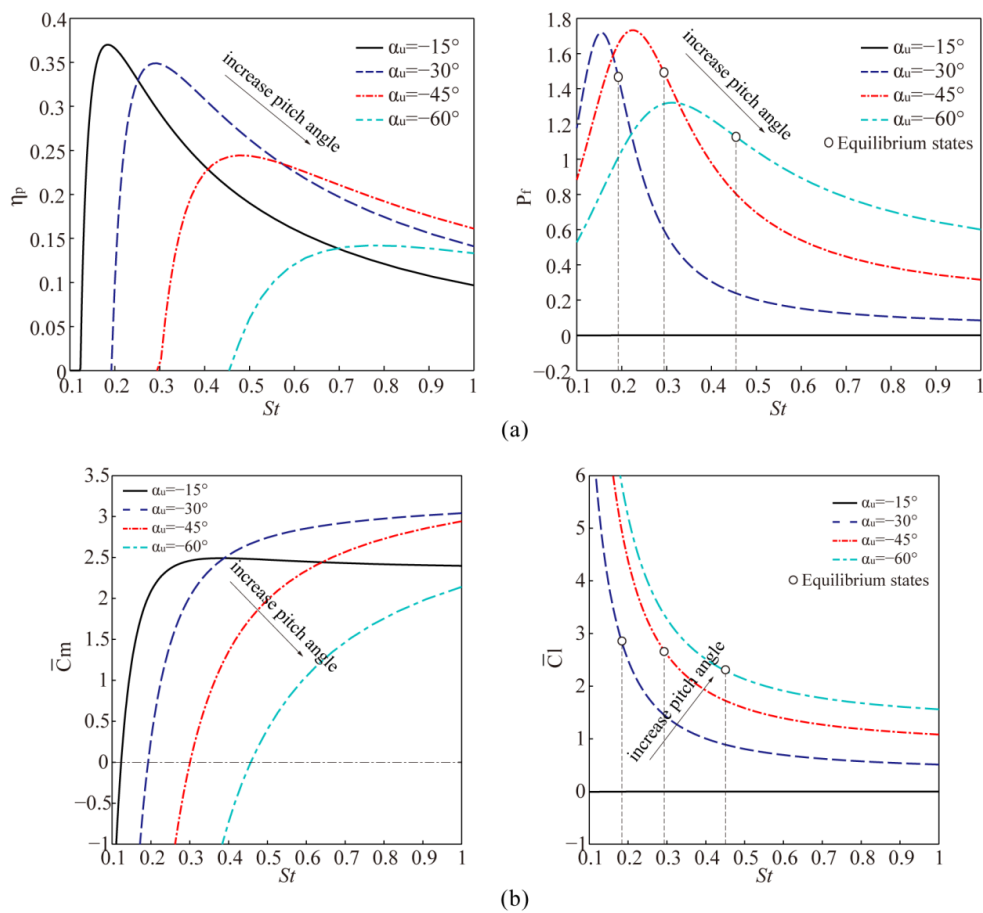
Figure 5-1 (a) Propulsive efficiency η_p and efficiency for producing lift *Pf* against the *St*; (b) mean rotational moment and lift coefficients $\bar{C}_M$ and $\bar{C}_L$ against the *St*.

Table 5-1 The St for maximum ηp and Pf for fixed α_d=-15º.

kinematic case	maximum ηp	St for maximum ηp	maximum Pf	St for maximum Pf
α_u=15º	0.37	0.19	0	/
α_u=30º	0.35	0.29	1.72	0.15
α_u=45º	0.24	0.48	1.73	0.22
α_u=60º	0.14	0.77	1.32	0.31

5.2.2 Flow structure of flapping wing at optimal efficiency states

Previous studies have shown that the propulsive efficiency of flapping airfoils is closely related to the evolution of the flow structure on the wing. Triantafyllou et al (Triantafyllou, Triantafyllou and Grosenbaugh, 1993; Triantafyllou, Triantafyllou and Gopalkrishnan, 1991) studied the propulsive efficiency of 2D oscillating airfoil and proposed that the optimal efficiency is obtained when an airfoil is flapped at the frequency that results in the maximum amplification of the shed vortices, and the velocity profile behind the airfoil is in the form of an inverted von Kármán vortex street indicative of a jet. Later, by using an inviscid panel method to investigate the wake structure of a 2D oscillating airfoil, Jones et al (Jones, Dohring and Platzer, 1998) noted a remarkable similarity between the simulated wake and the experiment wake structure, indicating that the formation of the well-defined wake structure is essentially an inviscid phenomenon.

At low Re and large AoA, the well-defined structure of the wake is complicated by the flow separation at the leading edge and interactions with the vortices shed from the trailing edge. Wang (Wang, 2000) studied the flow over a impulsively started 2D airfoil using CFD method and observed that the thrust production is correlated with the time scale that governs the shedding of the LEV. He proposed that optimal efficiency is obtained when the duration of the flapping stroke is inside the 'thrust window' that exists before the LEV is shed.

In view of the previous results in 2D, the optimal kinematic cases (shown in Figure 5-1 and Table 5-1) that result in the highest propulsive efficiency and

efficiency of lift are taken to investigate the 2D flow and forces. The 2D calculations are conducted for the cases with symmetric pitch angles: α_d=-15°, α_u=15° and St=0.19, and asymmetric pitch angles: α_d=-15°, α_u=30° with St=0.29, that yield the maximum ηp; and the case with: α_d=-15°, α_u=45° and St=0.22 that yields the maximum Pf. The calculated time courses of forces and flow for maximum ηp cases are shown in Figure 5-2.

In Figure 5-2, large thrust is produced in both the upstroke and downstroke for the two cases. In the symmetric pitching case, the production of thrust is equal in the up and downstroke; while in the asymmetric pitching case, the thrust produced in the downstroke is larger than in the upstroke. Figure 5-2 (a) shows that the LEVs of the symmetric pitching case are of equal strength on both sides of the wing in the up and downstroke, which contributes equally large thrust in each stroke. In contrast, Figure 5-2 (b) shows that asymmetric LEVs are formed on the wing for the asymmetric pitching case. In the downstroke, a strong LEV is formed on the upper wing surface which contributes significant lift and thrust; while in the upstroke, a weak LEV is formed on the lower wing surface which contributes small thrust and negative lift.

It is observed that the scales of the LEVs associated with the above cases are relatively small. This is due to the small effective AoA at the given St. In general, the formation of LEV decreases the propulsive efficiency, as indicated in previous studies for oscillating 2D airfoils (Heathcote, Martin and Gursul, 2004; Isogai, Shinmoto and Watanabe, 1999; Tuncer and Kaya, 2005). However, LEVs also serves as a source of thrust production. It is noted that the St serves to balance these two effects. As shown in Figure 5-2 (b), when St decreases from moderate to small value, a transition from large rotational moment to negative is observed, indicating a decrease of the effective AoA from large value to negative. Maximum propulsive efficiencies occur at medium St, where small positive effective AoA forms small LEV, as shown in Figure 5-2.
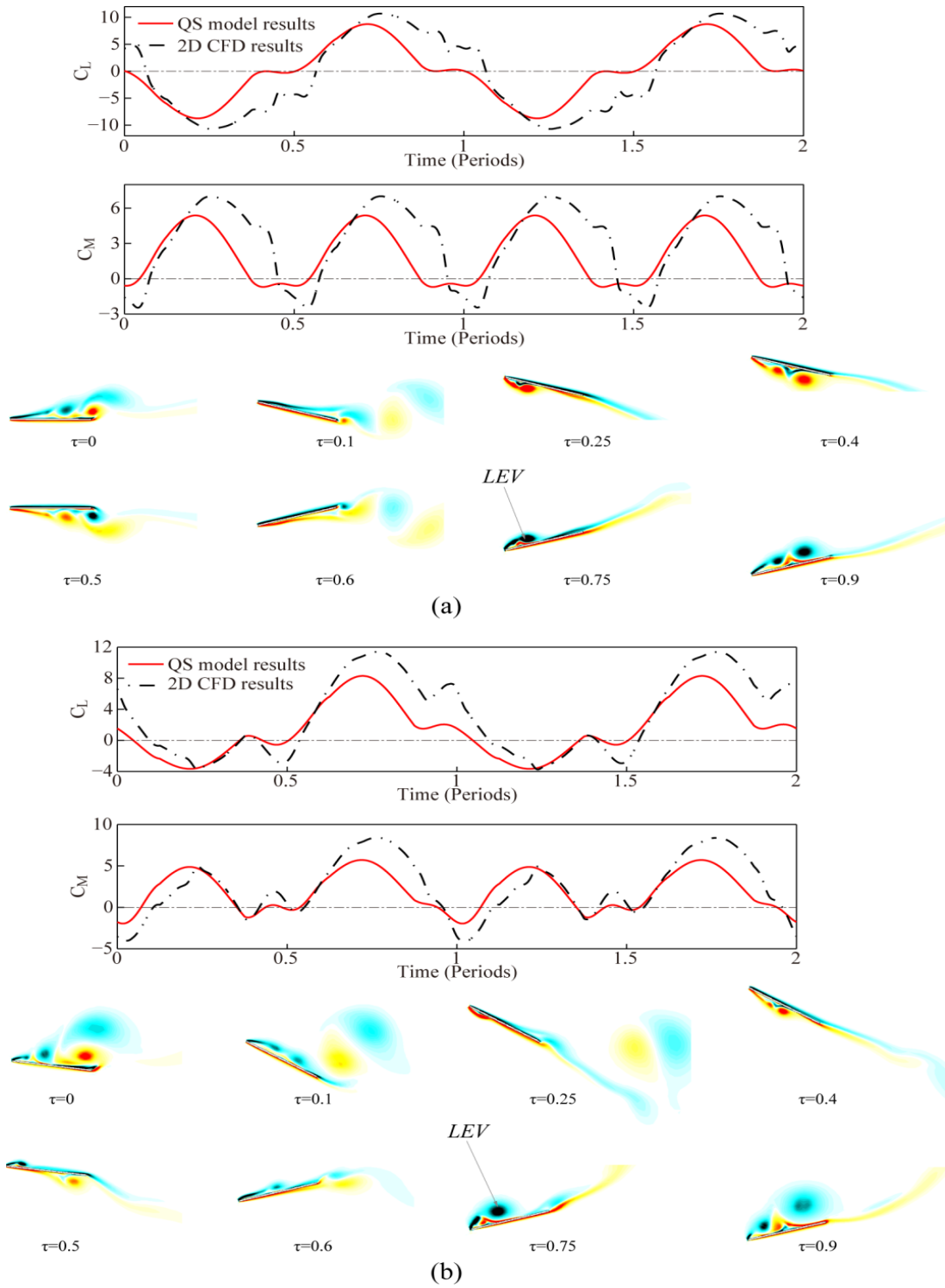
Figure 5-2 Time courses of C_L and C_M and vorticity contours for maximum ηp cases. (a) Symmetric case: α_d=-15º, α_u=15º at St=0.19; (b) asymmetric case: α_d=-15º, α_u=30º at St=0.29.

Figure 5-3 shows the time courses of lift, rotational moment and 2D flow structure of the wing for the maximum *Pf* case with an even larger pitch angle (α_u=45°). The forces and moments of the 2D CFD results follow qualitatively the trends of the 3D QS forces and moments. However, disturbances of the 2D forces are observed due to the shedding of LEVs. In this case, lift is produced in both upstroke and downstroke. Large anti-rotating moment is produced in the upstroke and only a small rotational moment is produced in the downstroke. It is noted that in both up and downstroke, large LEVs are formed on the upper surface of the wing and significant vortices shedding are observed near the end of each stroke. This is most likely due to the fact that the wing has consistently large effective AoA in a whole flapping cycle at this *St*.
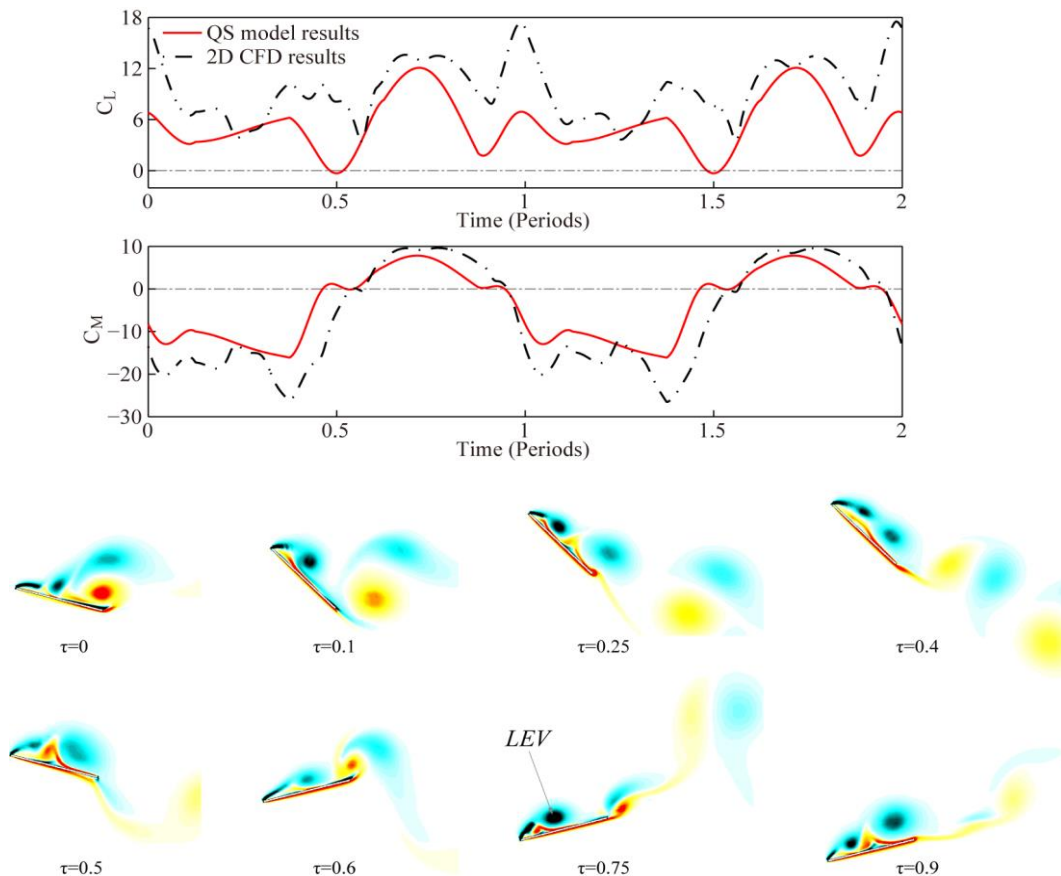
Figure 5-3 Time courses of C_L and C_M and vorticity contours for maximum *Pf* case: α_d=-15°, α_u=45° and *St*=0.22.

From the above analysis, it is noted that as the wing pitch angles change from symmetric to asymmetric in the up and downstroke, a transition of the LEVs structure from symmetric to asymmetric is observed. The asymmetry of the LEV structure on the wing surface results in net lift production. However, as the flow forms large LEV in the downstroke, higher power are required to overcome the vertical lift force, which leads to a diminished propulsive efficiency. The transition of the flow structure from symmetry to asymmetry thus indicates a transfer of flapping energy from propulsion to weight suspension.

5.3 Aerodynamic Efficiency of Passive Rotating Wing

When the FWR wing is free to rotate horizontally, the rotation speed will reach an equilibrium state when the mean rotational moment over a flapping cycle is zero. The rotational equilibrium state of the FWR kinematics has been proposed for design of MAVs. Several previous studies have shown that this kinematics may have certain benefits in terms of system simplicity and aerodynamic efficiency compared with other conventional type (fixed wing, rotary wing and insect-like flapping wing) when applied for MAV design (Guo, Li and Wu, 2012; Jianghao, Chao and Yanlai, 2017; Li et al., 2016). Apart from practical applications, the passive rotating kinematics also has a noticeable similarity with the cruising flight of natural flyers, where the flapping wings produce both lift and thrust, and the cruise speed is determined by the equilibrium of the body drag and the flapping propulsive thrust.

The present investigation focuses on the rotational equilibrium state of the FWR wing. Since the wing produces no net propelling moment at this state, the efficiency for producing lift *Pf* is of particular interest. In this investigation, the aerodynamic efficiency at the equilibrium state is compared with the maximum aerodynamic efficiency, which is the highest aerodynamic efficiency that can be obtained by actively tuning the rotation speed (or equivalently the *St*) of the wing. The efficiency for producing lift at the rotational equilibrium state is denoted by *Pfe*, while the maximum efficiency for the given wing pitch angles (α_d and α_u) is indicated by *Pfm*.
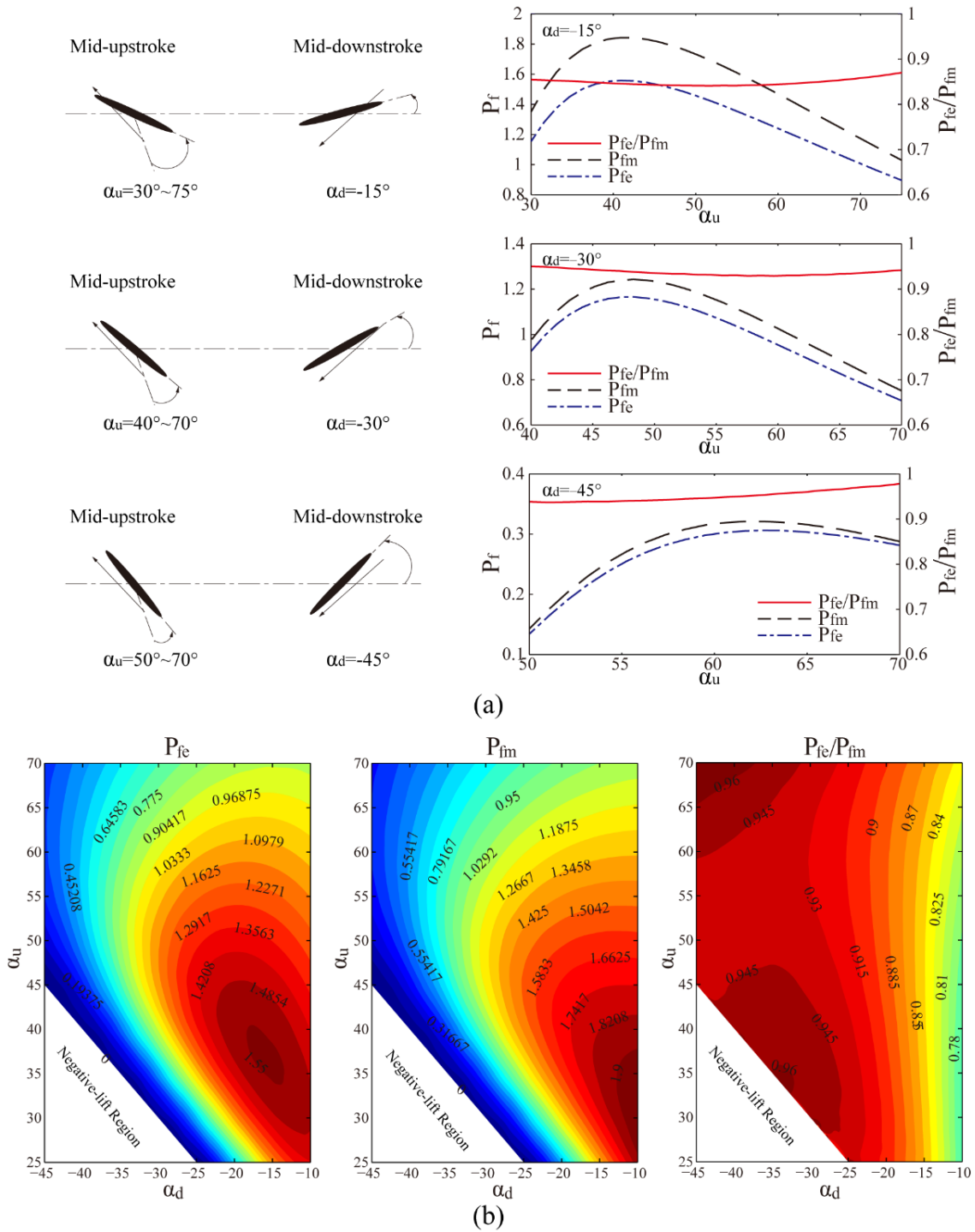
Figure 5-4 The variations of efficiency at equilibrium state *Pfe*, the optimal efficiency *Pfm* and the ratio *Pfe*/*Pfm* with α_d and α_u. (a) Variations of efficiencies with α_u for fixed α_d=-15º, -30º and -45º; (b) Efficiency contours for α_u=25º~70º and α_d=-45º~-10º.

In this investigation, the two efficiencies *Pfe* and *Pfm* are calculated with the downstroke wing pitch angle α_d range between -45°~-10° and the upstroke wing pitch angle α_u range between 25°~70°. Specifically, the individual cases when α_d is fixed at -15º, -30º and -45º are chosen to analyse the efficiency variations with α_u. For all the cases, the wing semi-span is taken as *R*=98mm and the flapping frequency *f*=10Hz, flapping amplitude ϕ=70°, and the *Re*=2500. The variation contours of *Pfe*, *Pfm* and the ratio *Pfe*/*Pfm* with α_u and α_d are shown in Figure 5-4 (b). The efficiency curves with fixed α_d is shown in Figure 5-4 (a). In Figure 5-4 (b), the negative-lift regions correspond to wing kinematic cases with larger negative α_d in the downstroke than positive α_u in the upstroke, which consequently yields negative mean lift force in a flapping cycle.

The results in Figure 5-4 shows that, in general, the efficiencies (*Pfe* and *Pfm*) are sensitive to the variation of wing pitch angles (α_u and α_d). Increasing the downstroke AoA α_d generally leads to decreases in the aerodynamic efficiencies; while the optimal upstroke AoA α_u for *Pfe* and *Pfm* always takes intermediate values between 30°~60°, depending on α_d. However, despite these variations with wing pitch angles, the efficiency at the equilibrium states *Pfe* appears to be very close to the maximum efficiency *Pfm*. In most of the cases (α_d between -45°~-15°), the ratio *Pfe*/*Pfm* is above 85%; furthermore, when the downstroke wing pitch angle is large (α_d between -45°~-30°), the ratio *Pfe*/*Pfm* is above 90%.

The above results imply that for the passive rotating wing, the forces equilibrium of the flapping propulsive thrust and anti-rotating drag in a flapping cycle leads to high aerodynamic efficiency. This feature of the passive rotating wing may be favourable for bio-inspired MAV design, since the rotation speed automatically converges to a high efficiency state. Furthermore, since flapping wing flyers in cruising flight is in a state of equilibrium where the thrust produced by their flapping wings balances with the drag from the air, the above results imply that cruising flyers may benefit from this natural equilibrium to gain high aerodynamic efficiency.

In order to fully characterize the kinematics of the three status of the wing, i.e. the maximum propulsive efficiency state, the state with maximum efficiency of lift and the equilibrium state, the St of these respective states at different wing pitch angles are calculated. It should be noted that since the St serves to determine the production of aerodynamic forces from propulsive thrust to anti-rotating drag, the St at equilibrium state stands in the middle of the other two states.
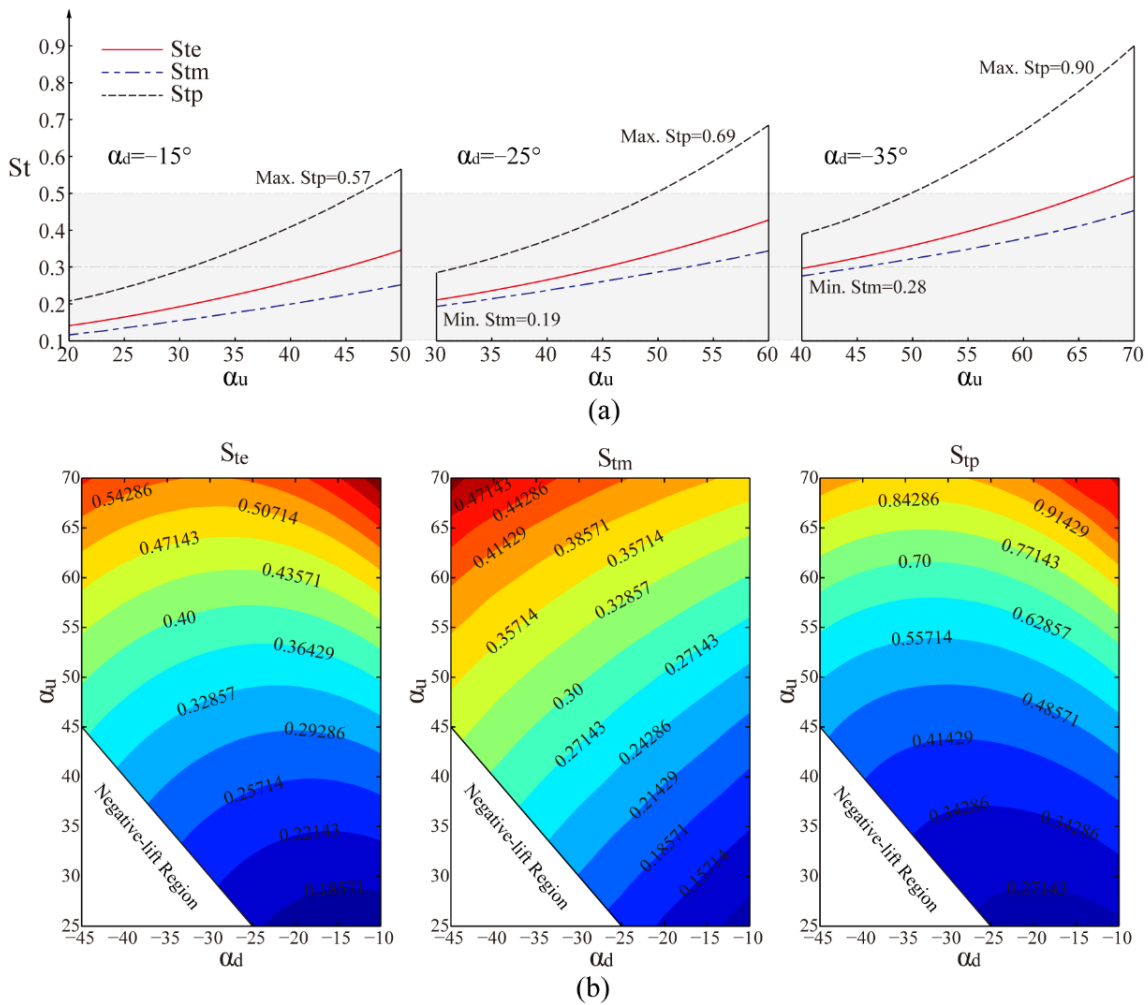
Figure 5-5 Distributions of St in typical states with the wing pitch angles $α_u$ and $α_d$. (a) Ste, Stm and Stp variations with $α_u$ for fixed $α_d$=-15°, -25° and -35°, (b) Contours of Ste, Stm and Stp for $α_u$=25°~70° and $α_d$=-45°~-10°.

Figure 5-5 (a) shows the variations of St with α_u for fixed α_d cases; the full contours of St at different wing pitch angles are shown in Figure 5-5 (b). In Figure 5-5, the St for maximum ηp states are denoted by Stp, for maximum Pf states are denoted by Stm, and for equilibrium states are denoted by Ste.

The variations in Figure 5-5 (a) shows that the St for typical states (Ste, Stm and Stp) decrease monotonically with the increase of α_u. Both Figure 5-5 (a) and (b) show that reducing the wing pitch angle (i.e., increase of α_u and decrease α_d) lowers the St for the high efficiency states, indicating that higher efficiency (ηp and Pf) are obtained at higher rotation speed at small wing pitch angles (since St is inversely proportional to the rotation speed).

Figure 5-5 (b) shows that for most of the kinematic cases with $\alpha_u=25^o{\sim}70^o$ and $\alpha_d=-45^o{\sim}-10^o$, the St at equilibrium state Ste and maximum Pf state Stm fall in the interval between 0.1~0.5; while the St at maximum ηp appears to be higher within 0.2~0.9 for most of the cases. Particularly, the distribution of the data shows that when the upstroke AoA is small, i.e. α_u less than 45°, nearly all the St for high efficiency states Stm, Stp and the equilibrium state Ste converge to the interval of 0.1~0.5. The lower end of St (between 0.1 and 0.3) corresponds to high Pf, while the higher end (between 0.2 and 0.5) corresponds to high ηp. These results are in close agreement with previous reported data of flying animals in cruising flight, which show that many natural flyers cruise at St between 0.2 and 0.4 (Taylor, Nudds and Thomas, 2003). The above results indicate that the various wing kinematics of flapping wing flyers in cruising flight may result in high aerodynamic efficiency states of for both lift production and propulsion, although these two efficiencies cannot be optimized at the same time.

5.4 Summary

In this chapter, the aerodynamic efficiency of the FWR kinematics which combines vertical flapping motion and passive horizontal rotation is investigated. The propulsive efficiency ηp for producing horizontal thrust and the efficiency for producing vertical lift Pf is investigated using a wing model of

elliptical shape with wing semi-span R=98mm, wing aspect ratio λ=3.6, flapping frequency f=10Hz, and flapping amplitude ϕ=70° at Re=2500.

The calculated data show that both the propulsive efficiency ηp and efficiency of lift Pf depend on the dimensionless St and wing pitch angles (α_u and α_d). For small wing pitch angle (α_u less than 45°), both efficiencies η_p and Pf are found to peak at St between 0.1 and 0.5. However, these two efficiencies are complementary to each other: when maximum ηp is obtained, the Pf is relatively low; while maximum Pf always occurs when the flapping wing produces net drag instead of thrust. In particular, high efficiency of lift production are found when St is between 0.1 and 0.3, which is in general lower than the St for high propulsive efficiency (between 0.2 and 0.5). Further analyses of the 2D flow of the wing in typical kinematic states show that the production of lift and thrust is closely related with the LEV structure on the wing. Maximum ηp occurs when the wing forms small and symmetric LEVs in the up and downstroke; while asymmetric LEVs large in the downstroke is associated with the production of lift and decrease in propulsive efficiency ηp.

The rotational equilibrium state of the FWR kinematics is also investigated. The results show that the aerodynamic efficiency at this state Pfe is above 85% compared with the maximum efficiency Pfm for a wide range wing kinematics. Furthermore, systematic calculations on different wing pitch angles (α_u and α_d) show that most of the St for the high efficiency states (maximum Pf state and maximum ηp state) and the equilibrium state of the wing are within the interval St=0.1~0.5. These results show that the natural equilibrium between thrust and drag of the flapping wing results in a state of high aerodynamic efficiency. The agreement of our results with reported data of cruising flight of animals indicates that flapping wing flyers may benefit from this equilibrium to gain high efficiency for both lift and thrust production, although these two efficiencies cannot be optimized at the same time. The results also have implications for bio-inspired MAV design, since for the passive rotating kinematics of FWR, no fine tuning of the rotation speed is needed to achieve a high efficiency state.

6 AERODYNAMIC FORCE AND EFFICIENCY COMPARISON OF THREE TYPES OF WINGS

Although the flapping wing of animal flight in nature has demonstrated extraordinary capability in manipulating the unsteady low Re aerodynamics, the performances of such flapping wings in comparison with other configurations of MAV design such as the rotary wing has not been studied systematically. In addition, the novel kinematics of the FWR which was described in the last chapter seems to provide great potential for MAV applications. Therefore, it is of great interest to compare the performance of the FWR in terms of aerodynamic efficiency and lift production with the conventional type of MAVs.

In this chapter, first of all, the effect of pitch angles and dimensionless rotation speed for lift production and efficiency of FWR at equilibrium state are analysed using the QS aerodynamic model described in section 4.2. The optimal kinematics of FWR for both lift and efficiency has been determined. The aerodynamic performances of FWR are then compared with the other two competitive wings for MAVs, i.e. the insect flapping wing and Rotary Wing (RW) capable of VTOLH. For the insect flapping wings, comparisons are made with two types of kinematics namely the Horizontal Flapping (HF) and Inclined Flapping (IF) demonstrated typically by fruitfly and dragonfly respectively.

In this study, a wing model with aspect ratio AR=3.6 and of 200mm span at Re=3500 is taken as an example for analysis. The kinematics for both FWR and the insect wings are set in a simple harmonic motion. To determine the optimal kinematics for FWR, the pitch angle of the wing varies in the range of less than 90º. The wing flaps between the angle of ±25º and at a frequency f=12Hz. The aerodynamic lift and efficiency at the same Re for insect wing and rotary wing are calculated at a specified parameter range chosen from typical insect data. The calculated aerodynamic force, efficiency and comparison of three types of wings are presented.

6.1 Optimal Kinematics of FWR

A unique feature of the FWR is that its rotation is passively induced by the thrust of the flapping wing. This is different from the prescribed motion of insect wings and conventional rotor blades. Consequently, a hovering FWR would reach and stay in an equilibrium rotation speed that the mean aerodynamic thrust balances with the drag of the wing. Thus, the rotational moment would average to zero ($\bar{C}_M = 0$) over a flapping circle. In this study, all the calculations are subjected to the equilibrium state of FWR.

Based on the QS aerodynamic model, the aerodynamic forces and power of FWR at the equilibrium state ($\bar{C}_M = 0$) are calculated at different AoA measured at mid upstroke (α_u) and mid downstroke (α_d). The parameters range between $\alpha_u=0°\sim60°$ and $\alpha_d=-30°\sim0°$. In the investigated cases, the flapping amplitude ϕ is fixed to 50°. The flapping frequency and dimension of the wing is determined to match the specified Re=3500 for the investigation. The resulting dimensionless parameters of the FWR ($\bar{C}_L$, $\bar{C}_p$, Pf and η) are shown in Figure 6-1.

As shown in Figure 6-1, the dimensionless rotation speed of FWR η is maximized at small anti-symmetric AoA in up and downstroke ($\alpha_u=9°$ and $\alpha_d=-9°$). Along the symmetry lines $\alpha_u=-\alpha_d$, nearly no lift is generated ($\bar{C}_L = 0$), thus the power factor Pf remains zero. The power coefficient $\bar{C}_p$ is large at small α_u and α_d where the flapping motion forms large effective AoA. In the special case when the pitch angle is constantly zero ($\alpha_u=\alpha_d=0$), Vandenberghe et al (Vandenberghe, Zhang and Childress, 2004) showed in experiment that the rotation of the wing exhibits supercritical bifurcation, where an inverted von Kármán wake behind the wing was observed and the wing rotates by the associated thrust. The results show that the FWR produces high lift coefficient ($\bar{C}_L > 4.3$) when α_d is between -8°~-2° and α_u between 13°~24°. The power factor Pf is above 1.6 when $\alpha_d=-30°\sim-13°$ and $\alpha_u=35°\sim50°$. The resulting maximum values of $\bar{C}_L$, Pf, $\bar{C}_p$ and η and the associated α_u and α_d are listed in Table 6-1.

113
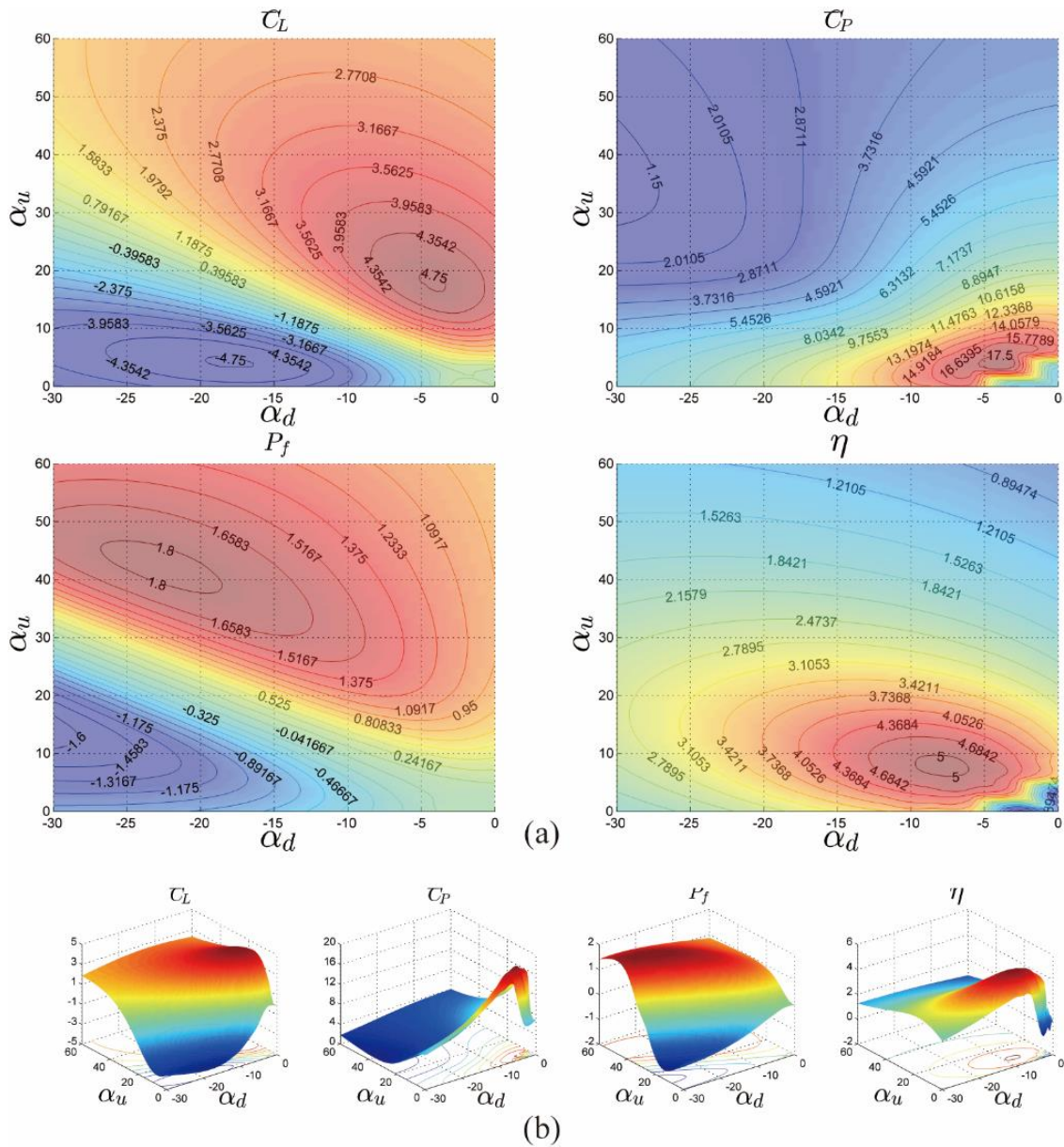
Figure 6-1 (a) Contour plots and (b) 3D surface plots the FWR results in the range α_u=0°~60° and α_d=-30°~0°.

For FWR, the passive rotation speed would deflect the air velocity with respect to the wing which changes the instantaneous effective AoA (α_e). Based on the results obtained from Figure 6-1, the instantaneous α_e of the FWR wing at different η are shown in Figure 6-2 (a). As can be seen, the variations of α_e in a flapping cycle follow a similar trend for different η. In the downstroke, the wing forms large α_e thus produces large lift and propelling moment. In upstroke, the wing forms small positive α_e thus generates a positive though small lift and anti-

114

rotating moment. Subject to the equilibrium condition ($\bar{C}_M = 0$), the propelling and anti-rotating moments cancel each other over a flapping cycle. The resulting AoAs and forces on the FWR wing are illustrated in Figure 6-2 (b).

Table 6-1 The maximum $\bar{C}_L$, Pf, $\bar{C}_p$ and η values and the associated α_u and α_d.

Dimensionless Parameters	Maximum Values	Equilibrium η at Maximum Values	α_u at Maximum Values	α_d at Maximum Values
$\bar{C}_L$	4.73	3.33	18°	-3°
Pf	1.82	1.94	42°	-24°
$\bar{C}_p$	17.21	4.40	6°	-3°
η	5.03	5.03	9°	-9°

From Figure 6-2 (a), the downstroke α_e changes significantly with the rotation speed (η): a large rotation speed (such as η=2.70) produces a small α_e in the downstroke, whereas small rotations speed (η=0.99) results in large α_e in the downstroke. In the former case, the variation of α_e in a flapping cycle appears to be plateaued by the induced rotation speed, thus the aerodynamic force of FWR tends to be dominated by rotation, which is similar to a rotary wing. For the latter case, the wing forms large α_e in the downstroke, whereas a small α_e in the upstroke. The resulting kinematics is similar to a typical insect wing with inclined stroke plane.
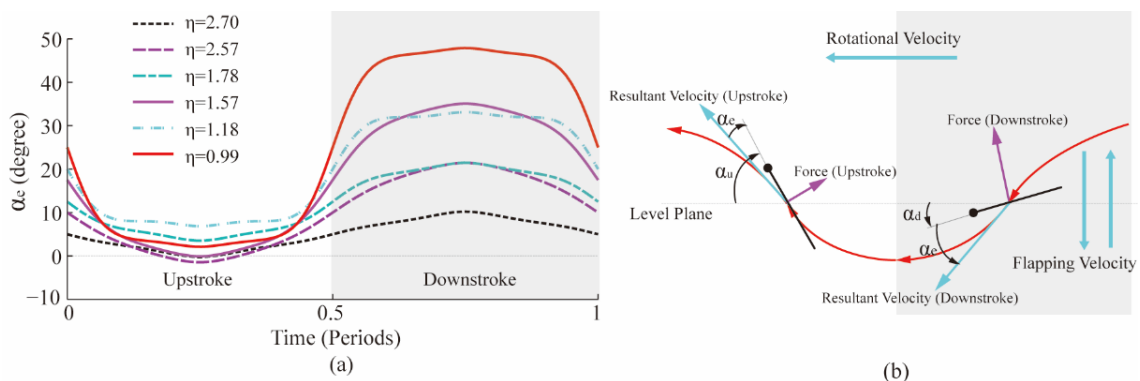
Figure 6-2 (a) The FWR effective AoA, α_e in different rotation speed and (b) the corresponding velocity and aerodynamic forces.

6.2 Instantaneous Force Comparison of FWR with Insect-like Flapping Wings

In order to study the lift production and flight efficiency of the existing types of wings (FWR, insect-HF, IF and rotary wing-RW), comparisons are made between these wing kinematics using the same wing geometry and Re=3500.

Firstly, the instantaneous aerodynamic force of FWR is compared with the insect flapping wings (HF and IF). The kinematic parameters of FWR are chosen by four representative cases of α_u=30°, 60° and α_d=-10°, -20°, respectively. For insect wings, the kinematic parameters are chosen based on data obtained from typical insect flight. In particular, the HF wing is given by: flapping amplitude ϕ_{HF}=150° and α_e=35° in both up and downstroke (Ellington, 1984d), while the IF wing is given by: ϕ_{IF}=90°, stroke plane inclination angle β=40°, and α_e=20° and 45° in the up and downstroke, respectively (Azuma et al., 1985). The kinematics for different wing motions are illustrated in Figure 6-3. Figure 6-4 shows the instantaneous lift and rotational moment coefficients for different wings at Re=3500. The associated mean lift and rotational moment coefficients are given in Table 6-2.
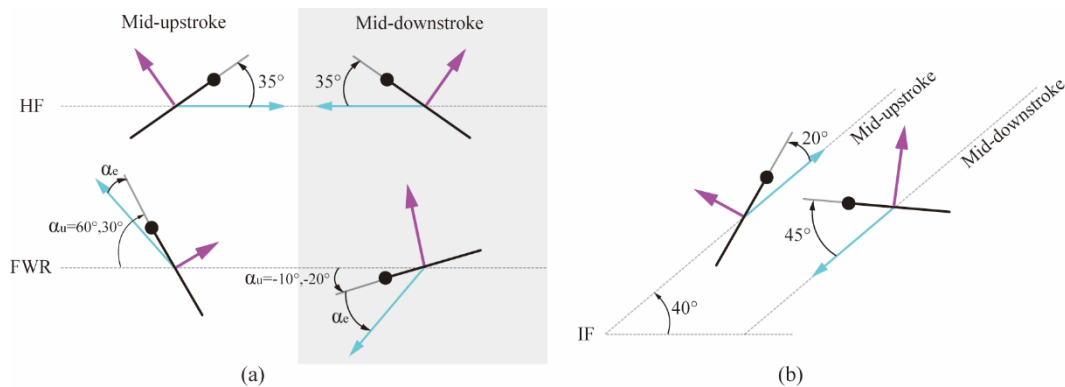
Figure 6-3 Kinematic for FWR and insect flapping wings. (a)-HF and FWR, (b)-IF.

The instantaneous lift of FWR is similar with the IF, where the downstroke produces the majority of lift while the upstroke contributes small or even

negative lift. In contrast, the HF produces equal lift in both up and downstroke. Similar to the IF wing, the large α_e of the FWR wing in the downstroke would produce significant aerodynamic drag (i.e. aerodynamic force parallel to the flow direction). However, a large portion of this drag is contributed to the upward lift due to the vertical flapping velocity. Wang (Wang, 2004) proposed that the aerodynamic drag plays important role for insect flight with an inclined stroke plane: about three quarters of the weight of a dragonfly was supported by the aerodynamic drag. In the above cases of FWR, the drag contribution to the upward lift is between 5%~55%.
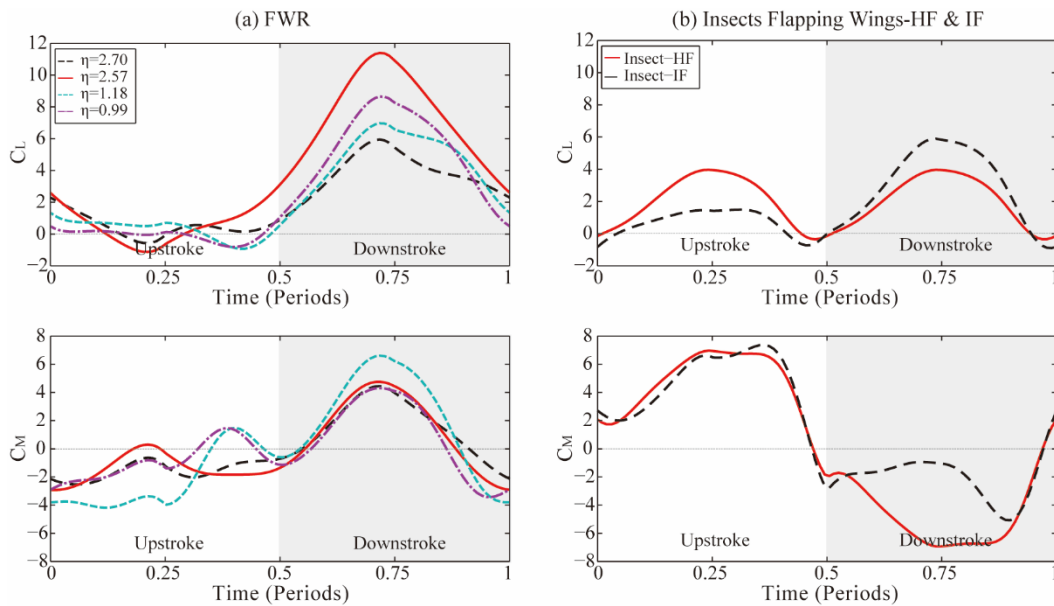
Figure 6-4 Instantaneous C_L and C_M of FWR and insect flapping wing. (a)-FWR, (b)-HF and IF.

For both HF and IF, the wing pitches drastically during a flapping cycle. The typical kinematics of insect wings gives the pitch angles of $\Delta\alpha=110^\circ$ and 115° respectively for HF and IF, whereas the $\Delta\alpha$ of the FWR wing are between $40^\circ\sim80^\circ$. Insect-like flapping wings change the moving direction at stroke reversals, thus the wings need to pitch drastically in order to form a positive α_e in the subsequent stroke. However, due to the induced rotation speed of FWR, a positive α_e can be obtained at a much smaller pitch angle. It is anticipated that

the smaller pitch angle of the FWR wing would be desirable for MAV structural integrity and actuation system requirements.

Table 6-2 Kinematics and corresponding $\bar{C}_L$ and $\bar{C}_M$ of FWR and insect flapping wings (HF and IF).

Kinematic Cases	AoA at mid-upstroke α_u	AoA at mid-downstroke α_d	η	$\bar{C}_L$	$\bar{C}_M$
FWR	30°	-10°	2.57	3.96	0
	30°	-20°	2.70	2.12	0
	60°	-10°	0.99	2.56	0
	60°	-20°	1.18	2.40	0
HF	α_e=35°	α_e=35°	-	1.99	0
IF (β=40°)	α_e=20°	α_e=45°	-	1.82	1.20

6.3 Lift and Efficiency Comparison of Three Types of Wings

The second comparison is between the optimal lift and efficiency of the three types of wings. In this investigation, the kinematic parameters for each wing are specified to vary in a range. The variations of the kinematic parameters are chosen to cover the optimal lift and efficiency for the respective wings. In particular, the α_u and α_d of FWR are chosen to cover the maximum $\bar{C}_L$ and Pf given in Table 6-1; the insect kinematics are chosen to cover the typical motions of insect flight-HF and IF given in Table 6-2. For FWR and IF, the calculations are performed by fixing α_u or α_d respectively in two different cases. The parametric definitions for this investigation are given in Table 6-3 and Figure 6-5.

By varying the corresponding parameters (α_u or α_d for FWR and IF, α_e for HF and RW), the chosen parametric spaces thus represent the boundary performances in terms of $\bar{C}_L$ and Pf for the respective wings. The resulting Pf versus $\bar{C}_L$ boundaries for the three types of wings are presented in Figure 6-6. The arrows in the figure indicate the variations of Pf and $\bar{C}_L$ with the increase of the associated AoAs. The typical kinematic case of insect HF is marked by★, and the dragonfly kinematics case is marked by▲.

As shown in Figure 6-6, the maximum lift produced by RW is smaller compared with the insect wings (HF and IF) and FWR, but the power factor is greater. This indicates that RW is superior in terms of aerodynamic efficiency among the three types of wings, which is consistent with previous experimental results (Lentink, Jongerius and Bradshaw, 2010; Lentink and Dickinson, 2009). The maximum *Pf* of FWR appears to be slightly smaller than RW, but greater than the insect HF and IF wings. This could be due to the deflection of the flow velocity by the passive rotation speed. As shown in Figure 6-2, the rotation speed of FWR tends to plateau the α_e of the wing in both up and downstroke. Therefore, when combined with a suitable flapping amplitude and frequency, the wing of FWR can operate at a relatively constant α_e of high lift to drag ratio, thus produces a higher efficiency, which is similar to the RW operating in a constant AoA.

Table 6-3 Kinematic parameters and optimal kinematics for three types of wing - FWR, insect-like wings (HF, IF) and RW.

Kinematic Cases		AoA Range-Upstroke	AoA Range-Downstroke	Optimal Kinematics for $\bar{C}_L$ and *Pf*				
				$\bar{C}_L$	*Pf*	η	AoA-Up	AoA-Down
FWR	Opt $\bar{C}_L$	α_u=3°~60°	α_d=-3°	4.73	0.98	3.33	α_u=18°	α_d=-3°
	Opt *Pf*	α_u=42°	α_d=-42°~0°	2.29	1.82	1.94	α_u=42°	α_d=-24°
IF	Opt $\bar{C}_L$	α_e=20°	α_e=0~90°	1.93	0.83	-	α_e=20°	α_e=60°
	Opt *Pf*	α_e=0~90°	α_e=45°	1.77	0.96	-	α_e=13°	α_e=45°
HF	Opt $\bar{C}_L$	α_e=0~90°		2.04	0.90	-	α_e=42°	
	Opt *Pf*			1.29	1.56	-	α_e=14°	
RW	Opt $\bar{C}_L$	α_e=0~90°		1.70	1.13	-	α_e=45°	
	Opt *Pf*			0.72	2.54	-	α_e=12°	

Figure 6-5 The AoA variation range for (a-b)-FWR, (c-d)-insect IF wing, (e)-insect HF wing and (*f*)-RW.

It is also noted that the maximum lift of FWR is significantly greater than the other wing motions. This is mainly due to the additional dynamic pressure provided by the passively induced rotation speed. Read et al (Read, Hover and Triantafyllou, 2003) studied the lift and efficiency of a plunging airfoil operating in the free stream. By measuring the fluid forces on the airfoil in a water tank, they found that when the pitching of the airfoil is biased by an angle, significant $\bar{C}_L$ (on the order of 5.5) can be obtained. By using the CFD method, Wang et al (Wang, Wu and Zhang, 2013) studied a flapping and simultaneously rotating wing with prescribed rotation speed, when the rotation speed is given by a high value, the obtained $\bar{C}_L$ could be significantly higher, along with a large anti-rotating moment. Compared with the current investigation of FWR, since the rotation speed of the wing is induced passively by the aerodynamic thrust, the resulting $\bar{C}_L$ is within 5.0 for the specific Re (on the order of 10^3).
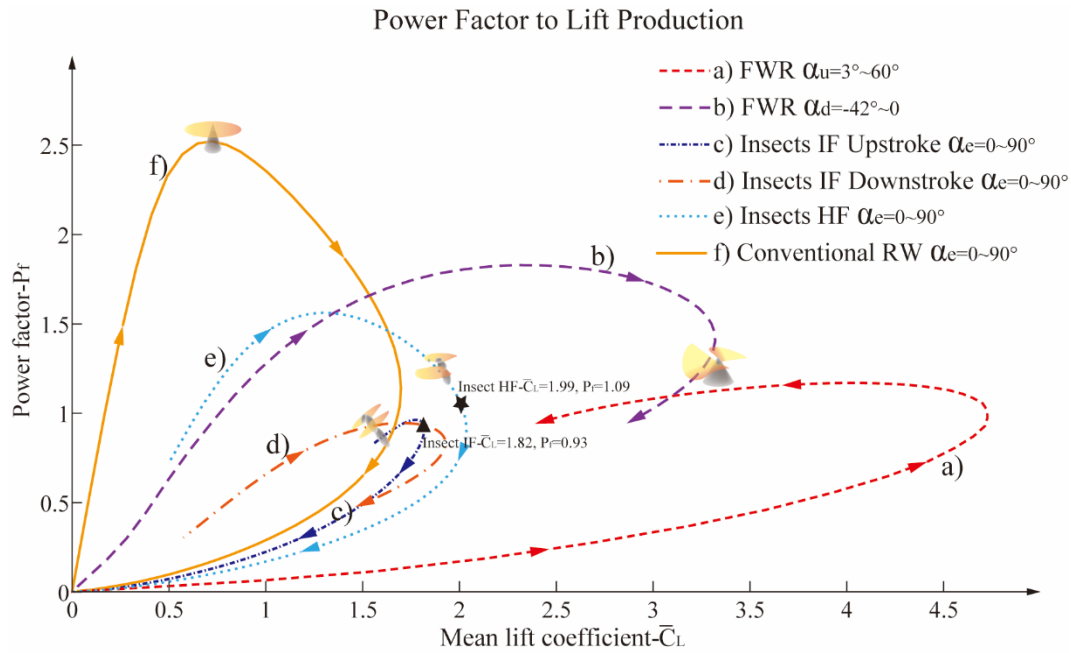
Figure 6-6 Power factor *Pf* versus mean lift coefficient $\bar{C}_L$ boundaries for different types of wings.

For MAV design, our results show that with the same input motion, i.e. flapping frequency and amplitude, the FWR will produce significant greater lift than the insect flapping wings and also the RW. Therefore, when both vertical lift and aerodynamic efficiency are required for a particular MAV, the FWR type of wing motion would be a suitable candidate for the design choices. In addition, the efficiency to lift boundary given in Figure 6-6 provides a guidance to select the design configuration and suitable kinematic parameters according to the MAV design specifications.

6.4 Summary

The bio-inspired FWR provides a novel configuration for MAV applications, which combines the kinematics of both conventional rotary wing and insect-like flapping wings. The FWR rotation is self-propelled in a passive manner by the thrust produced from powered flapping wing motion. This special feature offers not only the capability of VTOLH, but also enhanced aerodynamic performance and simplified mechanical system.

In this chapter, a systematic study has been conducted to quantify the FWR performance in terms of aerodynamic lift and power efficiency in a range of kinematic and geometric parameters. The aerodynamic forces production and efficiency are further compared with the insect-like flapping wing and conventional rotary wing.

The results show that in comparison with the conventional rotary and insect-like flapping wings, the FWR can produce significantly greater aerodynamic lift coefficient with power efficiency between the other two types of wings. The insect-like flapping wings (HF and IF) are of a moderate performance. The rotary wing has the greatest power efficiency of 28% and 39% higher than the FWR and insect-like wing (HF) respectively. However the corresponding lift coefficient of the rotary wing is only 30% and 53% of the other two types of wings respectively. When a rotary wing reaches its maximum lift with compromised power efficiency, the insect wing and FWR can offer 17% and more than double higher lift respectively in the same level of power efficiency. The FWR offers a significantly broader range of combination of aerodynamic lift and power efficiency with optional kinematics of wing motion. The study results in this chapter provide a quantified guidance for engineering design of MAVs using the three types of wings. The optimal kinematics of wing motions identified in this study provides guidance for MAV design to improve the flight performances subject to various aerodynamic force or efficiency requirements.

7 ANALYSIS AND EXPERIMENT OF A FLYABLE FWR MODEL

The numerical modelling results of FWR in the previous chapters have shown that it has great potential for improving the aerodynamic performances when applied for MAV design. In this chapter, the investigation is then continued into the design, analysis, manufacture and experiment of a flyable micro FWR MAV test model. The developed FWR model is driven by a micro electric motor and using carbon/epoxy composite to build most of the components, the total weight of the FWR test model is achieved to be only 2.6gm.

In this experiment, a desirable FWR wing structure was realised after a series of design and experiment to achieve the desired large pitch angle in the up-stroke for the FWR test model. Due to the extremely light weight of FWR model, the wing structure is highly flexible. Therefore, aeroelastic effects play a significantly role for aerodynamic force production. The aeroelastic twist angle of the wing under the inertia and aerodynamic forces is measured using high speed camera. An algorithm is developed to analysis the instantaneous kinematics of the wing using the frames captured by high speed camera.

The aerodynamic analysis was carried out using CFD method together with the quasi-steady aerodynamic model which employs empirical coefficients to accounts for unsteady aerodynamic effects. The comparison of the analytical and experimental results shows excellent agreement. Detailed analyses based on the simulated flow field on the wing and the aerodynamic forces productions are also presented.

7.1 The FWR Model Design and Manufacture

The FWR model configuration is designed as shown in Figure 7-1 (a). A DC motor is mounted on the body frame made of carbon/epoxy beams. The rotational output of the motor is transformed into an up and down motion of a shaft through a crank-linkage mechanism. The top end of the shaft is connected through a bearing to a horizontal elastic plate. The pair of wing leading edge beam is connected at the root to each end of the elastic plate and supported by

a *U*-frame through ball joints. The wings were set at a fixed initial geometric angle of attack (AoA=15°). The three components (wing beam, *U*-frame and elastic plate) form an elastic lever mechanism that transmits the vertical action of the shaft to a flapping motion of the wings. The mechanism is able to rotate freely around the shaft together with the wings. Based on the design, a physical FWR model was built as shown in Figure 7-1 (b).

(a)   (b)
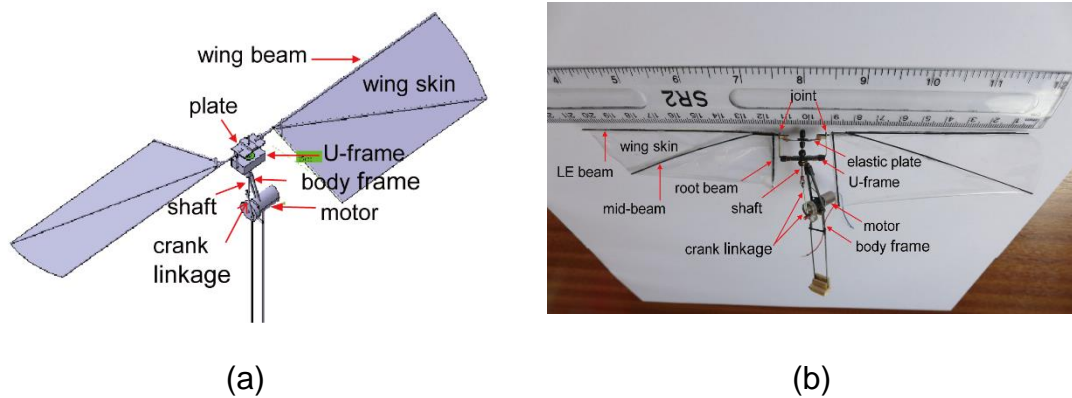
Figure 7-1 (a) FWR configuration and main components; (b) physical model.

The dimensions and weight of the primary components of the FWR model are listed in Table 7-1. Further details of the wing configuration are shown in Figure 7-2.

Table 7-1 Dimensions and weight of the FWR model primary components.

FWR component	Wing	Body frame	Motor	Crank linkage	Others
Dimension (mm)	105x33 (single)	75 x 14 x 7	15x6 (radius)	21	-
Weight (g)	0.28 (two)	0.85	1.2	0.25	0.02
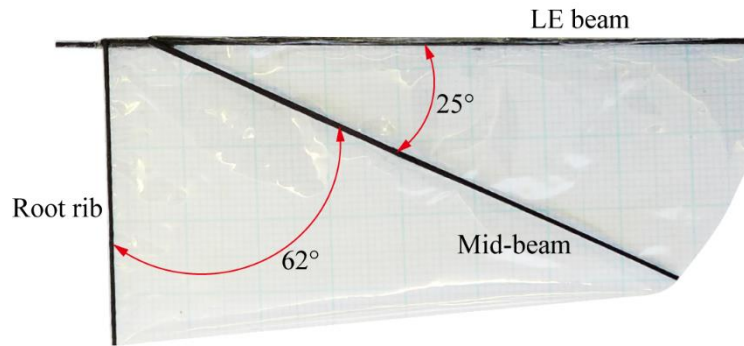
Figure 7-2 FWR model wing structure layout.

The commercially available motor (ZWPD006006-700) integrated with a gear box was selected. Its standard operational rotation speed is 1200 rpm with input voltage 3V and current 25mA, but varies in a range of 500~1500 rpm with input voltage 1.5~4.5V. In the experiment, the required electric power was supplied from a DC power unit.

In the design and manufacturing of the FWR model, the key challenge is for the wing to achieve an optimal kinematics of motion with a sufficient large α_u (AoA in up-stroke) and small α_d (AoA in down-stroke). Since the actuated motion is in vertical direction only, the AoA of a flapping cycle varies in a passive manner that relies on the flexibility of the lever mechanism and the wing structure. Therefore, the elastic plate plays a key role of the flapping mechanism. It not only amplifies the wing flapping angle, but also allows a large twist of the wing due to aeroelastic effect during flapping motion.

In order to make the crank in line with the actuation shaft, the motor was mounted in a position where its Centre of Gravity (CG) is eccentric from the FWR centre line as shown in Figure 7-1. This arrangement results in the CG of the FWR model having 3.5mm distance from the FWR centre in z-direction.

7.2 The FWR Model Experiment

7.2.1 FWR model setup and experiment results

The FWR model was mounted on a load cell (SINOSERA, CL-YB-8/5N in accuracy ±0.2%) to measure the instantaneous dynamic force in transverse direction; the force from the load cell was transmitted to a signal amplifier at a sampling rate of 3000Hz; the FWR kinematics of motion was captured using a high speed camera at a data rate of 1000 frame/s as illustrated in Figure 7-3 (a). The two types of data were transmitted simultaneously and recorded in the PC. The experiment setup is shown in Figure 7-3 (b).

The kinematics of motion of the FWR model was obtained by post-processing the images captured using the high speed camera. The flapping frequency f and rotational speed n is determined by counting the number of frames over 10 flapping cycles Nf and rotational circles Nn as: $f=(10\times1000)/Nf$ and $n=(10\times1000)/Nn$.
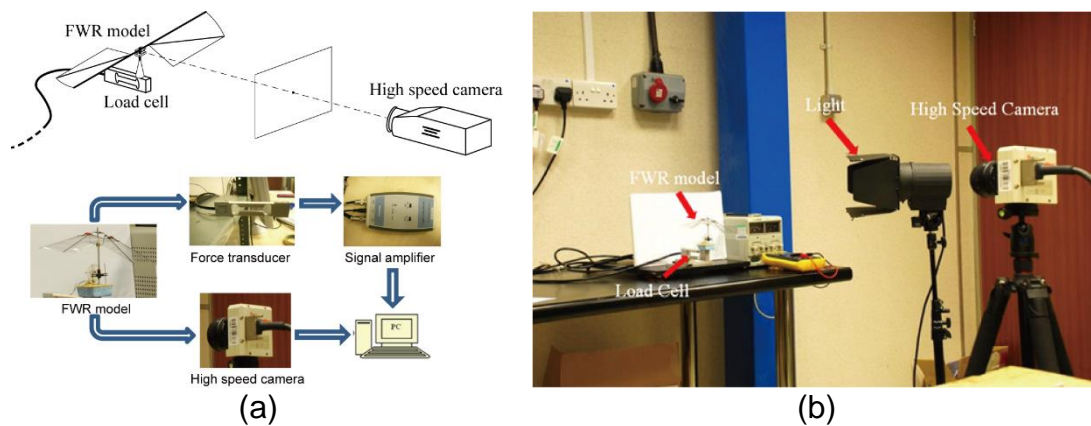
Figure 7-3 (a) The FWR measurement devices and (b) experiment setup.

A series of FWR experiments was performed in a range of input voltages 2.5~4.5v with each measurement time lasting 10s. The instantaneous aerodynamic force was obtained by removing the symmetric periodic inertia force from the measured force data. The resulting FWR flapping frequency, maximum flapping angle (flapping amplitude), AoA, rotation speed and average aerodynamic lift were measured and summarised in Table 7-2 and as shown

Figure 7-4 (a). In addition, the ratio of output lift to input power as a measure of the power efficiency and the Strouhal number (*St*) is calculated and presented in Table 7-2 and Figure 7-4 (b).

Table 7-2 The FWR model results from input voltage in the range of 2.5~4.5v.

Input voltage	(v)	2.50	3.0	3.50	4.0	4.5
Input power	P(W)	0.13	0.18	0.23	0.28	0.34
Max flapping angle	ϕ (deg.)	35.0	39.0	36.0	41.0	35.0
AoA in mid-up-stroke	α_u (deg.)	38.0	40.0	39.0	40.0	41.0
AoA in mid-down-stroke	α_d (deg.)	7.00	-4.0	-10.0	-18.0	-22.0
Flapping frequency	f (Hz)	11.42	14.01	19.31	21.79	24.10
Rotation speed	n(r/s)	2.78	4.57	6.21	7.81	8.93
Average lift	L(mN)	11.7	17.4	24.0	27.2	29.7
Mean lift coefficient	$\bar{C}_L$	1.26	1.00	0.86	0.59	0.72
Strouhal number	St	0.39	0.32	0.31	0.31	0.26

It is noted from the experimental results that the FWR flapping frequency, rotation speed and average lift increase almost linearly with the input power (2.5v~4.5v). During the flapping motion, the wing AoA varies passively around the initial geometric AoA=15° as a result of the aeroelastic interaction between the wing elastic, inertia and aerodynamic forces. When the input voltage increased from 2.5v~4.5v, the up-stroke α_u increased from 38° to 41° corresponding to an aeroelastic twist angle of 23°~26° (15°+23°=38° to 15°+26°=41°). In the down-stroke, the variation and magnitude of the aerodynamic force and (negative) pitching moment are significantly greater than the up-stroke. The pitching moment produced a large variation of (negative) aeroelastic twist angle from -8° to -37° that resulted in the α_d varied from 15°-8°=7° to 15°-37°=-22° for the input 2.5v~4.5v.

| (a) | (b) |
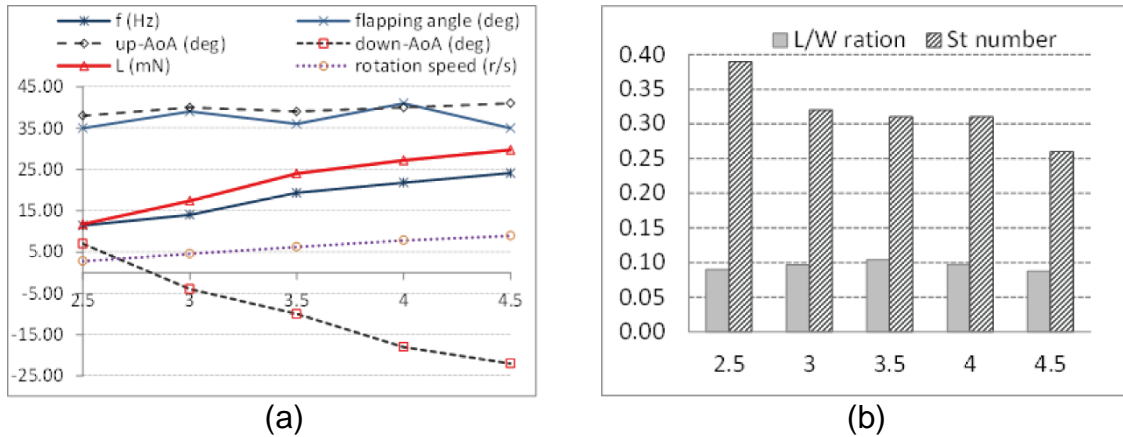
Figure 7-4 (a) The resulting FWR model flapping frequency, angle, geometric AoAs, mean lift and rotation speed; (b) lift to power ratio and *St* for input voltage 2.5~4.5v.

The kinematics of motion (α_u=41°, α_d=-22°) at the maximum input 4.5v is close to the optimal solution (α_u=42°, α_d=-24°) of maximum aerodynamic efficiency of a generic FWR (Li et al., 2016). It is also interesting to note that the *St* of the FWR falls in the range of optimal propelling efficiency 0.25~0.4 as demonstrated by flying animals (Taylor, Nudds and Thomas, 2003) over the input power range as shown in Table 7-2 and Figure 7-4 (b). Although the *St* in Table 7-2 are calculated at the wingtip, they remain the same for any section of the FWR.

Unlike the aerodynamic force, the mean lift coefficient of the FWR does not vary progressively with the input power. Although the lowest input 2.5v resulted in the highest $\bar{C}_L$=1.26 for the FWR model, the passive kinematics of motion (α_u=38°, α_d=7°) is not close to the optimal solution shown in previous study (α_u=18°, α_d=-3° (Li et al., 2016)). The results indicate that an optimal FWR kinematics of motion for maximum $\bar{C}_L$ requires a prescribed actuation rather than achieved by passive twist.

From Figure 7-4 (b), it is noted that the power efficiency reached the maximum for the motor in optimal operation power (3.5v). The resulting lift force L=24mN is only 2mN smaller than the required value to lift up the FWR model. This case is thus taken for further detailed study.

128

7.2.2 FWR kinematic processing

In order to measure the kinematics of motion of the model in this particular case (3.5v), the FWR images were captured at a series of discrete instantaneous moment for post processing as shown in Figure 7-5. The maximum flapping angle and AoA at the mid-up-stroke and mid-down-stroke was obtained from processing the measured data as shown in Figure 7-6. An algorithm based on Euler angles for post processing the wing instantaneous kinematics is developed. Details of the algorithm are provided in Appendix B.
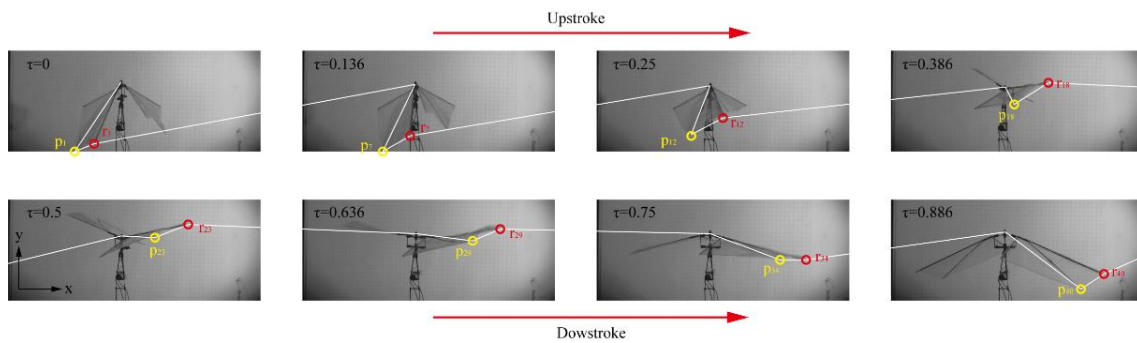
Figure 7-5 FWR image processing for 3.5v input voltage.
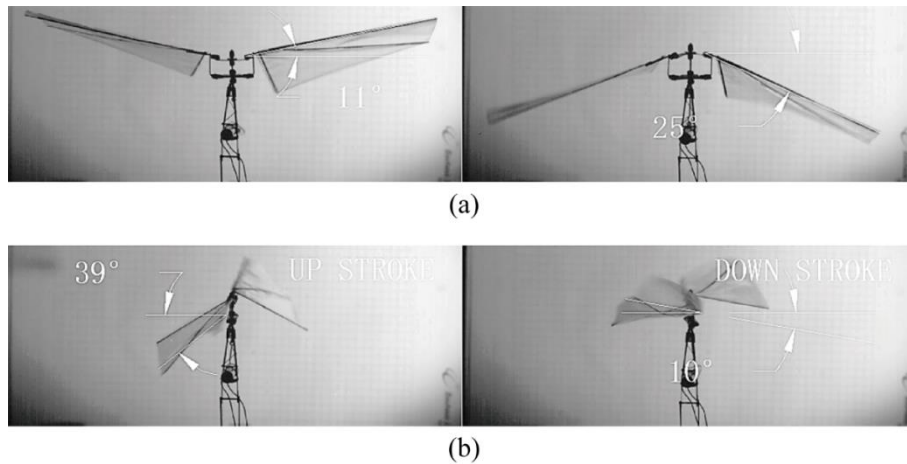
Figure 7-6 (a) Flapping angle at up most and lowest position; (b) AoA at mid-up-stroke (α_u) and mid-down-stroke (α_d) for input 3.5v.
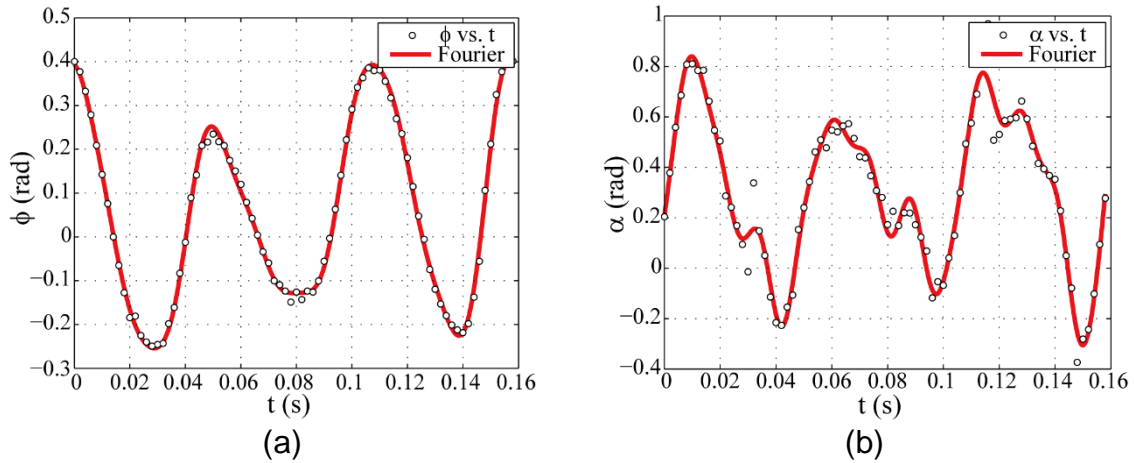
Figure 7-7 Curve fitting of the measured (a) flapping angle; (b) AoA for 3.5v case. White dots indicate measured kinematic data; red line indicates fitted function using Fourier series.

Table 7-3 Coefficients of Fourier fitting for measured data flapping angle (φ) and AoA (α).

Coefficients	Flapping angle (φ)	AoA (α)
a0	0.1671	0.4885
a1	0.0605	-0.0512
b1	-0.0573	-0.0405
a2	0.0624	0.1660
b2	-0.0431	0.2510
a3	0.1082	-0.0287
b3	-0.2312	-0.0350
a4	0.0431	0.0402
b4	0.1364	-0.0095
a5	0.0291	0.0023
b5	0.0686	-0.0041
a6	0.0171	-0.0042
b6	0.0361	-0.0744
a7	-0.0033	0.0001
b7	-0.0233	-0.0031
a8	0.0085	-0.0625
b8	-0.0082	-0.0224

The FWR kinematics of motion was created by curve fitting the measured data (3.5v case) over a couple of flapping cycles using a 8th order Fourier trigonometric series (the coefficients are shown in Table 7-3). The processed FWR flapping angle and AoA results are shown in Figure 7-7. The velocities

and accelerations of the wing motion were obtained by differentiating the displacement function in time.

7.3 The FWR Model Theoretical, CFD and Experimental Results

7.3.1 Comparison of theoretical, CFD and experimental results

According to the function created from the measured FWR kinematics of motion, the aerodynamic forces were calculated using CFD method and the QS aerodynamic model. The CFD simulation in the present study was carried out by solving the 3D incompressible unsteady Navier–Stokes equations of the flapping wing in assumed laminar flow. Details of the flow solver and the validation of our code can be found in the previous work (Jianghao, Chao and Yanlai, 2017). Grid-independence of CFD simulations are performed with the grid node quantities $67 \times 81 \times 78$ (in normal, chordwise, and spanwise directions, respectively); the outer boundary is located 30 chords away from the wing surface and 15 chords away from the wing tip; 400 time steps per flapping cycle is used in the simulation.

In the CFD and QS models, the aeroelastic effect of the FWR wing has been partly taken into account by using the instantaneous AoA measured during the experiments as shown in Figure 7-6 and Figure 7-7. The data is influenced by the wing twist deformation although the effect of wing shape change, i.e. spanwise bending and chordwise camber deformation has been ignored. The data provide reasonably good approximations since a previous study shows that the wing shape change effect would not cause significant change of aerodynamic forces <10% (Young et al., 2009).

Corresponding to the input 3.5v, the FWR motion was measured in terms of flapping angle φ and AoA. According to the motion, the lift and drag coefficients were calculated using the two methods and shown over six flapping cycles in Figure 7-8. The positive φ indicates the wing flapping position below the horizontal plane; negative value above the plane.
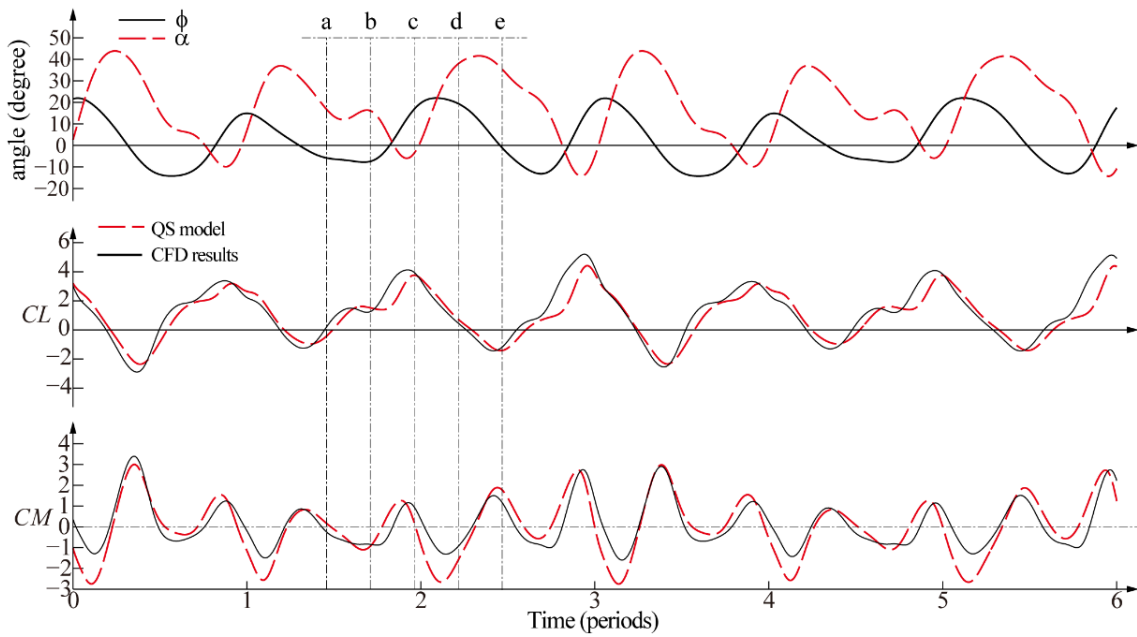
Figure 7-8 The FWR kinematics of motion, C_L and C_M using CFD and QS methods for 3.5v.

As shown in Figure 7-8, the instantaneous C_L and C_M from both methods show good agreement. Based on the results, the average aerodynamic forces and mean lift coefficients over the six flapping cycles were calculated and compared with the experimental results as shown in Table 7-4 and Figure 7-9. In Figure 7-9, the error bands at each input voltage are obtained by choosing the maximum and minimum measured mean lift of different flapping cycles within the interval of measurements (10s in total).

Table 7-4 Comparison of analytical and experimental results.

Input voltage (v)	2.5	3.0	3.5	4.0	4.5
Measured Lift (mN)	11.4	17.4	24.0	27.2	29.7
QS-Method Lift (mN)	9.6	17.2	24.8	28.3	32.0
Experimental $\bar{C}_L$	1.33	1.35	0.98	0.87	0.78
QS-Method $\bar{C}_L$	1.12	1.33	1.01	0.90	0.84
CFD Lift (mN)	-	-	29.8	-	-
CFD $\bar{C}_L$	-	-	1.21	-	-
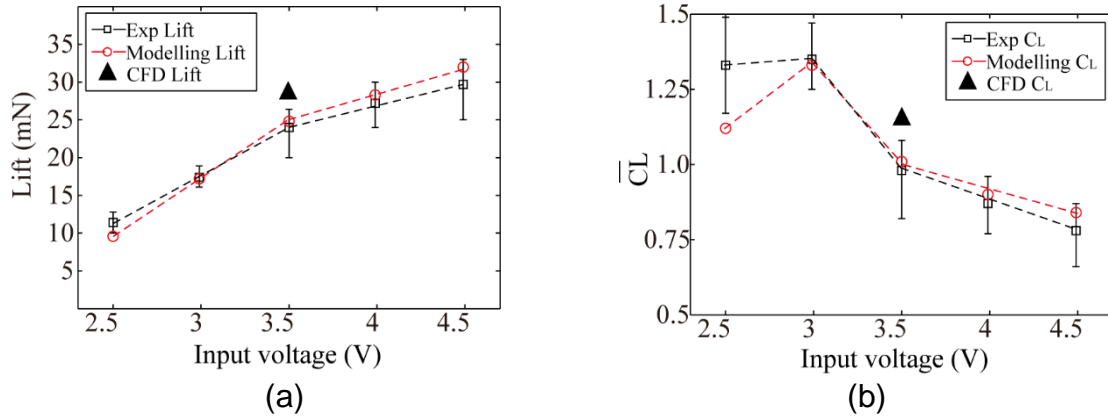
Figure 7-9 (a) The FWR average lift and (b) mean C_L from experiment and QS method for the range of input voltages 2.5V~4.5v

The results comparison shows that the mean lift coefficients and resulting forces for the input voltage 3.5v obtained by CFD method were higher than experimental results. The difference between measured and simulated lift coefficients and forces is less than 3.4% when the input power is in the designed motor operation range around 3~3.5v. For the input voltages 4v~4.5v beyond the range, the difference is increased to 7.7%. When the motor was under-performed for low power input 2.5v however, the simulated lift was lower with a deviation of 15.8%. This is mainly because the FWR AoA became significantly irregular due to the aeroelastic deformation of the wing particularly in the up-down stroke transition period near the maximum up flapping angle. This resulted in an increasing deviation for the curve-fitting and approximated function of the FWR kinematics of motion as shown in Figure 7-10. For more accurate analytical result, the curve-fitting process should be improved.
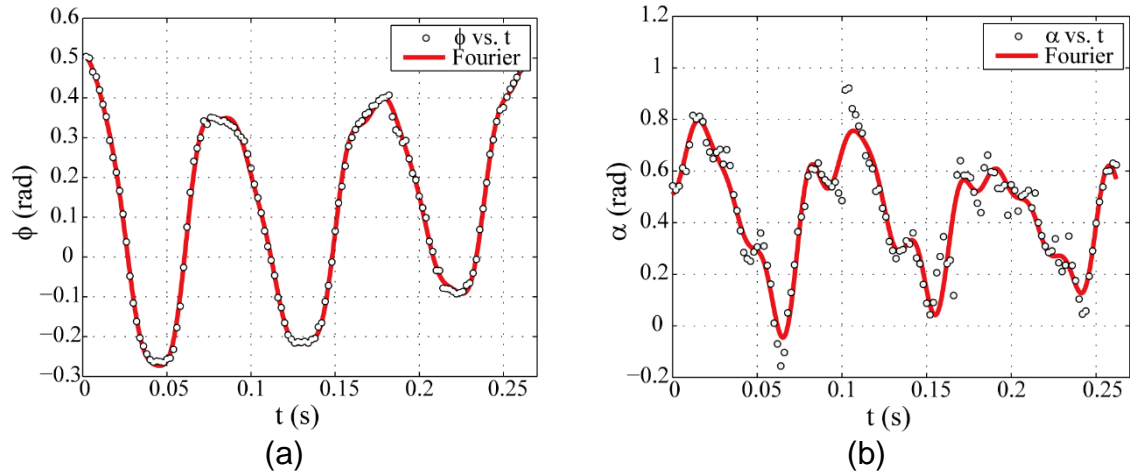
Figure 7-10 Curve fitting of the measured (a) flapping angle; (b) AoA for input 2.5v.

7.3.2 Analysis of CFD results

In order to further study the aerodynamic details, the flow field obtained by the CFD method at five moments of time (from *a* to *e*) over one of the flapping cycles as marked in Figure 7-8 are selected and presented in Figure 7-11. For this selected cycle, the maximum flapping angle φ=31° (lower φ=22°, upper φ=-9°) and wingtip displacement d=57mm. At the flapping frequency 19.3Hz, the average flapping velocity at wingtip is U=2fd=2.2m/s. In the same time, the FWR rotation produced a forward (horizontal) velocity V=3.9m/s (wingtip). The FWR motion changes the instantaneous effective AoA of the wing. The effect of the deflected velocity can be studied qualitatively by the mean deflection angle α_q=tan^{-1}(U/V) =+29.3° in the down-stroke and -29.3° in the up-stroke, which remains the same along the wing span (ignoring the chord-wise deformation). In this study, the flapping cycle is divided into four quarters period. The 1st and 2nd quarters correspond to the upper-half of the up-stroke and down-stroke respectively when the wing is above the horizontal (x-z) plane (y>0, φ<0). The time-a and time-b as shown in Figure 7-8 lie in the middle of their two respective quarters. The 3rd and 4th quarters correspond to the lower half of the down-stroke and up-stroke including time-c and time-d respectively when the wing is below the x-z plane (y<0, φ>0). The time-e is at the end of the 4th quarter cycle.
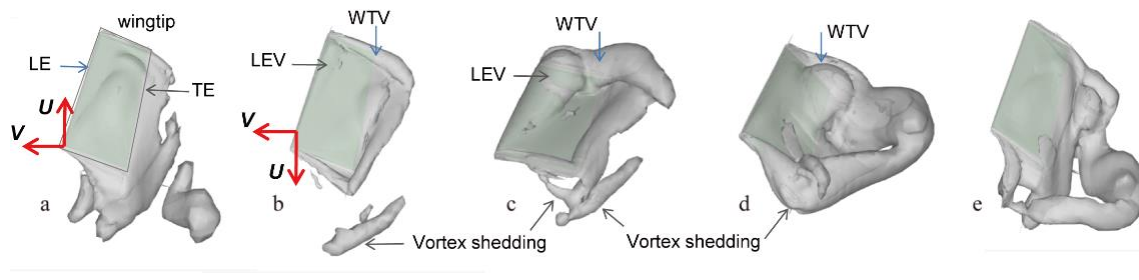
Figure 7-11 The flow field simulation by CFD at five time moments over a flapping cycle.

At time-a, the wing was near the end of up-stroke (mid of the 1st quarter cycle) with geometric AoA $\alpha_u=17°$ as shown in Figure 7-8. The combined α_u and quasi-steady $\alpha_q=-29.3°$ resulted in an equivalent $\alpha_e=\alpha_u+\alpha_q=17°-29.3°=-12.3°$ of the FWR against the airflow. At this moment, the wing LE and upper surface is relatively clean, but the vortex was generated over the lower surface and shed off the TE as shown in Figure 7-11 (a). Under this flow condition, the FWR produced a small lift coefficient $C_L=0.15$ and rotational moment coefficient $C_M=-0.25$ as shown in Figure 7-8.

At time-b, the FWR wing was near the beginning of the down-stroke (mid of the 2nd quarter cycle). Although the wing has completed the transition from up-stroke to down-stroke, the geometric AoA $\alpha_d=17°$ was kept almost the same as time-a, and the resulting equivalent $\alpha_e=\alpha_d+\alpha_q=17°+29.3°=46.3°$ became much greater. Consequently a wingtip vortex and LEV was generated from the outboard wing. The vortex below the wing generated in earlier time-a was partly captured, and partly shed off the TE as shown in Figure 7-11 (b). In this flow and AoA condition, the FWR produced a relatively large $C_L=1.5$, but negative $C_M=-0.9$ as shown in Figure 7-8.

At time-c, the wing moved into the 2nd half of down-stroke in the mid of the 3rd quarter cycle with geometric AoA=-5° as shown in Figure 7-8. The resulting equivalent angle was largely decreased from earlier time-b value, but remained a large value $\alpha_e=\alpha_u+\alpha_q=-5°+29.3°=24.3°$. Consequently the connected LEV and

135

WTV kept growing and maintaining attached to the LE as shown in Figure 7-11 (c). The strong LEV and large α_e led the lift coefficient to nearly the maximum value C_L=4.0. Due to the large C_L and negative AoA=-5°, the resulting C_M also reached nearly the maximum positive C_M=1.0 in this cycle.

At time-d, the wing completed the transition from down-stroke to the first half of up-stroke in the mid of 4th quarter cycle. Due to significant aeroelastic effect in accelerating motion, the geometric AoA increased to 39° towards the maximum value of the cycle as shown in Figure 7-8. The equivalent AoA became $\alpha_e=\alpha_u+\alpha_q$=39°-29.3°=9.7°. The resulting LEV generated at earlier time-c moved down stream and shed off the TE as shown in Figure 7-11 (d). Due to the large AoA but reduced LEV, the resulting C_L=0.5 was reduced from previous value and the C_M=-0.9 became negative.

At time-e, the wing moved to the middle of the up-stroke where the flapping velocity was close to maximum with the AoA=35° reduced from the earlier peak angle 42° as shown in Figure 7-8. This resulted in an equivalent $\alpha_e=\alpha_u+\alpha_q$=35°-29.3°=5.7°. Similar to the time-a, the clean upper surface and vortex below the wing surface resulted in a negative C_L=-1.2. Due to the negative C_L and large AoA=35° however, a positive C_M=1.2 was produced just before completing the flapping cycle as shown in Figure 7-8.

7.3.3 The FWR model flight test

Based on the above results, it was predicted that the FWR can produce sufficient lift force to overcome the model weight (2.6g) for the input power below 0.28W (4v). The FWR model was then removed from the load cell and set on a base rail by placing its long legs into a couple of holes as shown in Figure 7-12 (a). The electric power was supplied to the motor through fine wires, which were kept loosely connected to the FWR motor to ensure little interference with the flying model during flight. When the power of 0.26W (about 3.8v) was supplied, the FWR model achieved a successful vertical take-off as shown in Figure 7-12 (b). The measured FWR flapping frequency, rotation speed and St are 21Hz, 7.2r/s and 0.31 respectively. The flyable model demonstrated its self-stabilized flight without control, which is one of the FWR

136

features. By tuning the input power, the FWR model also demonstrated its capability of hovering within a small highlighted space as shown in the Figure 7-13.

(a)   (b)
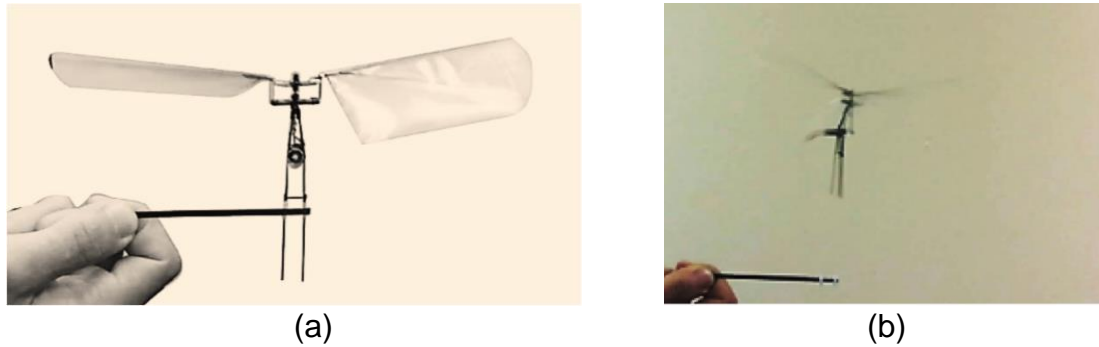
Figure 7-12 The FWR model (a) set on a flight launch base (b) vertical take-off.
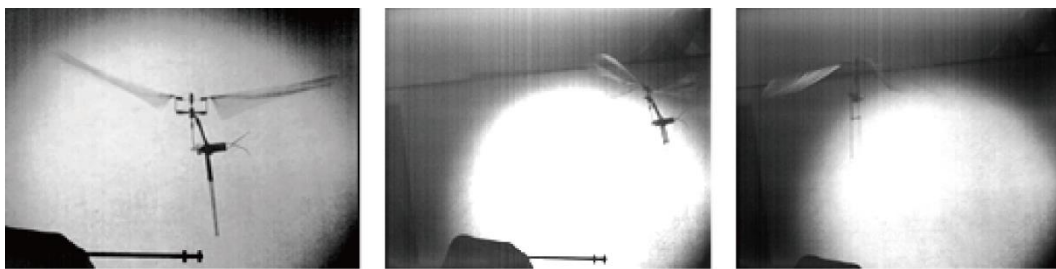
Figure 7-13 The FWR model hovering within a small highlighted space.

In theory, the FWR is statically stable in the horizontal plane and free of body rotation about the vertical axis. This is because no actuation torque is required for the self-propelling wing rotation as one of the FWR key features. In the experiment, however, the FWR model body was swinging and spinning (rotating about the respective z and y axes, coordinate system as defined in Figure 4-1) although at very low frequency as observed during the flight test. Throughout the flight test, the fine wires are loosely connected to the motor to prevent external interference to the FWR model movement. The main reason for the model swing is because of the torque about the horizontal z-axis produced by the motor instead of a desirable torque-free linear motor. The body spin is due to the existing friction in the bearings. The additional rotational mass moment of

inertia due to the eccentric CG of the FWR model reduces the body spinning frequency.

7.4 Summary

In this chapter, the design, experiment and numerical analysis of a practical FWR MAV are presented. A successful VTOL and short hovering flight test of the model has been performed.

Systematic numerical analysis and experimental study has been carried out based on the developed model. Comparison of numerical modelling results using QS aerodynamic model and experimental data show that the mean aerodynamic lift coefficients and average forces by the numerical method have excellent agreement with the experimental results (<3.4% difference) within the range of power for the motor specified normal operation (3~3.5V).

In this experiment, it is also observed that the resulting kinematics of wing motion of the FWR as a result of aeroelastic twisting lead to the optimal propelling efficiency in terms of St=0.25~0.4 for the whole range of input power (0.25~4.5v). This self-adapted behaviour of FWR is in agreement with the previous numerical study, as presented in chapter 5, which implies that the natural equilibrium of FWR lead to high aerodynamic efficiency.

It is noted that the elastic plate of the developed model plays a key role in the lever mechanism of the FWR. It not only amplifies the flapping angle, but also produces elastic twist angle for the FWR to obtain desirable wing kinematics which improves the aerodynamic efficiency.

In summary, the flyable FWR model provides a desirable base not only for analytical and experimental study, but also a flight demonstrator of the FWR feasibility and advantages.

8 CONCLUSIONS AND FUTURE WORK

8.1 Conclusions

In this thesis, a series of studies on the structure, aerodynamics and aeroelasticity of large fixed wing aircraft as well as MAVs are presented. The structural and aeroelastic design, analysis and optimization techniques for conventional fixed wing aircraft are firstly investigated. The aerodynamics of flapping wings at low Re and aeroelasticity of MAVs are then investigated using numerical and experimental methods.

For conventional fixed wing aircraft, a method of aeroelastic optimization based on the existing commercial software MATLAB and NASTRAN has been developed. A case study of composite wing has been used to demonstrate the FE modelling, analysis and optimization using the developed MATLAB-NASTRAN optimization platform. The results show that the wing box weight can be reduced by 13% with the skin thickness and stringer/stiffener cross section dimensions being taken as design variables. When the composite skin laminate layup is taken as design variables for aeroelastic tailoring, the flutter speed can be increased by 18.5%. The study further revealed that the most sensitive part of the wing for aeroelastic tailoring is near the engine location, which contributes to the majority of flutter speed increase for optimization.

A 2D analytical model for non-circular BWB fuselage skin design has been developed and validated against FEM. The developed model is then interfaced with an optimizer in MATLAB to carry out a case study of a fuselage cross section taken from a BWB aircraft. The results show that a weight reduction of 17% can be achieved. These studies demonstrate the effective procedure and efficient techniques of interfacing numerical models with commercial software packages such as NASTRAN and MATLAB for design, analysis and optimization of aircraft structure and aeroelasticity.

In order to model the unsteady aerodynamic force of flapping wings at low Re, a QS aerodynamic model has been developed. Compared with the CFD method, the modelled instantaneous forces by the QS model achieved very good

agreement both qualitatively and quantitatively. The modelled average aerodynamic forces of QS model are also within 15% difference in comparison with CFD method.

Based on the QS model, the aerodynamic efficiency for flapping wing flight at low Re (2500) is studied. The results show that the propulsive efficiency and efficiency of lift for flapping wings peak at a Strouhal number St lying between 0.1 and 0.5. The natural equilibrium state of FWR also lies in this interval of St, which is in close agreement with observations from animal flight. Further investigations show that the aerodynamic efficiency of the FWR at equilibrium state is above 85% of maximum efficiency, indicating that the passive rotation of FWR automatically converges to high efficiency states.

The study then continues to identify the optimal wing kinematics of FWR in terms of lift production and aerodynamic efficiency. A series of calculations using the QS aerodynamic model is carried out. The lift production and aerodynamic efficiency of conventional rotary wing and insect-like flapping wings are also calculated at equivalent low Re (3500) and wing geometry. The optimal kinematics of FWR wing for producing lift and aerodynamic efficiency are found to appear at relatively small AoA, with α_d between -30°~-2° and α_u between 13°~50°. Comparisons are made among the FWR, rotary wing and insect-like flapping wings. The results show that the FWR can produce significantly greater aerodynamic lift coefficient with power efficiency between the other two types of wings. The rotary wing has the greatest power efficiency of 28% and 39% higher than the FWR and insect-like wing (HF) respectively. However the corresponding lift coefficient of the rotary wing is only 30% and 53% of the other two types of wings. The results of this study provide guidance for engineering design of MAVs under specific design requirements.

Based on the numerical analysis results, a FWR experiment is then carried out using a developed model of weight only 2.6g. Ground tests of the model using load cell and high speed camera to measure the aerodynamic lift production and wing kinematics are performed. The wing instantaneous AoA as a result of aeroelastic twist are calculated using a developed algorithm from the frames

captured by the high speed camera. Based on the measured wing kinematics, numerical calculations are carried out which in comparison with the measured lift are in very good agreement (<3.4% difference). Analysis of the simulated flow field of the wing show that the desirable variations of the wing AoA as a result of aeroelastic twist leads to cyclic formation and shedding of vortices on the wing. In particular, a stably attached LEV structure is found for the wing in the downstroke of the flapping motion, which serves to maintain the high lift production. The study revealed that aeroelastic twisting of the wing help to form desirable variations of wing angle of attack, which improves the aerodynamic performance of FWR.

The study results of this thesis provide advancement in the understanding of aerodynamics and aeroelasticity of flapping wing flight at low Re, and also provide guidance for engineering practices of bio-inspired MAVs. The methods developed in this thesis for structural, aerodynamic and aeroelastic analysis can be further applied to engineering design, analysis and optimization of large aircrafts as well as bio-inspired MAVs.

8.2 Suggestions for Future Work

This thesis presents a number of fundamental investigations towards the development of MAVs. In particular, the aerodynamic force, efficiency and aeroelasticity of flapping wing MAVs at low Re have been addressed.

In the aeroelastic investigation of flapping wing, the wing twist effect on the AoA of the wing has been taken into account. Further studies can be made into the effect of more detailed wing deformation (e.g. wing bending and shape change) on the aerodynamic performance of the wing.

In order to achieve autonomous flight of the FWR MAV, further studies into the flight dynamics and control of the multibody system is required. Mechatronic integration of hardware control circuits and software are needed for implementation of the FWR MAV.

REFERENCES

Al-Qadi, I.M. and Al-Bahi, A.M. (2006) 'Micro aerial vehicles design challenges: state of the art review', *SSAS UAV Scientific Meeting & Exhibition.*, pp. 29–45.

Alben, S. (2008) 'Optimal flexibility of a flapping appendage in an inviscid fluid', *Journal of Fluid Mechanics*, 614, pp. 355–380.

Anderson, J.M., Streitlien, K., Barrett, D.S. and Triantafyllou, M.S. (1998) 'Oscillating foils of high propulsive efficiency', *Journal of Fluid Mechanics*, 360, pp. 41–72.

Arasse, D. and da Vinci, L. (1998) *Leonardo Da Vinci*. Old Saybrook: Konecky & Konecky.

Avadhanula, S., Wood, R.J., Campolo, D. and Fearing, R.S. (2002) 'Dynamically tuned design of the MFI thorax', *Proceedings - IEEE International Conference on Robotics and Automation*, 1, pp. 52–59.

Azuma, A., Azuma, S., Watanabe, I. and Furuta, T. (1985) 'Flight mechanics of a dragonfly', *Journal of Experimental Biology*, 116(1), pp. 79–107.

Bachmann, R.J., Boria, F.J., Vaidyanathan, R., Ifju, P.G. and Quinn, R.D. (2009) 'A biologically inspired micro-vehicle capable of aerial and terrestrial locomotion', *Mechanism and Machine Theory*, 44(3), pp. 513–526.

Barbarino, S., Bilgen, O., Ajaj, R.M., Friswell, M.I. and Inman, D.J. (2011) 'A review of morphing aircraft', *Journal of Intelligent Material Systems and Structures*, 22(9), pp. 823–877.

Berg, C. Van Den and Ellington, C.P. (1997a) 'The vortex wake of a "hovering" model hawkmoth', *Philosophical Transactions of the Royal Society B: Biological Sciences*, 352(1351), pp. 317–328.

Berg, C. Van Den and Ellington, C.P. (1997b) 'The three-dimensional leading-edge vortex of a "hovering" model hawkmoth', *Philosophical Transactions of the Royal Society B: Biological Sciences*, 352(1351), pp. 329–340.

Biewener, A.A. (2003) *Animal locomotion*. Oxford: Oxford University Press.

Birch, J.M. and Dickinson, M.H. (2003) 'The influence of wing-wake interactions on the production of aerodynamic forces in flapping flight', *Journal of Experimental Biology*, 206(13), pp. 2257–2272.

Bisplinghoff, R., Ashley, H. and Halfman, R. (1996) *Aeroelasticity*. New York: Dover Publications.

Blake, J.R. and Sleigh, M.A. (1974) 'Mechanics of ciliary locomotion', *Biological Reviews of the Cambridge Philosophical Society*, 49(1), pp. 85–125.

Blake, R.W. (1978) 'The mechanics of labriform locomotion. I. Labriform locomotion in the angelfish (Pterophyllum eimekei): an analysis of the power stroke', *J. Exp. Biol.*, 82, pp. 255–271.

Bohorquez, F., Samuel, P., Sirohi, J., Pines, D., Rudd, L. and Perel, R. (2003) 'Design, analysis and hover performance of a rotary wing micro air vehicle', *Journal of the American Helicopter Society*, 48(2), pp. 80–90.

Bos, F.M., Lentink, D., Oudheusden, B.W. Van and Bijl, H. (2008) 'Influence of wing kinematics on performance in hovering insect flight', *J. Fluid Mech.*, 594, pp. 341–368.

Bouabdallah, S., Becker, M. and Siegwart, R. (2007) 'Autonomous miniature flying robots: coming soon!', *IEEE Robotics & Automation Magazine*, 14(3), pp. 88–98.

Cadou, C., Moulton, N., Aluko, M., Sookdeo, T. and Leach, T. (2003) 'Performance measurement and scaling in small internal combustion engines', *41st Aerospace Sciences Meeting and Exhibit*, (1), pp. 1–11.

Chigier, N. and Gemci, T. (2003) 'A review of micro propulsion technology', *American Institute of Aeronautics and Astronautics*, 670, pp. 1–11.

Datta, A., Chopra, I., Bao, J., Gamard, O., Griffiths, D., Liu, L., Pugliese, G., Roget, B. and Sitamaran, J. (2000) The martian autonomous rotary-wing vehicle (MARV) *Alfred Gessow Rotorcraft Center*. Department of Aerospace

Engineering, University of Maryland, College Park, Maryland

Dickinson, M. and Dudley, R. (2009) 'Flight', in Vincent, R. and Ring, C. (eds.) *Encyclopedia of Insects*. 2nd edn. Academic Press, pp. 364–372.

Dickinson, M.H., Lehmann, F.O. and Sane, S.P. (1999) 'Wing rotation and the aerodynamic basis of insect flight', *Science*, 284(5422), pp. 1954–1960.

Dudley, R. (2002) *The Biomechanics of Insect Flight: Form, Function, Evolution*. Princeton University Press.

Ellington, C.P. (1984a) 'The aerodynamics of hovering insect flight .6. lift and power requirements', *Philosophical Transactions of the Royal Society of London Series B-Biological Sciences*, 305(1122), pp. 145–181.

Ellington, C.P. (1991) 'Aerodynamics and the origin of insect flight', *Advances in Insect Physiology*, 23(C), pp. 171–210.

Ellington, C.P. (1999) 'The novel aerodynamics of insect flight: applications to micro-air vehicles.', *The Journal of experimental biology*, 202(Pt 23), pp. 3439–3448.

Ellington, C.P. (1984b) 'The aerodynamics of hovering insect flight .1. the quasi-steady analysis', *Philosophical Transactions of the Royal Society of London Series B-Biological Sciences*, 305(1122), pp. 1–15.

Ellington, C.P. (1984c) 'The aerodynamics of hovering insect flight .2. morphological parameters', *Philosophical Transactions of the Royal Society of London Series B-Biological Sciences*, 305(1122), pp. 17–40.

Ellington, C.P. (1984d) 'The aerodynamics of hovering insect flight .3. kinematics', *Philosophical Transactions of the Royal Society of London Series B-Biological Sciences*, 305(1122), pp. 41–78.

Ellington, C.P. (1984e) 'The aerodynamics of hovering insect flight .4. aerodynamic mechanisms', *Philosophical Transactions of the Royal Society of London Series B-Biological Sciences*, 305(1122), pp. 79–113.

Ellington, C.P., van den Berg, C., Willmott, A.P. and Thomas, A.L.R. (1996)

'Leading-edge vortices in insect flight', *Nature*, 384(6610), pp. 626–630.

Ennos, A.R. (1988) 'The inertial cause of wing rotation in Diptera', *Journal of experimental biology*, 140(1), pp. 161–169.

Epstein, A.H. and Senturia, S.D. (1997) 'Macro power from micro machinery', *Science*, 276(5316), p. 1211.

Ettinger, S.M., Nechyba, M.C., Ifju, P.G. and Waszak, M. (2003) 'Vision-guided flight stability and control for micro air vehicles', *Advanced Robotics*, 17(7), pp. 617–640.

Fearing, R.S., Chiang, K.H., Dickinson, M.H., Pick, D.L., Sitti, M. and Yan, J. (2000) 'Wing transmission for a micromechanical flying insect', *Proceedings 2000 ICRA. Millennium Conference. IEEE International Conference on Robotics and Automation.*, Vol.2, pp. 1509–1516.

Fu, K., Knobloch, A.J., Martinez, F.C., Walther, D.C., Fernandez-Pello, C., Pisano, A.P., Liepmann, D., Miyaska, K. and Maruta, K. (2001) 'Design and experimental results of small-scale rotary engines', *2001 ASME International Mechanical Engineering Congress and Exposition.*, Vol.2, pp. 3439–3445.

G.C.H.E., de C., Groen, M.A., C., de W., Remes, B., Ruijsink, R. and Van Oudheusden, B.W. (2012) 'Design, aerodynamics and autonomy of the DelFly', *Bioinspiration & Biomimetics*, 7(2), p. 25003.

G.C.H.E., de C., Kristien M.E., de C., Ruijsink, R., Remes, B. and C., de W. (2009) 'Design, Aerodynamics, and Vision-Based Control of the DelFly', *International Journal of Micro Air Vehicles*, 1(2), pp. 71–97.

Galinski, C. and Zbikowski, R. (2005) 'Insect-like flapping wing mechanism based on a double spherical Scotch yoke', *Journal of The Royal Society Interface*, 2(3), pp. 223–235.

Galiński, C. and Żbikowski, R. (2007) 'Some problems of micro air vehicles development', *Bulletin of the Polish Academy of Sciences-Technical Sciences*, 55(1), pp. 91–98.

Guo, S., Li, D. and Huang, Z. (2009) 'A smart material aeroelastic flapping wing micro rotorcraft', *International forum on aeroelasticity and structural dynamics.* Seattle, Washington: Paper no.: IFASD-2009-163.

Guo, S., Li, D. and Wu, J. (2012) 'Theoretical and experimental study of a piezoelectric flapping wing rotor for micro aerial vehicle', *Aerospace Science and Technology*, 23(1), pp. 429–438.

Guo, S., Li, H., Zhou, C., Zhang, Y.L., He, Y. and Wu, J.H. (2018) 'Analysis and experiment of a bio-inspired flyable micro flapping wing rotor', *Aerospace Science and Technology*, 79, pp. 506–517.

Heathcote, S., Martin, D. and Gursul, I. (2004) 'Flexible flapping airfoil propulsion at zero freestream velocity', *AIAA Journal*, 42(11), pp. 2196–2204.

Hodges, D.H. (1990) 'A mixed variational formulation based on exact intrinsic equations for dynamics of moving beams', *International Journal of Solids and Structures*, 26(11), pp. 1253–1273.

Hodges, D.H. (2003) 'Geometrically exact, intrinsic theory for dynamics of curved and twisted anisotropic beams', *AIAA Journal*, 41(6), pp. 1131–1137.

Hodges, D.H. and Pierce, G.A. (2014) *Introduction to Structural Dynamics and Aeroelasticity*. Cambridge: Cambridge University Press.

Hylton, T., Martin, C., Tun, R. and Castelli, V. (2012) 'The DARPA nano air vehicle program', *50th AIAA Aerospace Sciences Meeting including the New Horizons Forum and Aerospace Exposition.*, pp. 1–9.

Ifju, P.G.J. (2005) 'Flexible-wing-based micro air vehicles', in *Compliant Structures in Nature and Engineering.* , pp. 171–191.

Isogai, K., Shinmoto, Y. and Watanabe, Y. (1999) 'Effects of dynamic stall on propulsive efficiency and thrust of flapping airfoil', *AIAA Journal*, 37(10), pp. 1145–1151.

Jianghao, W., Chao, Z. and Yanlai, Z. (2017) 'Aerodynamic power efficiency comparison of various micro-air-vehicle layouts in hovering flight', *AIAA Journal*,

55(4), pp. 1265–1278.

Jones, K.D., Dohring, C.M. and Platzer, M.F. (1998) 'Experimental and computational investigation of the Knoller-Betz effect', *AIAA Journal*, 36(7), pp. 1240–1246.

Katz, J. and Weihs, D. (1978) 'Hydrodynamic propulsion by large amplitude oscillation of an airfoil', *J. Fluid Mech.*, 88, pp. 486–497.

Keennon, M., Klingebiel, K. and Won, H. (2012) 'Development of the Nano Hummingbird: a tailless flapping wing micro air vehicle', *50th AIAA Aerospace Sciences Meeting including the New Horizons Forum and Aerospace Exposition*. Nashville, Tennessee: American Institute of Aeronautics and Astronautics.

Kornbluh, R. (2002) 'Project mentor: biologically inspired platform', *Keynote Presentation at the 8th AIAA/CEAS Aeroacoustics Conference*. Breckenridge, Colorado: American Institute of Aeronautics and Astronautics, Vol.1719.

Kramer, von M. (1932) 'Die zunahme des maximalauftriebes von tragflugeln bei plotzlicher anstellwinkelvergrosserung (boeneffekt)', *Z.Flugtech.Motorluftschiff*, 23, pp. 185–189.

Kristien M.E., D.C., Roeland, de K., Bart, R., Bas W. Van, O. and Hester, B. (2009) 'Aerodynamic experiments on DelFly II: unsteady lift enhancement', *International Journal of Micro Air Vehicles*, 1(4), pp. 255–262.

Kroo, I. and Kunz, P. (2000) 'Development of the Mesicopter: a miniature autonomous rotorcraft', *Vertical Lift Aircraft Design Conference (A00-26651 06-05)*. San Francisco,CA: American Helicopter Society, International, pp. 1–9.

Kroo, I., Prinz, F., Shantz, M. and Kunz, P. (2000) *The Mesicopter: a miniature rotorcraft concept–phase ii interim report*. Stanford University.

Lee, Y.J., Lua, K.B. and Lim, T.T. (2016) 'Aspect ratio effects on revolving wings with Rossby number consideration.', *Bioinspiration & biomimetics*, 11(5), p. 056013.

Lentink, D. (2013) 'Biomimetics: flying like a fly', *Nature*, 498(7454), pp. 306–307.

Lentink, D. and Dickinson, M.H. (2009) 'Rotational accelerations stabilize leading edge vortices on revolving fly wings', *Journal of Experimental Biology*, 212(16), pp. 2705–2719.

Lentink, D., Jongerius, S.R. and Bradshaw, N.L. (2010) 'The scalable design of flapping micro-air vehicles inspired by insect flight', in *Flying Insects and Robots*. Springer, pp. 185–205.

Lewin, G.C. and Haj-Hariri, H. (2003) 'Modelling thrust generation of a two-dimensional heaving airfoil in a viscous flow', *Journal of Fluid Mechanics*, 492(492), pp. 339–362.

Li, H., Guo, S., Zhang, Y.L., Zhou, C. and Wu, J.H. (2016) 'Unsteady aerodynamic and optimal kinematic analysis of a micro flapping wing rotor', *Aerospace Science and Technology*, 63, pp. 167–178.

Lian, Y., Shyy, W., Viieru, D. and Zhang, B. (2003) 'Membrane wing aerodynamics for micro air vehicles', *Progress in Aerospace Sciences*, 39(6–7), pp. 425–465.

Liebeck, R.H. (2004) 'Design of the blended wing body subsonic transport', *Journal of Aircraft*, 41(1), pp. 10–25.

Lighthill, J. (1976) 'Flagellar hydrodynamics', *SIAM Review*, 18(2), pp. 161–230.

Lighthill, J. (1997) 'Introduction to the scaling of aerial locomotion', in T. J. Pedley (ed.) *Scale Effects in Animal Locomotion*. New York: Academic Press, pp. 365–404.

Lim, T.T., Teo, C.J., Lua, K.B. and Yeo, K.S. (2009) 'On the prolong attachment of leading edge vortex on a flapping wing', *Modern Physics Letters B*, 23(03), pp. 357–360.

Lin, J.C.M. and Pauley, L.L. (1996) 'Low-Reynolds-number separation on an airfoil', *AIAA Journal*, 34(8), pp. 1570–1577.

Liu, H., Ellington, C.P., Kawachi, K., Berg, C. Van Den and Willmott, A.P. (1998) 'A computational fluid dynamic study of hawkmoth hovering', *The Journal of experimental biology*, 201, pp. 461–477.

Livne, E. (2003) 'Future of airplane aeroelasticity', *Journal of Aircraft*, 40(6), pp. 1066–1092.

Livne, E. and Weisshaar, T.A. (2003) 'Aeroelasticity of nonconventional airplane configurations-past and future', *Journal of Aircraft*, 40(6), pp. 1047–1065.

Love, M., Zink, P., Wieselmann, P. and Youngren, H. (2005) 'Body freedom flutter of high aspect ratio flying wings', *46th AIAA/ASME/ASCE/AHS/ASC Structures, Structural Dynamics and Materials Conference*. American Institute of Aeronautics and Astronautics, pp. 1–23.

Ma, K.Y., Chirarattananon, P., Fuller, S.B. and Wood, R.J. (2013) 'Controlled flight of a biologically inspired, insect-scale robot', *Science*, 340(6132), pp. 603–607.

Magnan, A. (1934) *Le vol des insectes*. Hermann, Locomotion chez les animaux.

Mao, S. and Hamdani, H. (2001) 'A study on the mechanism of high-lift generation by an airfoil in unsteady motion at low reynolds number', *Acta Mechanica Sinica*, 17(2), pp. 97–114.

McHenry, M.J. (2003) 'The hydrodynamics of locomotion at intermediate Reynolds numbers: undulatory swimming in ascidian larvae (Botrylloides sp.)', *Journal of Experimental Biology*, 206(2), pp. 327–343.

McMasters, J.. and Henderson, M.. (1979) 'Low speed single element airfoil synthesis', *Technical Soaring*, 6(2), p. 7.

Mcmichael, J.M. and Francis, M.S. (1997) 'Micro air vehicles - toward a new dimension in flight', *Unmanned Systems*, 15(3), pp. 10–15.

Moore, M.N.J. (2015) 'Torsional spring is the optimal flexibility arrangement for thrust production of a flapping wing', *Physics of Fluids*, 27(9)

Morris, S.J. (1997) 'Design and flight test results for micro-sized fixed-wing and VTOL aircraft', *Proceedings of the First International Conference on Emerging Technologies for Micro Ai Vehicles*. Atlanta, GA: Georgia Institute of Technology.

Mountcastle, A.M. and Combes, S.A. (2013) 'Wing flexibility enhances load-lifting capacity in bumblebees', *Proceedings of the Royal Society B: Biological Sciences*, 280(1759), p. 20130531.

Mountcastle, A.M. and Daniel, T.L. (2010) 'Aerodynamic and functional consequences of wing compliance', *Animal Locomotion*, , pp. 311–320.

Mueller, T.J. (1999) 'Aerodynamic measurements at low reynolds numbers for fixed wing MAVs', *Development and Operations of UAVs for Military and Civil Applications*. Belgium, pp. 1–32.

Mukhopadhyay, V. (2005) 'Blended Wing Body (BWB) fuselage structural design for weight reduction', *46th AIAA/ASME/ASCE/AHS/ASC Structures, Structural Dynamics and Materials Conference.*, pp. 1–8.

Musiak, J.D. and Vogel, S. (1996) *Life in Moving Fluids: The Physical Biology of Flow*. Princeton, New Jersey: Princeton University Press.

Nakata, T. and Liu, H. (2012) 'Aerodynamic performance of a hovering hawkmoth with flexible wings: a computational approach', *Proceedings of the Royal Society B: Biological Sciences*, 279(1729), pp. 722–731.

Norberg, U.M. (2012) *Vertebrate flight: mechanics, physiology, morphology, ecology and evolution*. Springer-Verlag Berlin Heidelberg.

O'Meara, M. and Mueller, T.J. (1987) 'Laminar separation bubble characteristics on an airfoil at low Reynolds numbers', *AIAA Journal*, 25(8), pp. 1033–1041.

Pardesi, M.S. (2005) 'Unmanned aerial vehicles/unmanned combat aerial vehicles: likely missions and challenges for the policy-relevant future', *Air & Space Power Journal*, 19(3), p. 45.

Pauley, L.L., Moin, P. and Reynolds, W.C. (1990) 'The structure of two-

dimensional separation', *Journal of Fluid Mechanics*, 220, pp. 397–411.

Paulsen, D.H. and Muren, P. (2009) 'Nano UAS- an upcoming reality', *Proceedings of the 24th International Unmanned Air Vehicles Conference.* Bristol, UK, pp. 132–132.

Pelletier, A. and Mueller, T.J. (2000) 'Low Reynolds number aerodynamics of low-aspect-ratio, thin/flat/cambered-plate wings', *Journal of Aircraft*, 37(5), pp. 825–832.

Pendleton, E., Lee, M. and Wasserman, L. (1992) 'Application of active flexible wing technology to the Agile Falcon', *Journal of Aircraft*, 29(3), pp. 444–451.

Pennycuick, C.J. (1989) *Bird Flight Performance: A Practical Calculation Manual.* Oxford University Press.

Pennycuick, C.J. (1996) 'Wingbeat frequency of birds in steady cruising flight: new data and improved predictions', *Journal of Experimental Biology*, 199, pp. 1613–1618.

Pérez-Arancibia, N.O., Ma, K.Y., Galloway, K.C., Greenberg, J.D. and Wood, R.J. (2011) 'First controlled vertical flight of a biologically inspired microrobot', *Bioinspiration and Biomimetics*, 6(3), p. 36009.

Petricca, L., Ohlckers, P. and Grinde, C. (2011) 'Micro- and nano-air vehicles: State of the art', *International Journal of Aerospace Engineering*, 2011, p. 17.

Pines, D.J. and Bohorquez, F. (2006) 'Challenges facing future micro-air-vehicle development', *Journal of Aircraft*, 43(2), pp. 290–305.

Pines, D.J., Bohorquez, F.A. and Sirohi, J. (2005) *Biomimetic Mechanism for Micro Aircraft.* United States Patent.

Popescu, B. and Hodges, D.H. (2000) 'On asymptotically correct Timoshenko-like anisotropic beam theory', *International Journal of Solids and Structures*, 37(3), pp. 535–558.

Pornsin-Sirirak, T.N., Lee, S.W., Nassef, H., Grasmeyer, J., Tai, Y.C., Ho, C.M. and Keennon, M. (2000) 'MEMS wing technology for a battery-powered

ornithopter', *Proceedings IEEE Thirteenth Annual International Conference on Micro Electro Mechanical Systems (Cat. No.00CH36308).*, pp. 799–804.

Prempraneerach, P., Hover, F.S. and Triantafyllou, M.S. (2003) 'The effect of chordwise flexibility on the thrust and efficiency of a flapping foil', *Proceedings Unmanned, Untethered Submersible Technology.*, p. 11.

Rayner, J.M. V. (1988) 'Form and function in avian flight', in Johnston, R. (ed.) *Current Ornithology*. Springer, pp. 1–66.

Rayner, J.M. V (1979) 'A new approach to animal flight mechanics', *Journal of Experimental Biology*, 80, pp. 17–54.

Read, D.A., Hover, F.S. and Triantafyllou, M.S. (2003) 'Forces on oscillating foils for propulsion and maneuvering', *Journal of Fluids and Structures*, 17(1), pp. 163–183.

Ricketts, R.H. (1983) *Structural testing for static failure, flutter and other scary things*. NASA Technical Memorandum 84606. NASA Langley Research Center, Hampton, VA.

Sane, S.P. (2003) 'The aerodynamics of insect flight', *Journal of Experimental Biology*, 206(23), pp. 4191–4208.

Sane, S.P. and Dickinson, M.H. (2001) 'The control of flight force by a flapping wing: Lift and drag production', *Journal of Experimental Biology*, 204(15), pp. 2607–2626.

Sane, S.P. and Dickinson, M.H. (2002) 'The aerodynamic effects of wing rotation and a revised quasi-steady model of flapping flight', *Journal of Experimental Biology*, 205(8), pp. 1087–1096.

Schafroth, D., Bouabdallah, S., Bermes, C. and Siegwart, R. (2009) 'From the test benches to the first prototype of the muFly micro helicopter', *Journal of Intelligent and Robotic Systems: Theory and Applications*, 54(1–3 SPEC. ISS.), pp. 245–260.

Sedov, L.I. (1965) *Two-dimensional problems of hydrodynamics and*

aerodynamics. New York: Interscience Publishers.

Shearer, C.M. and Cesnik, C.E.S. (2007) 'Nonlinear flight dynamics of very flexible aircraft', *Journal of Aircraft*, 44(5), pp. 1528–1545.

Shearer, C.M. and S. Cesnik, C.E. (2008) 'Trajectory control for very flexible aircraft', *Journal of Guidance, Control, and Dynamics*, 31(2), pp. 340–357.

Shkarayev, S., Null, W. and Wagner, M. (2004) *Development of micro air vehicle technology with in-flight adaptive-wing structure*. Tuscon, Arizona: Department of Aerospace and Mechanical Engineering, University of Arizona.

Shoele, K. and Zhu, Q. (2013) 'Performance of a wing with nonuniform flexibility in hovering flight', *Physics of Fluids*, 25(4)

Shyy, W., Berg, M. and Ljungqvist, D. (1999) 'Flapping and flexible wings for biological and micro air vehicles', *Progress in Aerospace Sciences*, 35(5), pp. 455–505.

Shyy, W., Ifju, P. and Viieru, D. (2005) 'Membrane wing-based micro air vehicles', *Applied Mechanics Reviews*, 58(4), p. 283.

Shyy, W., Jenkins, D. a. and Smith, R.W. (1997) 'Study of adaptive shape airfoils at low Reynolds number in oscillatory flows', *AIAA Journal*, 35(9), pp. 1545–1548.

Sitti, M. (2003) 'Piezoelectrically actuated four-bar mechanism with two flexible links for micromechanical flying insect thorax', *IEEE/ASME Transactions on Mechatronics*, 8(1) IEEE, pp. 26–36.

Spedding, G.R. and Maxworthy, T. (1986) 'The generation of circulation and lift in a rigid two-dimensional fling', *Journal of Fluid Mechanics*, 165, pp. 247–272.

Srygley, R.B. and Thomas, A.L.R. (2002) 'Unconventional lift-generating mechanisms in free-flying butterflies', *Nature*, 420(6916), pp. 660–664.

Stanford, B., Abdulrahim, M., Lind, R. and Ifju, P. (2007) 'Investigation of membrane actuation for roll control of a micro air vehicle', *Journal of Aircraft*, 44(3), pp. 741–749.

Su, W. and S. Cesnik, C.E. (2011) 'Dynamic response of highly flexible flying wings', *AIAA Journal*, 49(2), pp. 324–339.

Sun, M. (2005) 'High-lift generation and power requirements of insect flight', *Fluid Dynamics Research*, 37(1–2 SPEC. ISS.), pp. 21–39.

Sun, M., Tang, J. and Tang, H. (2002) 'Unsteady aerodynamic force generation by a model fruit fly wing in flapping motion', *Journal of Experimental Biology*, 205(1), pp. 55–70.

Tanaka, H., Whitney, J.P. and Wood, R.J. (2011) 'Effect of flexural and torsional wing flexibility on lift generation in hoverfly flight', *Integrative and Comparative Biology*, 51(1), pp. 142–150.

Tatineni, M. and Zhong, X. (2000) 'Numerical simulation of unsteady low-Reynolds-number separated flows over airfoils', *AIAA Journal*, 38(7), pp. 1295–1298.

Taylor, G.K., Nudds, R.L. and Thomas, A.L.R. (2003) 'Flying and swimming animals cruise at a Strouhal number tuned for high power efficiency.', *Nature*, 425(6959), pp. 707–711.

Triantafyllou, G.S., Triantafyllou, M.S. and Grosenbaugh, M.A. (1993) 'Optimal thrust development in oscillating foils with application to fish propulsion', *Journal of Fluids and Structures*, 7(2), pp. 205–224.

Triantafyllou, M.S., Triantafyllou, G.S. and Gopalkrishnan, R. (1991) 'Wake mechanics for thrust generation in oscillating foils', *Physics of Fluids A: Fluid Dynamics*, 3(12), pp. 2835–2837.

Tuncer, I.H. and Kaya, M. (2005) 'Optimization of flapping airfoils for maximum thrust and propulsive efficiency', *AIAA Journal*, 43(11), pp. 2329–2336.

Usherwood, J.R. and Ellington, C.P. (2002) 'The aerodynamics of revolving wings - I. Model hawkmoth wings', *Journal of Experimental Biology*, 205(11), pp. 1547–1564.

Vandenberghe, N., Zhang, J. and Childress, S. (2004) 'Symmetry breaking

leads to forward flapping flight', *Journal of Fluid Mechanics*, 506, pp. 147–155.

Vogel, S. (1967) 'Flight in Drosophila: III. aerodynamic characteristics of fly wing sand wing models', *Journal of Experimental Biology*, 46(3), pp. 431–443.

Vos, R., Geuskens, F.J.J.M.M. and Hoogreef, M.F.M. (2012) 'A new structural design concept for blended wing body cabins', *53rd AIAA/ASME/ASCE/AHS/ASC Structures, Structural Dynamics and Materials Conference*. American Institute of Aeronautics and Astronautics.

Wakeling, J.M. and Ellington, C.P. (1997) 'Dragonfly flight I. Gliding flight and steady-state aerodynamic forces', *The Journal of experimental biology*, 600, pp. 583–600.

Walker, J.A. (2002) 'Functional morphology and virtual models: Physical constraints on the design of oscillating wings, fins, legs, and feet at intermediate Reynolds numbers', *Integrative and Comparative Biology*, 42(2), pp. 232–242.

Wang, D., Wu, J. and Zhang, Y. (2013) 'Aerodynamics on flapping rotary wing in low Reynolds number', *2013 International Powered Lift Conference*. Los Angeles, CA: American Institute of Aeronautics and Astronautics, pp. 1–14.

Wang, Z., Chen, P.C., Liu, D.D., Mook, D.T. and Patil, M.J. (2006) 'Time domain nonlinear aeroelastic analysis for HALE wings', *47th AIAA/ASME/ASCE/AHS/ASC Structures, Structural Dynamics, and Materials Conference*. American Institute of Aeronautics and Astronautics, Vol.1, pp. 488–506.

Wang, Z.J. (2004) 'The role of drag in insect hovering', *Journal of Experimental Biology*, 207(23), pp. 4147–4155.

Wang, Z.J. (2008) 'Aerodynamic efficiency of flapping flight: analysis of a two-stroke model', *Journal of Experimental Biology*, 211(2), pp. 234–238.

Wang, Z.J. (2000) 'Vortex shedding and frequency selection in flapping flight', *Journal of Fluid Mechanics*, 410, pp. 323–341.

Ward, T.A., Fearday, C.J., Salami, E. and Binti Soin, N. (2017) 'A bibliometric

review of progress in micro air vehicle research', *International Journal of Micro Air Vehicles*, 9(2), pp. 146–165.

Weis-Fogh, T. (1973) 'Quick estimates of flight fitness in hovering animals including novel mechanisms for lift production', *Journal of Experimental Biology*, 59(1), pp. 169–230.

Williams, T. a (1994) 'A model of rowing propulsion and the ontogeny of locomotion in Artemia Larvae', *Biological Bulletin*, 187(June 1993), pp. 164–173.

Wilson, E.L. (2002) 'Static and dynamic aeroelasticity', *Elements*, 90(January), pp. 1689–703.

Wood, R.J. (2008) 'The first takeoff of a biologically inspired at-scale robotic insect', *IEEE Transactions on Robotics*, 24(2), pp. 341–347.

Wood, R.J., Avadhanula, S., Steltz, E., Seeman, M., Entwistle, J., Bachrach, A., Barrows, G., Sanders, S. and Fear, R.S. (2007) 'An autonomous palm-sized gliding micro air vehicle', *IEEE Robotics and Automation Magazine*, 14(2), pp. 82–91.

Wootton, R.J. (2010) 'Springy shells, pliant plates and minimal motors: Abstracting the insect thorax to drive a micro-air vehicle', in *Flying insects and robots*. Springer, pp. 207–217.

Wootton, R.J. (1981) 'Palaeozoic insects', *Annual Review of Entomology*, 26(1), pp. 319–344.

Wu, J., Wang, D. and Zhang, Y. (2015) 'Aerodynamic analysis of a flapping rotary wing at a low Reynolds number', *AIAA Journal*, 53(10), pp. 2951–2966.

Yingsong, G., Zhichun, Y. and Shun, H. (2015) 'Body freedom flutter of a blended wing body model coupled with flight control system', *Procedia Engineering*, 99, pp. 46–50.

Young, J., Walker, S.M., Bomphrey, R.J., Taylor, G.K. and Thomas, A.L.R. (2009) 'Details of insect wing design and deformation enhance aerodynamic

function and flight efficiency', *Science*, 325(5947), pp. 1549–1552.

Yu, W., Hodges, D.H., Volovoi, V. and Cesnik, C.E.S. (2002) 'On Timoshenko-like modeling of initially curved and twisted composite beams', *International Journal of Solids and Structures*, 39(19), pp. 5101–5121.

Zhao, L., Huang, Q., Deng, X. and Sane, S.P. (2010) 'Aerodynamic effects of flexibility in flapping wings', *Journal of The Royal Society Interface*, 7(44), pp. 485–497.

APPENDICES

Appendix A Baseline and optimized Composite Wing Laminate layups

The aeroelastic tailoring for maximum flutter speed results of laminate layups are provided in Table A-1 to Table A-7.

Table A-1 Baseline and optimized Laminate layups of wing skin part1 (degree)

Composite wing model	Baseline layups				Optimized layups			
Skin location	Upper Skin	Lower Skin	Front Spar	Rear Spar	Upper Skin	Lower Skin	Front Spar	Rear Spar
Laminate layup (symmetric half)	45	45	45	45	45	45	45	45
	45	45	0	45	-45	-45	-45	-45
	0	0	45	0	2	3	45	0
	45	-45	45	45	44	-44	45	45
	0	0	-45	0	2	3	-45	0
	-45	45	0	-45	-45	44	0	-45
	90	90	-45	90	62	62	-45	62
	-45	-45	90	90	-45	-44	62	62
	90	90	90	-45	62	62	62	-45
	90	90	-45	90	62	62	-45	62

Table A-2 Baseline and optimized Laminate layups of wing skin part2 (degree)

Composite wing model	Baseline layups				Optimized layups			
Skin location	Upper Skin	Lower Skin	Front Spar	Rear Spar	Upper Skin	Lower Skin	Front Spar	Rear Spar
Laminate layup (symmetric half)	45	45	45	45	45	45	45	45
	45	45	0	45	-45	-45	-45	-45
	0	0	45	0	17	7	45	1
	45	45	45	45	37	49	45	44
	0	-45	-45	0	17	-36	-44	1
	0	0	0	-45	17	7	-3	-45
	-45	45	0	0	-51	49	-3	1
	-45	0	-45	-45	-51	7	-44	-45
	90	90	90	90	43	63	61	47
	-45	45	90	90	-51	49	61	47
	90	90	-45	-45	43	63	-44	-45
	90	90	90	90	43	63	61	47

Table A-3 Baseline and optimized Laminate layups of wing skin part3 (degree)

Composite wing model	Baseline layups				Optimized layups			
Skin location	Upper Skin	Lower Skin	Front Spar	Rear Spar	Upper Skin	Lower Skin	Front Spar	Rear Spar
Laminate layup (symmetric half)	45	45	45	45	45	45	45	45
	45	45	0	45	-45	-45	-45	-45
	0	0	45	0	0	32	44	-45
	45	45	45	45	35	36	44	46
	45	-45	45	45	35	-39	44	46
	0	0	-45	0	0	32	-45	-45
	0	45	0	-45	0	36	0	-39
	-45	0	0	0	-30	32	0	-45
	-45	0	-45	-45	-30	32	-45	-39
	90	90	90	90	36	58	62	43
	0	-45	90	90	0	-39	62	43
	-45	-45	90	90	-30	-39	62	43
	90	90	-45	-45	36	58	-45	-39
	90	90	90	90	36	58	62	43

Table A-4 Baseline and optimized Laminate layups of wing skin part4 (degree)

Composite wing model	Baseline layups				Optimized layups			
Skin location	Upper Skin	Lower Skin	Front Spar	Rear Spar	Upper Skin	Lower Skin	Front Spar	Rear Spar
Laminate layup (symmetric half)	45	45	45	45	45	45	45	45
	45	45	0	45	-45	-45	-45	-45
	0	0	45	0	0	34	44	-7
	45	45	45	45	66	32	44	45
	45	45	45	45	66	32	44	45
	0	-45	-45	0	0	-65	-45	-7
	0	0	45	45	0	34	44	45
	-45	45	0	0	-18	32	-9	-7
	-45	0	0	-45	-18	34	-9	-41
	90	0	0	0	38	34	-9	-7
	0	90	-45	-45	0	67	-45	-41
	-45	-45	90	-45	-18	-65	62	-41
	90	-45	90	90	38	-65	62	44
	90	90	90	90	38	67	62	44
	90	90	-45	90	38	67	-45	44
	-45	90	90	-45	-18	67	62	-41
	90	-45		90	38	-65		44

Table A-5 Baseline and optimized Laminate layups of wing skin part5 (degree)

Composite wing model	Baseline layups				Optimized layups			
Skin location	Upper Skin	Lower Skin	Front Spar	Rear Spar	Upper Skin	Lower Skin	Front Spar	Rear Spar
Laminate layup (symmetric half)	45	45	45	45	45	45	45	45
	45	45	0	45	-45	-45	-45	-45
	45	45	45	45	64	34	44	44
	0	0	45	0	-49	30	44	1
	45	0	45	45	64	30	44	44
	45	45	-45	45	64	34	-43	44
	0	45	45	0	-49	34	44	1
	0	-45	0	45	-49	-64	0	44
	-45	0	0	0	-28	30	0	1
	-45	45	0	0	-28	34	0	1
	90	0	-45	-45	59	30	-43	-46
	0	0	90	0	-49	30	60	1
	-45	90	-45	-45	-28	60	-43	-46
	-45	-45	90	-45	-28	-64	60	-46
	90	45	-45	90	59	34	-43	47
	90	90	90	90	59	60	60	47
	90	90	90	90	59	60	60	47
	-45	90	-45	-45	-28	60	-43	-46
	90	-45	90	90	59	-64	60	47

Table A-6 Baseline and optimized Laminate layups of wing skin part6 (degree)

Composite wing model	Baseline layups							Optimized layups						
Skin location	Upper Skin	Lower Skin	Front Spar	Rear Spar	LGB* upper skin	LGB lower skin	LGB rear spar	Upper Skin	Lower Skin	Front Spar	Rear Spar	LGB upper skin	LGB lower skin	LGB rear spar
Laminate layup (symmetric half)	45	45	45	45	45	45	45	45	45	45	45	45	45	45
	45	45	0	45	45	45	45	-45	-45	-45	-45	-45	-45	-45
	45	45	45	45	45	45	45	72	5	44	44	45	42	45
	0	0	45	0	0	0	45	-1	5	44	2	-1	-6	45
	45	0	45	45	45	0	0	72	5	44	44	45	-6	0
	45	45	-45	45	45	45	0	72	5	-42	44	45	42	0
	0	45	45	0	0	45	45	-1	5	44	2	-1	42	45
	0	-45	45	45	0	-45	45	-1	-69	44	44	-1	-46	45
	-45	0	0	-45	-45	0	0	-24	5	-2	-45	-44	-6	0
	-45	-45	0	0	-45	-45	0	-24	-69	-2	2	-44	-46	0
	90	45	0	0	90	45	-45	48	5	-2	2	62	42	-44
	0	0	0	0	0	0	-45	-1	5	-2	2	-1	-6	-44
	-45	0	-45	-45	-45	0	0	-24	5	-42	-45	-44	-6	0
	0	90	90	0	0	90	-45	-1	57	47	2	-1	62	-44
	-45	-45	-45	-45	-45	-45	90	-24	-69	-42	-45	-44	-46	47
	-45	-45	90	-45	-45	-45	-45	-24	-69	47	-45	-44	-46	-44
	90	90	-45	90	90	90	90	48	57	-42	62	62	62	47
	90	90	90	90	90	90	90	48	57	47	62	62	62	47
	90	90	90	90	90	90	90	48	57	47	62	62	62	47
	-45	90	-45	-45	-45	90	90	-24	57	-42	-45	-44	62	47
	90	-45	90	90	90	-45	-45	48	-69	47	62	62	-46	-44

*LGB-Landing gear box

Table A-7 Baseline and optimized Laminate layups of wing skin part7 (degree)

Composite wing model	Baseline layups						Optimized layups					
Skin location	Upper Skin	Lower Skin	Front Spar	Rear Spar	LGB* upper skin	LGB rear spar	Upper Skin	Lower Skin	Front Spar	Rear Spar	LGB* upper skin	LGB rear spar
Laminate layup (symmetric half)	45	45	45	45	45	45	45	45	45	45	45	45
	45	45	0	45	45	45	-45	-45	-45	-45	-45	-45
	45	45	45	45	45	45	77	11	45	46	43	46
	45	0	45	0	45	45	77	0	45	0	43	46
	0	0	45	45	0	0	-10	0	45	46	0	0
	45	45	-45	45	45	0	77	11	-44	46	43	0
	45	45	45	0	45	45	77	11	45	0	43	46
	0	-45	45	45	0	45	-10	-67	45	46	0	46
	0	0	0	-45	0	0	-10	0	-2	-45	0	0
	0	-45	45	0	0	0	-10	-67	45	0	0	0
	-45	45	0	0	-45	-45	-36	11	-2	0	-44	-45
	-45	0	0	0	-45	-45	-36	0	-2	0	-44	-45
	90	0	0	-45	90	0	50	0	-2	-45	62	0
	0	90	0	0	0	-45	-10	56	-2	0	0	-45
	-45	0	-45	-45	-45	-45	-36	0	-44	-45	-44	-45
	0	-45	90	-45	0	90	-10	-67	47	-45	0	47
	-45	-45	-45	90	-45	-45	-36	-67	-44	48	-44	-45
	-45	90	90	90	-45	0	-36	56	47	48	-44	0
	90	90	-45	-45	90	90	50	56	-44	-45	62	47
	90	90	90	90	90	90	50	56	47	48	62	47
	90	90	90	-45	90	90	50	56	47	-45	62	47
	-45	-45	-45	90	-45	90	-36	-67	-44	48	-44	47
	90	-45	90	90	90	-45	50	-67	47	48	62	-45

*LGB-Landing gear box

Appendix B Image Processing Method for FWR Kinematics

B.1 Coordinate System Definition

If we assume that the observer is looking from the **z** direction, thus a vector r' on the wing is projected onto the x-y plane, and only the coordinate in this plane (r_1', r_2') will be visible to the observer, as shown in Figure B-1.
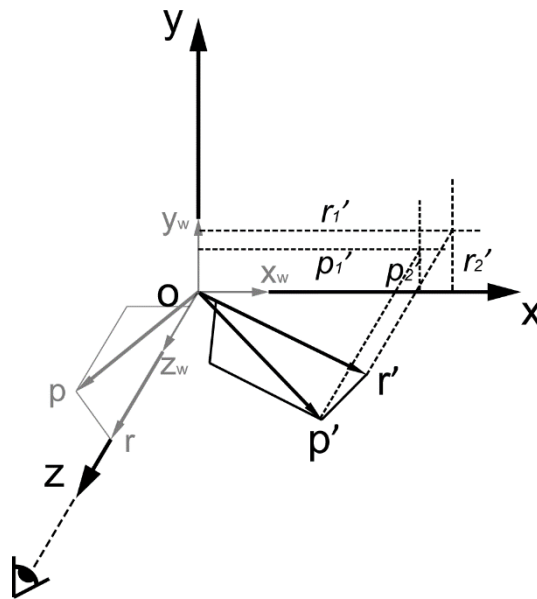

Figure B-1 The coordinate systems and the projection of the vectors on the wing.

Assumption:

a. The observer is strictly observing from the z direction, any deviation angle is neglected.

b. The wing is a rigid body, thus the geometric relation of the vector p on the wing with respect to the pitching axis r holds.

Apply Euler rotations ψ, ϕ and α to the coordinate system fixed on the wing successively with respect to y_w, x_w and $\mathbf{z_w}$ axes gives the vector r' as:

$$r' = R_{yw}R_{xw}R_{zw}r \qquad \textbf{(B-1)}$$

where the rotation matrix is written as:

$$R_{yw}R_{xw}R_{zw}$$

$$= \begin{bmatrix} \cos\psi\cos\alpha + \sin\psi\sin\phi\sin\alpha & -\cos\psi\sin\alpha + \sin\psi\sin\phi\cos\alpha & \sin\psi\cos\phi \\ \cos\phi\sin\alpha & \cos\phi\cos\alpha & -\sin\phi \\ -\sin\psi\cos\alpha + \cos\psi\sin\phi\sin\alpha & \sin\psi\sin\alpha + \cos\psi\sin\phi\cos\alpha & \cos\psi\cos\phi \end{bmatrix} \qquad \textbf{(B-2)}$$

Since the vectors $r(0,0,r_3)$ and $p(p_1,0,p_3)$ at reference position (shown in transparent in Figure B-1) can be obtained from the geometry of the wing, left multiply by the above rotation matrix gives the vectors' coordinates in the x-y plane as:

$$\begin{cases} r'_1 = \sin\psi\cos\phi \cdot r_3 \\ r'_2 = -\sin\phi \cdot r_3 \\ p'_1 = (\cos\psi\cos\alpha + \sin\psi\sin\phi\sin\alpha) \cdot p_1 + \sin\psi\cos\phi \cdot p_3 \\ p'_2 = \cos\phi\sin\alpha \cdot p_1 - \sin\phi \cdot p_3 \end{cases} \qquad \textbf{(B-3)}$$

B.2 Wing Geometry

For our wing model, the main beam serve as the pitching axis r, and the tip of the second bar is chosen as the mark vector p. Use PlotDigitizer to obtain the scaled geometry of the wing (as shown in Figure B-2), the vectors r and p are thus expressed as:

$$\begin{cases} r = k \cdot (0,0,1) = (0,0,k) \\ p = k \cdot (-0.315, 0, 0.895) = (-0.315k, 0, 0.895k)' \end{cases} \qquad \textbf{(B-4)}$$
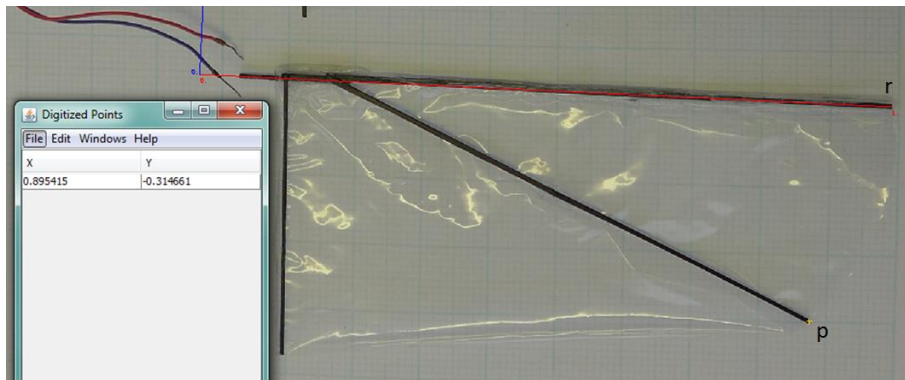
where k is the scale factor.

Figure B-2 The geometry of the wing used in PlotDigitizer.

B.3 Wing Kinematic Sequences

Use PlotDigitizer to obtain the kinematic sequences of the wing (as shown in Figure B-3). The processed frames are from frame No.300 to No.518, for each 2 frames, the first one is processed in order to reduce the workload. Since the high speed camera captures 1000 frames per second, we know that the time interval between each processed frame is $\Delta t = 0.002$ s.

In each frame, the coordinates of the vectors r' and p' (in the x-y plane) are obtained, thus the time histories of the vectors' motion are also obtained.

The wingspan as shown in the frame sequences corresponds to the scale factor k, which has the value of approximately 0.46. The obtained time history of the variation of the flapping angle ϕ and geometric AoA α are calculated and shown in Figure B-4 and Figure B-5.
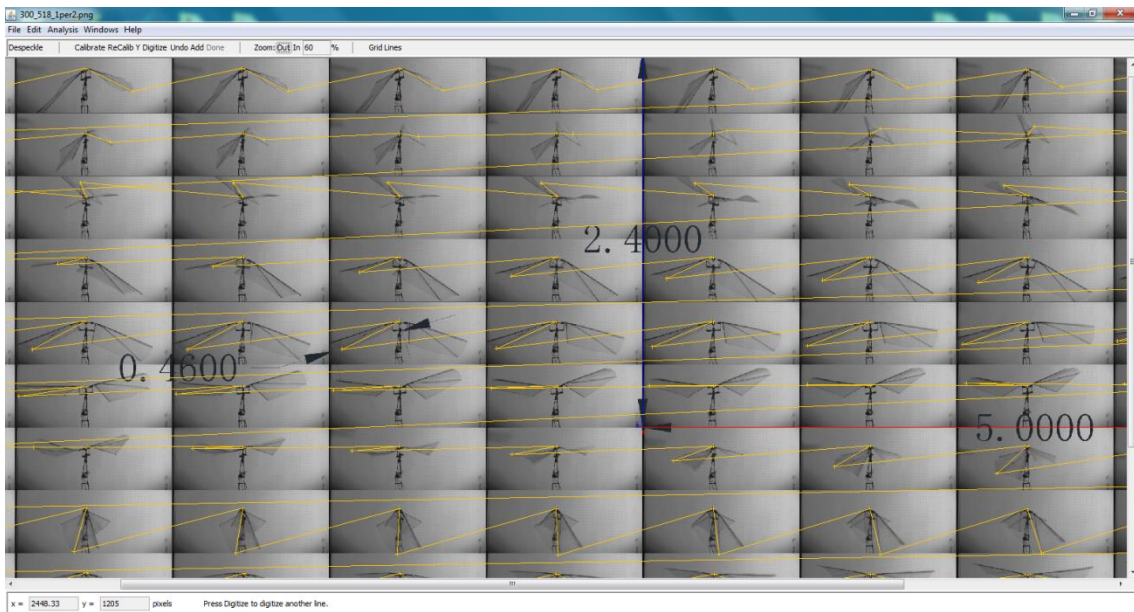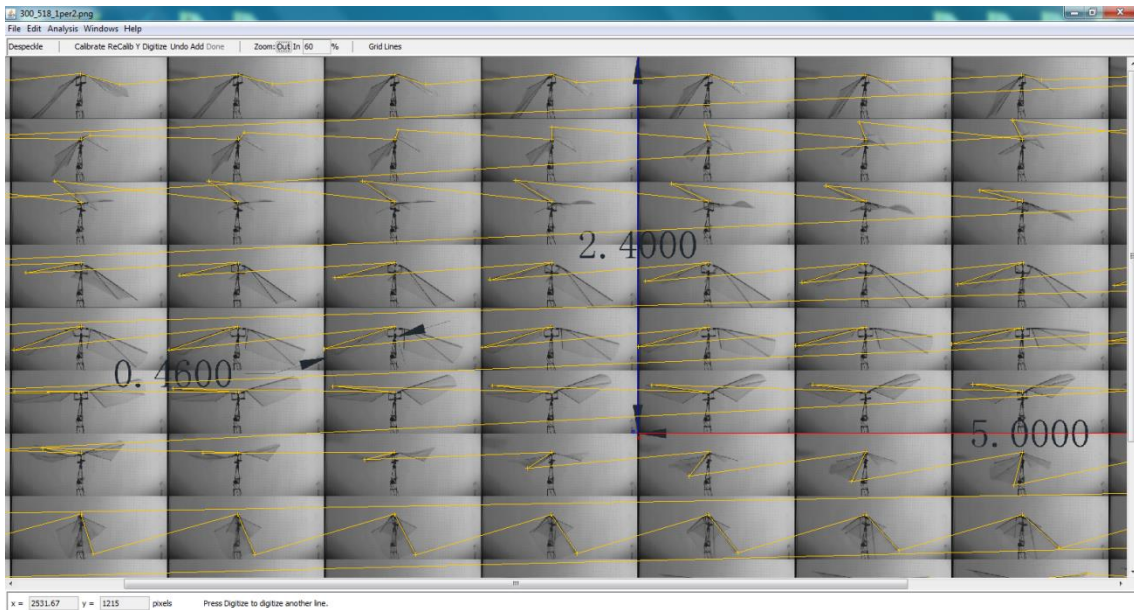
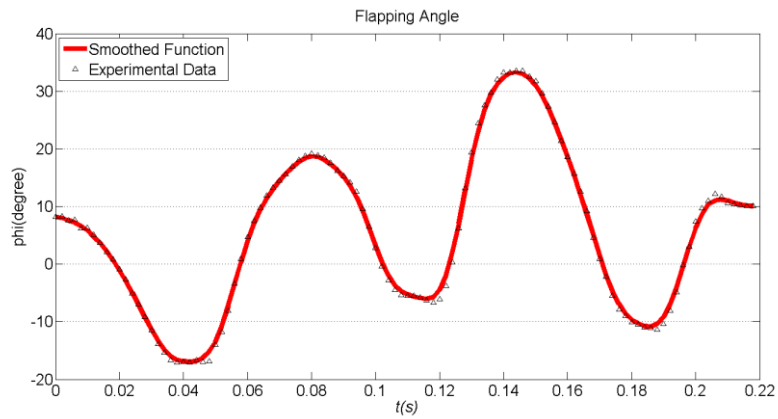Figure B-3 Figure processing for vectors (r' and p') on the wing in PlotDigitizer.

Figure B-4 Time history of the variation of the flapping angle ϕ. Angle units in degree (°) and time units in seconds (s).

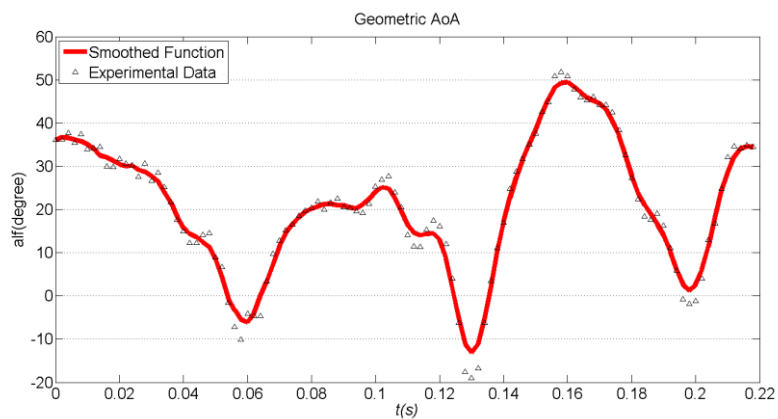Figure B-5 Time history of the variation of the geometric AoA α. Angle units in degree (°) and time units in seconds (s).

B.4 Correction for Camera Deviation Angle

As can be seen from equation (3), the flapping angle ϕ and pitching angle α can be sufficiently determined by r_2' and p_2', which means that we only need the y coordinates of the vectors (r' and p') to solve for the above two angles. This is because we assumed that the observer is strictly observing from the z direction. If we remove this assumption, and consider the deviation of the observer's view

166

from the z axis, for small deviation angles, the problem can still be resolved conveniently, as long as the deviation angles are known.

The deviation can be equivalently described by the rotation of the space containing the x-y-z frame, together with the wing by the angles δψ, δφ and δα with respect to y, x and z axes, respectively. For small rotations, the Euler angles δψ, δφ and δα are completely decoupled, the corresponding rotation matrix can be written as:

$$\delta R = I + \delta E \tag{B-5}$$

where I is identity matrix and δE is skew-symmetric matrix, which is expressed by the Euler angles as:

$$\delta E = \begin{bmatrix} 0 & -\delta\alpha & \delta\psi \\ \delta\alpha & 0 & -\delta\phi \\ -\delta\psi & \delta\phi & 0 \end{bmatrix} \tag{B-6}$$

Thus, the resultant vector after rotations is written as:

$$r'' = \delta R r' \tag{B-7}$$

it follows that:

$$r' = \delta R^{-1} r'' = r'' - \delta E r'' \tag{B-8}$$

Therefore, we can solve for the new coordinates:

$$\begin{cases} r_2' = -\sin\phi \cdot r_3 = r_2'' - \delta\alpha \cdot r_1'' + \delta\phi \cdot r_3'' \\ p_2' = \cos\phi\sin\alpha \cdot p_1 - \sin\phi \cdot p_3 = p_2'' - \delta\alpha \cdot p_1'' + \delta\phi \cdot p_3'' \end{cases}, \tag{B-9}$$

where the coordinates r_1'' and r_2'' are obtained from figure processing, and r_3'' can be calculated by the following relation:

$$\|r\|^2 = \|r''\|^2 = r_1''^2 + r_2''^2 + r_3''^2 = r_3^2 \tag{B-10}$$

it turns out that, the angle δψ, which corresponds to the deviation of the observer with respect to y axis, has no effect for the resultant φ and α.

It can be seen from equation (B-10) that the solution for r_3'' is not unique, since the square root corresponds to a positive and a negative value of r_3''. In order to solve the sign of r_3'', notice the continuity of the function r_3'': the sign of r_3'' flips over each time the vector passes through the x-y plane, where the norm $\|r_3''\|$ also becomes zero. Suppose the vector passes through x-y plane the Nth time, the sign of r_3'' is thus determined by the equation:

$$\text{sign}(r_3''|_n) = \text{sign}(r_3''|_1) \cdot (-1)^N \qquad \textbf{(B-11)}$$

therefore, for a given initial value of $\text{sign}(r_3''|_1)$, we can solve for the sign of the whole series $\text{sign}(r_3''|_n)$. Now, assume the data we obtained in section.3 are observed from a deviated angle given as $\delta\phi = 10°$ and $\delta\alpha = 5°$, which corresponds to a overlook and right-rolled view with 10° and 5°, respectively. The calculated time history of the variation of the flapping angle ϕ and geometric AoA α, in comparison with undeviated results are shown in Figure B-6 and Figure B-7.
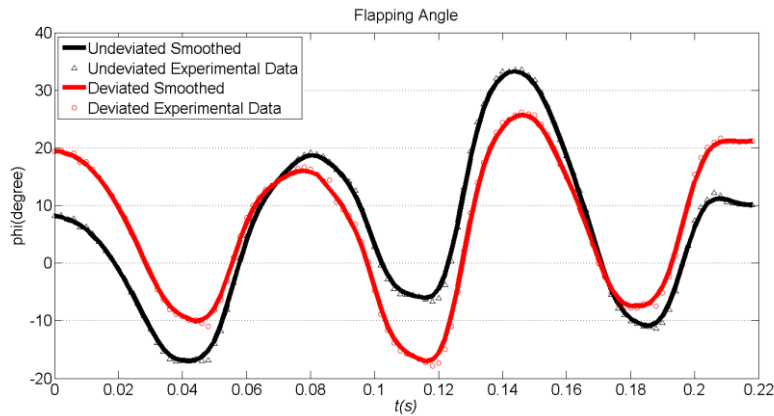

Figure B-6 Time history of the variation of the flapping angle ϕ. Results considering deviation of observer's view compare with undeviated view. Angle units in degree (°) and time units in seconds (s).
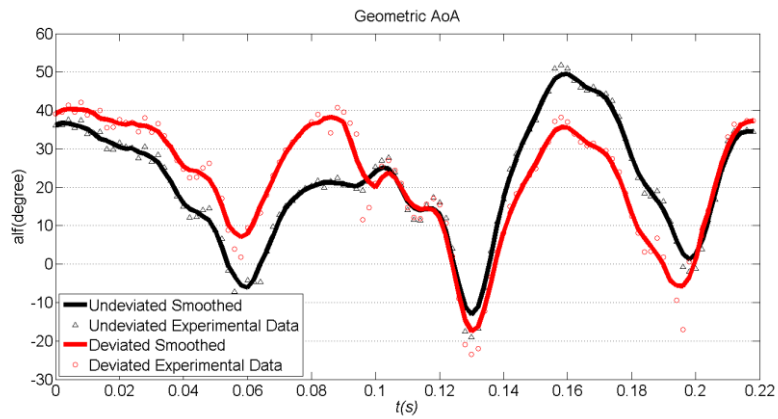
Figure B-7 Time history of the variation of the geometric AoA α. Results considering deviation of observer's view compare with undeviated view. Angle units in degree (°) and time units in seconds (s).

As can be seen from the above figures, small deviation angles of the observer's view (δϕ=10° and δα=5°) will affect the resultant flapping and pitching angles to a reasonable extent, especially for the time-history of the angles' variations.